

**On the Existence and Stability of Standing  
Solitary Waves in Faraday Resonance**

Thesis by  
Gary S. Guthart

In Partial Fulfillment of the Requirements  
for the Degree of  
Doctor of Philosophy

California Institute of Technology  
Pasadena, California  
June, 1992

(Submitted May 12, 1992)

## Acknowledgements

My sincere thanks go to Professor T. Yao-tsu Wu for his insight and guidance. His friendship and patience in matters scientific and otherwise are greatly appreciated. Deep thanks are also due to Dr. George Yates for his generous help and friendship. Thanks go to Professor Fred Raichlen for his help. Our discussions were both illuminating and enjoyable. I would also like to thank Ms. Helen Burrus, Mrs. Sharlene Cartier and Mrs. Susan Nakashima for all of their efforts on my behalf. The students in the Engineering Science group have made the day-to-day workings of graduate life interesting and fun. The men and women of The Chicken are a great group and their friendship is deeply valued. It is not possible to list the number of ways that my parents have supported my efforts. Their unwavering support is gratefully acknowledged. My deepest thanks go to my wife, Dawn, whose love and laughter have never diminished.

## Abstract

A rectangular tank of high-aspect ratio contains a liquid of moderate depth. The tank is subjected to vertical, sinusoidal oscillations. When the frequency of forcing is nearly twice the first natural frequency of the short side of the tank, waves are observed on the free surface of the liquid that slosh across the tank at a frequency equal to one half of the forcing frequency. These sloshing waves are modulated by a slowly varying envelope along the length of the tank. The envelope of the sloshing wave possesses two solitary-wave solutions, the standing soliton corresponding to a hyperbolic-secant solution and the standing kink wave corresponding to a hyperbolic-tangent solution. The depth and width of the tank determine which soliton is present. In the present work, we derive an analytical model for the envelope solitons by direct perturbation of the governing equations. This derivation is an extension of a previous perturbation approach to include forcing and dissipation. The envelope equation is the parametrically forced, damped, nonlinear Schrödinger equation. Solutions of the envelope equations are found that represent the solitary waves, and regions of formal existence are discussed. Next, we investigate the stability of these solitary-wave solutions. A linear-stability analysis is constructed for both the kink soliton and the standing soliton. In both cases, the linear-stability analysis leads to a fourth-order, nonself-adjoint, singular eigenvalue problem. For the hyperbolic-secant envelope, we find eigenvalues that correspond to the continuous and discrete spectrum of the linear operator. The dependence of the continuous-spectrum eigenvalues on the system parameters is found explicitly. By using local perturbations about known solutions and numerically continuing the branches, we find the bound-mode eigenvalues. For the kink soliton, continuous-spectrum branches are also found, and their dependence on the system parameters is determined. Bound-mode branches are found as well. In the case of the kink soliton, we extend the linear analysis by providing a nonlinear proof of stability when dissipation is neglected. We compute numerical solutions of the nonlinear Schrödinger equation directly and compare the results to the previous local analysis to verify the predicted behavior. Lastly, laboratory experiments were performed, examining the stability of the solitary waves, and comparisons are made with the foregoing work. In general, the agreement between the local analysis, the numerical simulations and the experiments is good. However, experiments and direct simulations show the existence of periodic solutions of the envelope equation when bound-mode instabilities are present.

# Contents

<b>Acknowledgements</b>	<b>ii</b>
<b>Abstract</b>	<b>iii</b>
<b>Table of Contents</b>	<b>iv</b>
<b>List of Figures</b>	<b>vi</b>
<b>List of Tables</b>	<b>viii</b>
<b>Nomenclature</b>	<b>ix</b>
<b>1 Introduction</b>	<b>1</b>
<b>2 Analytical Derivation</b>	<b>6</b>
2.1 Derivation of the Nonlinear Model . . . . .	6
2.2 Solitary-Wave Solutions . . . . .	11
2.3 Other Stationary Solutions . . . . .	15
<b>3 Standing-Soliton Stability</b>	<b>23</b>
3.1 Stability of $\xi$ -Independent Solutions . . . . .	24
3.1.1 Stability of the Flat Surface . . . . .	25
3.1.2 Stability of the Constant $r_0$ Solutions . . . . .	26
3.2 Stability of the Standing Solitary Wave . . . . .	28
3.2.1 Continuous Spectrum . . . . .	36
3.2.2 Discrete Spectrum . . . . .	38
3.2.3 The Complete Stability Picture . . . . .	42
3.2.4 Standing-Soliton Numerical Simulations . . . . .	43
3.2.5 Standing-Soliton Experiments . . . . .	47
<b>4 Kink-Wave Stability</b>	<b>79</b>
4.1 Kink-Wave Linear Stability . . . . .	80
4.1.1 Continuous Spectrum . . . . .	82
4.1.2 Discrete Spectrum . . . . .	84

4.1.3	The Linear-Stability Picture . . . . .	86
4.2	Kink-Wave Nonlinear-Stability Property . . . . .	87
4.2.1	Upper Bound for $\Delta M$ . . . . .	90
4.2.2	Lower Bound for $\Delta M$ . . . . .	92
4.2.3	Proof of Stability . . . . .	97
4.3	Kink-Wave Numerical Simulations . . . . .	98
4.4	Kink-Wave Experiments . . . . .	100
<b>5</b>	<b>Conclusions</b>	<b>110</b>
	<b>Appendices</b>	<b>113</b>
<b>A</b>	<b>Derivation of the Nonlinear Schrödinger Equation for a Stratified Fluid</b>	<b>113</b>
<b>B</b>	<b>Center Manifold for the Flat Surface</b>	<b>124</b>
<b>C</b>	<b>Eigenfunction-Construction Algorithm</b>	<b>126</b>
C.1	Matching Code for the Standing Soliton . . . . .	128
C.1.1	Discrete-Spectrum Eigenvalues . . . . .	130
C.1.2	Continuous-Spectrum Eigenvalues . . . . .	132
C.2	Matching Code for the Kink Wave . . . . .	134
<b>D</b>	<b>Perturbation Expansion for Bound-Mode Eigenvalues</b>	<b>137</b>
<b>E</b>	<b>Direct Simulation Algorithm</b>	<b>141</b>
	<b>References</b>	<b>143</b>

# List of Figures

2.1	19
2.2	19
2.3	20
2.4	20
2.5	21
2.6	21
2.7	22
3.1	55
3.2	56
3.3	57
3.4	57
3.5	58
3.6	58
3.7	59
3.8	60
3.9	60
3.10	61
3.11	61
3.12	62
3.13	62
3.14	63
3.15	64
3.16	65
3.17	65
3.18	66
3.19	67
3.20	68
3.21	69
3.22	69
3.23	70
3.24	71
3.25	71

3.26	72
3.27	73
3.28	73
3.29	74
3.30	75
3.31	75
3.32	76
3.33	76
3.34	77
3.35	77
3.36	78
4.1	103
4.2	104
4.3	104
4.4	105
4.5	105
4.6	106
4.7	106
4.8	107
4.9	107
4.10	108
4.11	108
4.12	109
4.13	109
A.1	122
A.2	122
A.3	123

## List of Tables

3.1	Continuous-spectrum stability results. . . . .	38
3.2	Discrete-spectrum stability results. . . . .	41
4.1	Continuous-spectrum stability results. . . . .	85
4.2	Discrete-spectrum stability results. . . . .	86

## Nomenclature

$b$  is the width of the tank.

$\ell$  is the length of the tank.

$h$  is the depth of the undisturbed fluid.

$g$  is the constant acceleration that is due to gravity.

$a_0$  is the amplitude of the vertical, sinusoidal forcing.

$\omega$  is one half of the frequency of the vertical, sinusoidal forcing.

$k = \pi/b$ , and is the wave number of the first, sloshing mode.

$\omega_0 = \sqrt{gk \tanh(kh)}$ , and is the natural frequency of the first, sloshing mode.

$\alpha$  is a nondimensional measure of dissipation.

$\beta = (\omega^2 - \omega_0^2)/(2\omega_0^2)$ , and is a nondimensional measure of the difference between the first, sloshing frequency and one half of the forcing frequency.

$\gamma = (a_0\omega^2)/g$ , and is a nondimensional measure of the forcing amplitude.

$\tilde{\gamma} = \pm\sqrt{\gamma^2 - \alpha^2}$ , and appears as a parameter in the soliton solutions and represents the forcing amplitude reduced by dissipation. The two signs of the square root indicate two different solution branches.

# Chapter 1

## Introduction

The phenomenon of forced-wave motion is of fundamental interest in many disciplines, from oceanography to optics. Within these fields, basic understanding of issues such as wave generation, wave stability and wave interactions is a continuing goal. Recently, attention has been given to parametrically forced, free-surface waves on a layer of liquid contained in a cylindrical tank as a result of the system's rich dynamical structure. Faraday (1831) first investigated parametrically forced water waves, observing subharmonic excitation of a liquid contained in a basin that was forced to oscillate vertically with frequency twice the natural frequency of the excited waves in the basin. Faraday waves have since been analyzed by Rayleigh (1883*ab*); Benjamin and Ursell (1954); Ockendon and Ockendon (1973); Miles (1984*a, b*); and others (for a review, see Miles and Henderson (1990)). By using small-motion approximations, Rayleigh explained why wave motions so excited are subharmonic. Benjamin and Ursell studied the stability of parametrically forced water waves, using linear theory and found that Mathieu's equation described the resulting waves. Ockendon and Ockendon extended this analysis to obtain some of the main features of nonlinear self-interaction. Miles applied the averaged Lagrangian method to calculate the nonlinear-interaction coefficients.

Agreement between theory and experiment has been examined by Henderson and Miles (1990), with the effects of viscous dissipation and surface tension taken into account for circular and rectangular cylinders, and discussed in the review of this general subject by Miles and Henderson.

One remarkable manifestation of the parametrically excited wave is the family called standing cross waves (or standing edge waves) generated on a layer of liquid contained in a rectangular basin of high-aspect ratio forced by a vertical, harmonic oscillation. Within this family, Wu et al. (1984) first showed experimentally the existence of a localized, standing solitary wave on a layer of modest depth contained in a high-aspect ratio, rectangular tank being subjected to vertical oscillation. At a forcing frequency slightly *below* twice the natural frequency  $\omega_0$  of the (0,1)-mode of the water waves within the tank, the forced oscillation generated standing cross waves sloshing to and fro across the width of the tank with their profile modulated by a hyperbolic-secant envelope along the tank's length. Subsequent theoretical work by Larraza and Putterman (1984) and Miles (1984*b*) showed that the standing soliton does not exist for values of  $kh \lesssim 1.022$ , where  $h$  is the uniform, quiescent water depth and  $k = \pi/b$ ,  $b$  being the width of the tank. However, we observed that for  $kh \gtrsim 1.022$  and for a forcing frequency slightly *above* twice the natural frequency  $\omega_0$  for the (0,1)-mode, a new family of surface waves exists that sloshes across the width of the tank and is modulated by a hyperbolic-tangent envelope. These waves are called kink waves and are stationary with respect to the long direction of the tank. Denardo et al. (1990) observed the kink wave independently, and we published our observations slightly after theirs without prior knowledge of their work.

In Chapter 2, we extend Larraza and Putterman's derivation of the envelope equation to include the effects of parametric forcing. Larraza and Putterman were motivated by Wu's observation of the parametrically forced soliton; however, their theoretical work examines the unforced, undamped wave only. By direct perturbation of the Euler equations, our analysis leads to the parametrically forced, nonlinear Schrödinger equation (NLS), giving the same governing equation that Miles finds using his Lagrangian formulation. Soliton solutions for both the standing soliton (Miles, Larraza and Putterman) and the standing kink wave (Guthart and Wu (1991); Denardo et al. (1990)) arise from this NLS equation.

As a preliminary objective, we seek to examine the stability of both the standing soliton and the standing kink wave analytically, numerically and experimentally. Faraday waves provide an excellent model system for comparison of analysis, computation and experimentation. The governing NLS envelope equation has applications in many different disciplines, making the stability results widely applicable to systems possessing nonlinearity, forcing and dissipation. Also, the experimental apparatus is relatively simple, allowing for clear comparison with analysis and computation. Recently, Laedke and Spatschek (1991) examined the linear stability of the standing-soliton solution of the NLS equation by using a Hamiltonian approach to establish bounds on the maximum growth rate of eigenfunctions. They identified some regions of linear instability, and they computed direct numerical simulations for some portions of the parameter space. We extend their work by determining the growth rates and eigenfunctions of their unstable modes and by confirming the existence of these instabilities in the laboratory. Furthermore, new regions of instability are identified within the parametric domain that were

omitted in their work. While writing our results, Barashenkov et al. (1991) independently published a theoretical investigation on the linear stability of solitons in condensed-matter physics. Their governing equation may be transformed into the NLS equation studied here for the hyperbolic-secant solution. The results of their study are eigenvalue branches in the parameter space. However, they did not carry out any direct numerical simulations or experiments. Their results agree with our numerically determined eigenvalues for the hyperbolic-secant solution. Our work complements theirs by independently identifying similar phenomena in the Faraday wave system, by examining all the parametric regions numerically and by verifying the analytic and numerical predictions experimentally.

In Chapter 3, we perform a linear-stability analysis for the standing soliton ( $kh > 1.022$ ). The operator for the linear system possesses a continuous spectrum of eigenvalues. We determine the dependence of these eigenvalues on the system parameters explicitly. Next, we numerically construct the bound-mode eigenvalues for the linear operator. By using direct numerical simulation of the forced NLS equation, we examine the stability properties of the standing soliton and compare the results with the theory. We find that the theory accurately predicts most of the behavior of the NLS equation. Near the bound-mode instabilities, unstable solitons do not break down completely, but instead, develop into periodic solutions. Finally, we experimentally determine the soliton's stability regions and we observe growth rates for continuous spectrum instabilities. Comparison between the theory and experiments shows good agreement for small-amplitude waves and small values of forcing and frequency detuning. The comparison weakens as the amplitude of the forcing or the detuning increases. The qualitative behavior of the soliton

instabilities predicted by the numerical simulations is in excellent agreement with our experimental observations.

In Chapter 4 we examine the stability of the standing kink wave. As with the standing soliton, we perform a linear-stability analysis. We identify the continuous spectrum of the linear operator and determine the eigenvalues. The bound-modes of the linear operator are difficult to identify in this case, since no local perturbations of exact solutions of the linear system could be found. However, we construct a more satisfactory stability proof by using time-invariant functionals of the NLS equation. Benjamin (1972) first used the idea of shape stability in his stability proof for soliton solutions of the Korteweg de-Vries equation. Bona (1975) made improvements to the method of the proof, and Zhidkov (1986) used similar ideas to show the stability of the hyperbolic-secant solution of the unforced NLS equation. We apply these ideas to kink solutions of the forced, undamped NLS equation, and obtain a proof of nonlinear stability. Again, direct numerical simulation of the NLS equation confirms the theoretical predictions. Comparison with experiment shows good agreement for regions of small-wave amplitude and small-forcing amplitude.

# Chapter 2

## Analytical Derivation

In this chapter, we derive the governing equation for sloshing waves on a liquid contained in a high-aspect ratio tank that is subject to vertical, sinusoidal oscillation. The derivation leads to a parametrically forced, damped, nonlinear Schrödinger (NLS) equation as a modulation of the first harmonic-sloshing mode. Analysis of the NLS equation shows that it possesses several stationary solutions, the standing soliton and the standing kink wave among them.

### 2.1 Derivation of the Nonlinear Model

We present here a theory for a dispersive, weakly nonlinear and weakly forced system, sustaining Faraday waves. The analysis is considerably simplified under the assumption that only one primary mode and its next higher harmonic are resonantly excited and that none of the natural frequencies of the secondary modes are close to the forcing frequency. We assume that no internal resonance occurs. A reference frame is taken, fixed to the rectangular tank with the  $x$ -axis directed along the long side of the tank of length  $\ell$ , the  $y$ -axis across the tank of width  $b$ ,  $b \ll \ell$ . The wave number  $k$  of the standing cross wave generated by the vertical oscillation is  $\pi/b$  and  $k\ell = O(1/\epsilon) \gg 1$  is a measure of the aspect ratio of the tank.

The  $z$ -axis points vertically upward so that  $z = 0$  at the quiescent water surface and  $z = -h$  at the tank bottom, which is flat and horizontal. Figure 2.1 shows a schematic of the tank and coordinate system. With the liquid assumed inviscid and incompressible and the motion assumed irrotational and free of capillary effects, the velocity potential  $\phi(x, y, z, t)$  and free-surface elevation  $\zeta(x, y, t)$  satisfy the field equation  $\nabla^2\phi = 0$  for  $-h \leq z \leq \zeta(x, y, t)$ , the wall condition for the normal velocity  $\mathbf{n} \cdot \nabla\phi = 0$  on the tank walls and bottom, and the free-surface conditions

$$w = \phi_z = \zeta_t + \phi_x \zeta_x + \phi_y \zeta_y, \quad (2.1)$$

$$\phi_t + \frac{1}{2}(\nabla\phi)^2 + \bar{g}(t)\zeta = 0, \quad (2.2)$$

on  $z = \zeta(x, y, t)$ , the subscripts denoting partial differentiation. Here, the forced acceleration of the tank is absorbed in the gravity term so that  $\bar{g}(t) = g(1 + 4\bar{\gamma} \cos(2\omega t))$ ,  $4\bar{\gamma}$  being the amplitude of the vertical, oscillatory acceleration imposed on the tank and scaled with respect to the constant gravitational acceleration  $g$ . The nondimensional forcing amplitude is then given by  $\bar{\gamma} = a_o\omega^2/g$ , where  $a_o$  is the amplitude of the vertical, sinusoidal forcing and  $2\omega$  is the frequency of the vertical forcing. We assume that  $\phi = O(\epsilon)$  and  $\zeta = O(\epsilon)$  in the motion weakly forced with  $\bar{\gamma} = \epsilon^2\gamma$ ,  $\gamma$  being of  $O(1)$ , where  $\epsilon = a/h$  is the nonlinearity parameter for a typical wave amplitude  $a$ , with  $\epsilon \ll 1$ . Expanding the conditions in (2.1) and (2.2) about  $z = 0$  in terms of  $\epsilon$  and eliminating  $\zeta$  in favor of  $\phi$ , we obtain (following Whitham (1976), now with additional  $t$ -dependence in  $\tilde{g}(t)$ )

$$\begin{aligned} & \phi_{tt} + g\phi_z - \frac{\phi_t}{g}(\phi_{tt} + g\phi_z)_z + [(\nabla\phi)^2]_t + \\ & + \nabla\phi \cdot \nabla \left[ \frac{1}{2}(\nabla\phi)^2 \right] + \frac{(\phi_{tt} + g\phi_z)_z}{2g} \left[ \frac{1}{g}(\phi_t^2)_z - (\nabla\phi)^2 \right] + \end{aligned}$$

$$\begin{aligned}
 & + \frac{(\phi_t)^2}{2g^2}(\phi_{tt} + g\phi_z)_{zz} - \frac{\phi_t}{g} [(\nabla\phi)^2]_{zt} + \\
 & + \epsilon^2\gamma g\phi_z \cos(2\omega t) + 2\omega\gamma\epsilon^2\phi_t \sin(2\omega t) = O(\epsilon^4), \tag{2.3}
 \end{aligned}$$

on  $z = 0$ . In this equation, use has been made of the expansion of  $\zeta$  up to  $O(\epsilon^2)$ ,

$$g\zeta = -(\phi_t - \frac{1}{g}\phi_t\phi_{zt} + \frac{1}{2}(\nabla\phi)^2) + O(\epsilon^3), \quad (z = 0). \tag{2.4}$$

The effects of the weak forcing excitation appear in the third-order terms of (2.3) and (2.4); however, they are needed only in (2.3).

For the phenomenon under investigation, we look for solutions of the above equation representing motions that slosh across the tank like  $\cos(ky)$ , with frequency  $\omega$  very nearly equal to the primary, natural frequency  $\omega_0$  and that are modulated along the  $x$ -direction by an envelope depending on a slow time,  $\tau$ , and a long space,  $\xi$ . The appropriate scales of these variables are  $\tilde{t} = \omega t$  for the fast time,  $\tau = \epsilon^2\omega t$  for the slow time, and  $\xi = \epsilon x$  for the long space. Thus, with the expansions

$$\phi = \sum_{n=1} \epsilon^n \phi_n(y, z, \tilde{t}; \xi, \tau), \tag{2.5}$$

$$\omega = \omega_0 + \epsilon\omega_1 + \epsilon^2\omega_2 + \dots, \tag{2.6}$$

the original field equation  $\nabla^2\phi = 0$  becomes

$$\nabla_2^2\phi_1 = 0, \quad \nabla_2^2\phi_2 = 0, \quad \nabla_2^2\phi_3 = -\phi_{1\xi\xi}, \tag{2.7}$$

where  $\nabla_2^2 = \partial_y^2 + \partial_z^2$  and  $\partial_y = \partial/\partial y$ ,  $\partial_z = \partial/\partial z$ . Proceeding to solve these equations with the wall conditions and the free-surface condition (2.3) taken by orders of  $\epsilon$ , we obtain for  $\phi_1$  the solution

$$\phi_1 = R_1(\tilde{t}; \xi, \tau) \cos(ky) \frac{\cosh(k(z+h))}{\cosh(kh)},$$

$$R_1(\tilde{t}; \xi, \tau) = \psi(\xi, \tau) \exp(-i\tilde{t}) + c.c.,$$

(c.c. denoting the complex conjugate of its preceding term), together with  $\omega_0^2 = gk \tanh(kh) \equiv gkT$  for the dispersion relationship. Suppression of the secular terms at the second-order analysis requires that  $\omega_1 = 0$  and gives for  $\phi_2$  the particular solution

$$\phi_2 = R_2(\tilde{t}; \xi, \tau) \left[ C_1 + C_2 \cos(2ky) \frac{\cosh(2k(z+h))}{\cosh(2kh)} \right],$$

with

$$\begin{aligned} R_2(\tilde{t}; \xi, \tau) &= i\psi^2(\xi, \tau) \exp(-2i\tilde{t}) + c.c., \\ C_1 &= \frac{-k^2}{8\omega_0} (1 + 3T^2), \quad (T \equiv \tanh(kh)) \\ C_2 &= \frac{3k^2}{8\omega_0 T^2} (1 - T^4). \end{aligned}$$

Note that the general solution to the second-order system includes a constant multiplying the solution to the homogeneous system,  $\phi_1$ . However, we may absorb this homogeneous solution into the first-order solution without loss of generality, so that the second-order solution appears as shown above. In the third-order analysis, suppression of the secular terms yields for  $\psi$  the equation

$$2i\omega_0^2 \psi_\tau + \bar{c}^2 \psi_{\xi\xi} + 2\omega_0 \omega_2 \psi + 2\gamma \omega_0^2 \psi^* + \bar{A} |\psi|^2 \psi = 0,$$

where

$$\begin{aligned} \bar{A} &= \frac{k^4}{8} (-9T^{-2} + 16 - 5T^2 + 6T^4), \\ \bar{c}^2 &= \frac{g}{2k} (T + kh(1 - T^2)), \end{aligned}$$

and \* denotes the complex conjugate. By dividing through by  $2\omega_0^2$  and defining  $\beta = \omega_2/\omega_0$ ,  $A = \frac{\bar{A}}{2\omega_0^2}$  and  $c^2 = \frac{\bar{c}^2}{2\omega_0^2}$ , we get

$$i\psi_\tau + c^2 \psi_{\xi\xi} + \beta \psi + \gamma \psi^* + A |\psi|^2 \psi = 0. \quad (2.8)$$

In terms of the real and imaginary components of  $\psi = p + iq$ , (2.8) gives

$$\begin{aligned} -q_\tau + c^2 p_{\xi\xi} + (\beta + \gamma)p + Ap(p^2 + q^2) &= 0, \\ p_\tau + c^2 q_{\xi\xi} + (\beta - \gamma)q + Aq(p^2 + q^2) &= 0. \end{aligned}$$

The above equation is the same as that found by Miles, using his Lagrangian approach. In the absence of forcing excitation, the reduced version of Equation 2.8 agrees with that given by Larraza and Putterman (1984). Furthermore, Equation 2.8 is consistent with a nonlinear Mathieu analysis when there is no  $\xi$  dependence. Notice that when the forcing is of order  $\epsilon$ , instead of the present order  $\epsilon^2$ , the foregoing analysis gives an equation similar to Equation 2.8 but without the cubic term and the  $\xi$  dependence and with the slow time given by  $\tau = \epsilon\omega t$ . Such an equation is consistent with the linear Mathieu analysis of Benjamin and Ursell (1954).

It is useful to add weak dissipation to the nonlinear Schrödinger equation. Several, previous approaches have been used to add dissipation to weakly nonlinear wave models. Theoretical estimates of the dissipation parameter, based on boundary layer losses alone, generally disagree with experiments because of the complex interactions occurring at the liquid, solid and air interface as well as the losses that are due to contaminants on the free surface (see Miles (1967)). We can motivate the form of the dissipative term in the nonlinear Schrödinger equation by considering boundary layers on the tank walls and the free surface and assuming the inner core of the flow to be irrotational. When this is done, a nondimensional parameter  $\alpha$  is introduced into the nonlinear Schrödinger equation as

$$i\psi_\tau + i\alpha\psi + c^2\psi_{\xi\xi} + \beta\psi + \gamma\psi^* + A|\psi|^2\psi = 0. \quad (2.9)$$

The parameter  $\alpha$  is easily seen to be dissipative (see, for example, Equation 2.10), and we leave  $\alpha$  to be determined experimentally. In order to ensure the loss of energy,  $\alpha$  is taken to be positive.

A few remarks about integrals of solutions to Equation 2.9 illustrate some of the basic properties of the equation. First, we note that

$$\frac{d}{d\tau} \int_{-\infty}^{+\infty} \psi(\xi, \tau) d\xi \neq 0,$$

so that the first moment is not conserved in time. Since the NLS equation governs the envelope of the first harmonic, sloshing mode, any  $\psi(\xi, \tau)$  conserves liquid mass. The energy integral is

$$\frac{d}{d\tau} \int_{-\infty}^{+\infty} |\psi(\xi, \tau)|^2 d\xi = -\alpha \int_{-\infty}^{+\infty} |\psi(\xi, \tau)|^2 d\xi + \gamma i \int_{-\infty}^{+\infty} \psi^{*2} - \psi^2 d\xi. \quad (2.10)$$

The above integral clearly shows the role of the parametric forcing,  $\gamma$ , and the dissipation,  $\alpha$ . When  $\alpha = 0$ , two time invariants of the motion given by Equation 2.9 may be identified; namely, with  $\psi = p + iq$ ,

$$\begin{aligned} H &= \int_{-\infty}^{\infty} \left( \frac{\beta}{2}(p^2 + q^2) + \frac{A}{4}(p^2 + q^2)^2 + \frac{\gamma}{2}(p^2 - q^2) - \frac{c^2}{2}((p_\xi)^2 + (q_\xi)^2) \right) d\xi, \\ L &= \int_{-\infty}^{\infty} (p_\xi q - q_\xi p) d\xi. \end{aligned} \quad (2.11)$$

$H$  is just the Hamiltonian identified by Miles (1984*b*). Both conserved quantities may be identified by analyzing the symmetries of the Lagrangian formulation of Equation 2.9 when  $\alpha = 0$ .

## 2.2 Solitary-Wave Solutions

We are interested in finding exact solutions to Equation 2.9 that are bounded as  $\xi$  goes to infinity. Without forcing excitation and without dissipation, (2.9) reduces

to a cubic Schrödinger equation that possesses solitary-wave solutions (Whitham (1974); Miles (1984*b*)). Taking  $\gamma = 0$ ,  $\alpha = 0$  and

$$\psi = \exp[i(r\xi - s\tau)]\Psi(X), \quad X = \xi - U\tau,$$

Equation 2.9 becomes

$$\frac{d^2\Psi}{dX^2} + \frac{\nu}{c^2}\Psi + \frac{A}{c^2}\Psi^3 = 0, \quad (2.12)$$

provided  $r = -\omega_0 U/c^2$  and  $\nu = 2\omega_0\omega_2 - c^2r^2 + s\omega_0^2$ , where  $\nu$  is introduced in place of  $s$  for algebraic convenience. Solutions of Equation 2.12 are noted to depend upon the signs of  $\nu$  and  $A$ . In the NLS equation,  $A$  plays a role similar to the coefficient of the nonlinear term in a cubic Duffing equation with the change in sign of  $A$  from negative to positive, corresponding to the change from hard-spring to soft-spring behavior, in the Duffing equation. With  $h = 1$  as the length scale,  $A$  is plotted versus  $k$  in Figure 2.2, which shows that  $A$  crosses zero from below at  $k \cong 1.022$ , with increasing  $k$ . For  $\nu < 0$  and  $k > 1.022$  ( $A > 0$ ), (2.12) has the solution

$$\Psi(X) = \left(\frac{-2\nu}{A}\right)^{\frac{1}{2}} \operatorname{sech}\left[\left(\frac{-\nu}{c^2}\right)^{\frac{1}{2}} X\right]. \quad (2.13)$$

If  $r = 0$  and  $s = 0$  ( $U = 0$  and  $\nu = 2\omega_0\omega_2$ ), this gives for  $\omega_2 < 0$  ( $\nu < 0$ ) the solution for the standing soliton that is stationary with respect to the slow time as reported by Larraza and Putterman (1984) and Miles (1984*b*). Since  $\omega_2 < 0$ , the wave frequency  $\omega$  is slightly lower than the primary-mode frequency,  $\omega_0$ .

In addition, however, we observe that for  $\nu > 0$  and  $A < 0$  ( $k < 1.022$ ), there is a new solution of (2.12) of the form

$$\Psi(X) = \left(\frac{\nu}{-A}\right)^{\frac{1}{2}} \tanh\left[\left(\frac{\nu}{2c^2}\right)^{\frac{1}{2}} X\right]. \quad (2.14)$$

For  $r = 0$  and  $s = 0$ , this solution exists for  $\nu > 0$  ( $\omega_2 > 0$  rendering the wave frequency  $\omega$  slightly greater than the primary-mode frequency,  $\omega_0$ , and is a wave envelope neither propagating nor varying with the slow time.

In the presence of forcing excitation and dissipation,  $\gamma \neq 0$  and  $\alpha \neq 0$ , we seek solutions of (2.9) that are similar in form to the  $\gamma = 0$ ,  $\alpha = 0$  solution (following Miles (1984b)). More precisely,

$$\psi = ae^{i\theta} f(\kappa\xi),$$

where  $\theta$  is a constant, phase angle,  $a$  is a real, positive constant and  $f$  is a real function of  $\kappa\xi$ . Substituting the above expression into (2.9) leads to two families of solitary-wave solutions. When  $A > 0$ , we have

$$\begin{aligned} f(\kappa\xi) &= \operatorname{sech}(\kappa\xi), \\ \sin(2\theta) &= \frac{\alpha}{\gamma}, \\ \cos(2\theta) &= \mp\sqrt{1 - \alpha^2/\gamma^2} \equiv -\frac{\tilde{\gamma}}{\gamma}, \\ \kappa^2 &= \frac{1}{c^2}(-\beta + \tilde{\gamma}) \text{ and} \\ a^2 &= \frac{2}{A}(-\beta + \tilde{\gamma}). \end{aligned} \tag{2.15}$$

The above solution of the parametrically forced, dissipative, nonlinear Schrödinger equation corresponds to the so-called standing soliton first observed by Wu, Keolian and Rudnick (1984). Miles was the first to identify the soliton analytically in the form shown above. Notice that the phase of the solution is independent of time and space, unlike the case of the free soliton. The phase locking of the soliton is due to the parametric forcing. There are at most two branches of stationary solutions whose relative phase is shifted by ninety degrees. These two solutions are differentiated by the sign of the parameter  $\tilde{\gamma} = \pm\sqrt{\gamma^2 - \alpha^2}$ . Furthermore, there are

no free parameters in the soliton solution. The amplitude, phase and characteristic length of the soliton are completely determined by the parameter space,  $(\alpha, \beta, \gamma)$ . The first-order approximation to the surface elevation corresponding to this soliton is given by

$$\zeta(x, y, t) = \frac{2\epsilon\omega}{g} a \operatorname{sech}(\kappa\epsilon x) \sin(\omega t) \cos(ky). \quad (2.16)$$

A computer-generated plot of the above solution for the surface of the liquid at a fixed time is shown in Figure 2.3. The dependence of the soliton on the system parameters is discussed further in Chapter 3.

When the depth of the water is less than the critical depth,  $kh < 1.022$ , the nonlinear, self-interaction coefficient changes sign ( $A < 0$ ), and we look for the kink solution of Equation 2.9. Now the solution is

$$\begin{aligned} f(\kappa\xi) &= \tanh(\kappa\xi), \\ \sin(2\theta) &= \frac{\alpha}{\gamma}, \\ \cos(2\theta) &= \pm\sqrt{1 - \alpha^2/\gamma^2} \equiv \frac{\tilde{\gamma}}{\gamma}, \\ \kappa^2 &= \frac{1}{2c^2}(\beta + \tilde{\gamma}) \text{ and} \\ a^2 &= \frac{1}{-A}(\beta + \tilde{\gamma}). \end{aligned} \quad (2.17)$$

The above solution corresponds to the standing kink wave observed by Guthart and Wu (1991) and Denardo, Wright, Larraza and Putterman (1990). Again, the solution is phase-locked with respect to the forcing. The phase, amplitude and characteristic length of the wave are completely determined by  $(\alpha, \beta, \gamma)$ . The two branches corresponding to the sign of  $\tilde{\gamma}$  are phase-shifted by ninety degrees. The first-order approximation to the surface elevation corresponding to this solution is

$$\zeta(x, y, t) = \frac{2\epsilon\omega}{g} a \tanh(\kappa\epsilon x) \sin(\omega t) \cos(ky). \quad (2.18)$$

A computer-generated plot of the above solution for the surface of the liquid at a fixed time is shown in Figure 2.4. The dependence of the kink wave on the system parameters is discussed more fully in Chapter 4.

## 2.3 Other Stationary Solutions

The parametrically forced, damped, nonlinear Schrödinger equation (2.9) possesses many stationary solutions. The above soliton solutions are limiting cases of more general solutions. The simplest solutions to Equation 2.9 are independent of  $\xi$ . They are worth mention because they set the stage for the more complex behavior found in the soliton solutions. The  $\xi$ -independent solutions are given by

$$\begin{aligned}\psi(\xi) &= r_0 e^{i\theta} \quad \text{where} \\ r_0^2 &= -\frac{\beta + \tilde{\gamma}}{A}, \\ \sin(2\theta) &= \frac{\alpha}{\gamma} \quad \text{and} \\ \cos(2\theta) &= \pm \sqrt{1 - \frac{\alpha^2}{\gamma^2}} = \frac{\tilde{\gamma}}{\gamma}.\end{aligned}\tag{2.19}$$

The trivial case,  $r_0 = 0$ , is always a solution. When  $\gamma > \alpha$ , there can be zero, one, or two solutions in the form shown above. A complete discussion of the  $\xi$ -independent solutions is given in the first section of Chapter 3.

When  $\xi$  dependence is included, solutions can be found by taking  $\psi(\xi)$  to be of the form

$$\psi(\xi) = e^{i\theta} f(\xi)$$

and substituting the above expression into Equation 2.9. Integrating the resulting equation once with respect to  $\xi$  leads to

$$\sin(2\theta) = \frac{\alpha}{\gamma},$$

$$\begin{aligned}\cos(2\theta) &= \pm\sqrt{\gamma^2 - \alpha^2} = \frac{\tilde{\gamma}}{\gamma}, \\ (f')^2 &= \frac{A}{2c^2}\left(\frac{-2(\beta + \tilde{\gamma})}{A}f^2 - f^4 + \frac{2C}{A}\right),\end{aligned}\tag{2.20}$$

where  $C$  is an undetermined constant of integration. Equation 2.20 possesses solutions that are elliptic functions. The following solutions may be identified. When  $kh > 1.022$ , implying that  $A > 0$ , there are two cases. Taking the integration constant  $C > 0$ , we have

$$\begin{aligned}f(\xi) &= a \operatorname{cn}\left(\sqrt{\frac{A}{c^2}}\left(\frac{\beta + \tilde{\gamma}}{A^2} + \frac{2C}{A}\right)^{\frac{1}{4}}\xi|m\right), \quad \text{where} \\ m &= \frac{1}{2} + \frac{-(\beta + \tilde{\gamma})}{2\sqrt{(\beta + \tilde{\gamma})^2 + \frac{2C}{A}}} \quad \text{and} \\ a^2 &= \frac{-(\beta + \tilde{\gamma})}{A} + \sqrt{\frac{(\beta + \tilde{\gamma})^2}{A^2} + \frac{2C}{A}}.\end{aligned}\tag{2.21}$$

The above solution is phase-locked, as expected. There exists one free parameter,  $C$ . Taking  $C = 0$  and requiring  $(\beta + \tilde{\gamma}) < 0$  implies that  $m = 1$ , and the hyperbolic-secant solution is recovered. A plot of the surface elevation corresponding to a cnoidal wave with  $m = 2/3$  is shown in Figure 2.5. Miles (1984*b*) first identified the cnoidal wave solution.

The second case for  $A > 0$  assumes that  $C < 0$ . An exact solution of Equation 2.20 can be found if the following conditions hold:

$$\begin{aligned}C &> -\frac{(\beta + \tilde{\gamma})^2}{2A} \quad \text{and} \\ 0 &> (\beta + \tilde{\gamma}).\end{aligned}$$

The solution is then a ‘‘dnoidal’’ wave given by

$$f(\xi) = a \operatorname{dn}\left(\sqrt{\frac{A}{2c^2}} a \xi|m\right),$$

$$\begin{aligned}
 a^2 &= -\frac{(\beta + \tilde{\gamma})}{A} + \sqrt{\frac{(\beta + \tilde{\gamma})^2}{A^2} + \frac{2C}{A}}, \text{ and} \\
 m &= \frac{2}{a^2} \sqrt{\frac{(\beta + \tilde{\gamma})^2}{A^2} + \frac{2C}{A}}.
 \end{aligned} \tag{2.22}$$

Here, taking  $C = 0$  implies that  $m = 1$ , and the solution corresponds to a spatially independent, nonzero solution. Figure 2.6 shows a plot of the free-surface elevation corresponding to a dnoidal wave with  $m = 2/3$ . In the literature on the standing-soliton problem, no mention of the dnoidal wave solution has been made.

Lastly, we can identify another solution when  $A < 0$ , ( $kh < 1.022$ ). This case requires

$$\begin{aligned}
 C &> 0 \quad \text{and} \\
 (\beta + \tilde{\gamma}) &> 0.
 \end{aligned}$$

Integration of Equation 2.20 then yields the following solution:

$$\begin{aligned}
 f(\xi) &= r \operatorname{sn} \left( \sqrt{\frac{-A}{2c^2}} s \xi |m \right), \\
 m &= \frac{r^2}{s^2}, \\
 r^2 &= \frac{(\beta + \tilde{\gamma})}{-A} - \sqrt{\frac{(\beta + \tilde{\gamma})^2}{A^2} + \frac{2C}{A}}, \quad \text{and} \\
 s^2 &= \frac{(\beta + \tilde{\gamma})}{-A} + \sqrt{\frac{(\beta + \tilde{\gamma})^2}{A^2} + \frac{2C}{A}}.
 \end{aligned} \tag{2.23}$$

If  $C = \frac{(\beta + \tilde{\gamma})^2}{-2A}$ , then  $m = 1$  and the kink-wave solution is recovered. The free-surface elevation corresponding to a snoidal solution with  $m = 2/3$  has been plotted and is shown in Figure 2.7. The snoidal wave solution has been identified by ourselves and by Denardo et al. (1990).

## **Figures for Chapter 2**

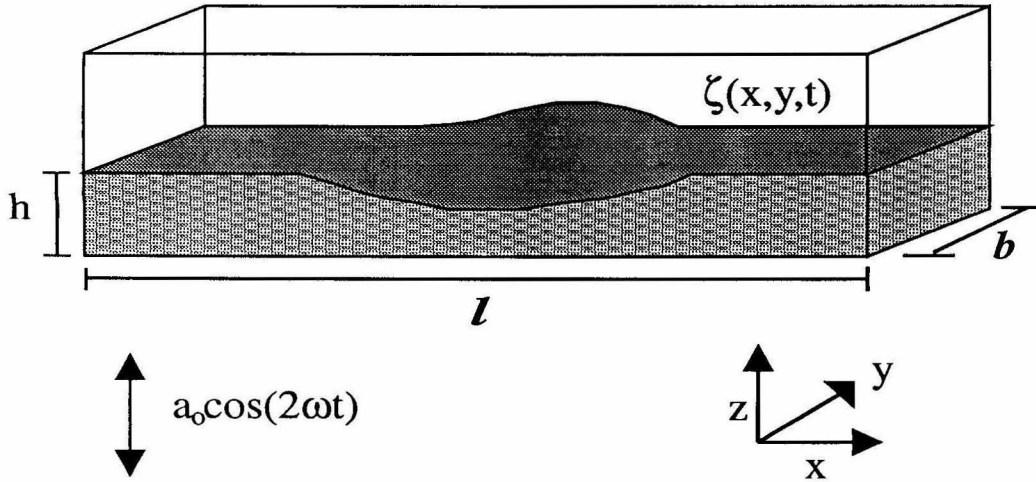


Figure 2.1: Schematic of experimental apparatus.

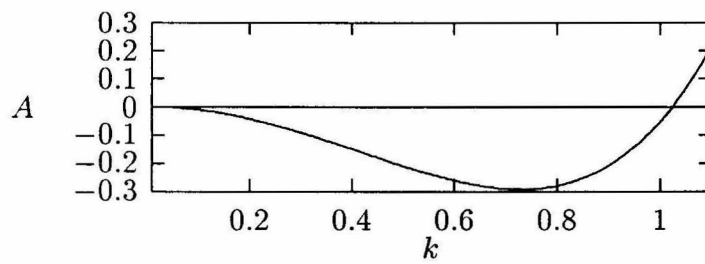


Figure 2.2: The nonlinear coupling coefficient,  $A$ , versus the wave number  $k$ , for cross waves in a rectangular tank with the water depth  $h = 1$ .

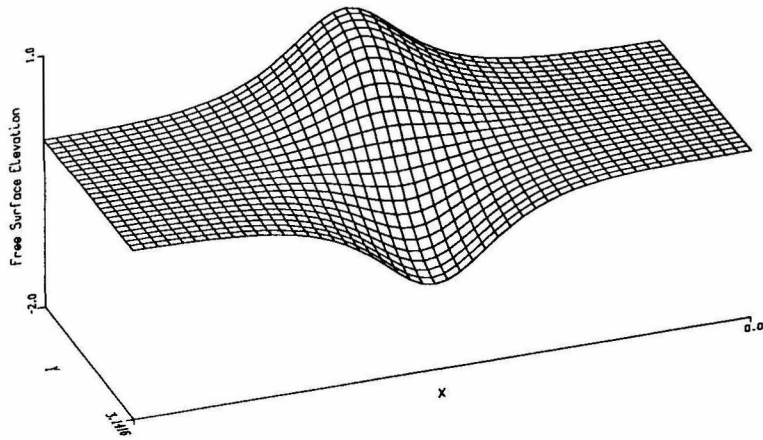


Figure 2.3: Computer-generated plot of the surface elevation for the sloshing soliton with  $a = 1$  and  $\kappa = 1$ .

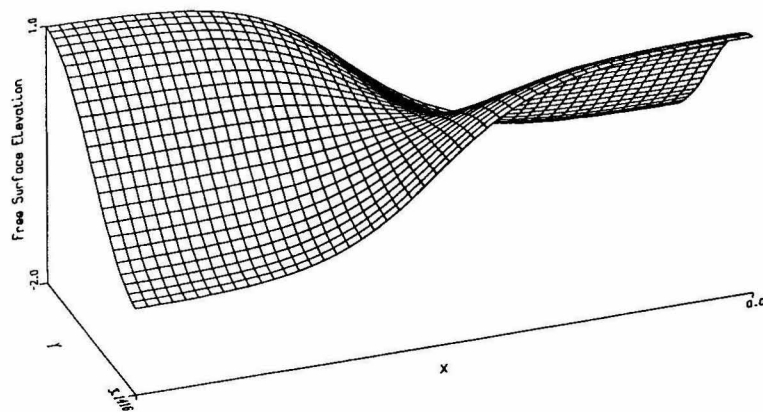


Figure 2.4: Computer-generated plot of the surface elevation for the sloshing kink wave with  $a = 1$  and  $\kappa = 1$ .

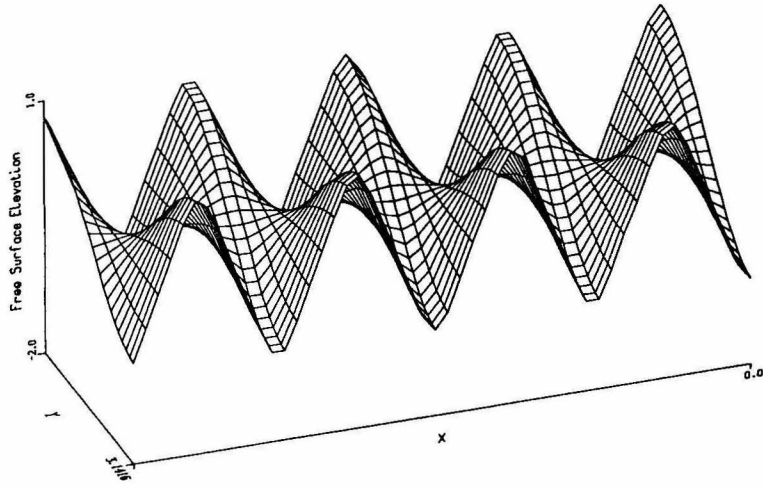


Figure 2.5: Computer-generated plot of the surface elevation for the cnoidal wave solution with  $a = 1$  and  $m = 2/3$ .

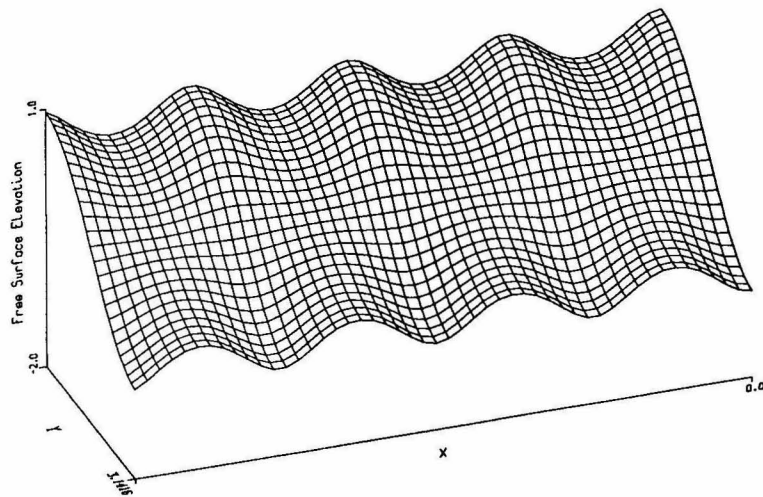


Figure 2.6: Computer-generated plot of the surface elevation for the dnoidal wave solution with  $a = 1$  and  $m = 2/3$ .

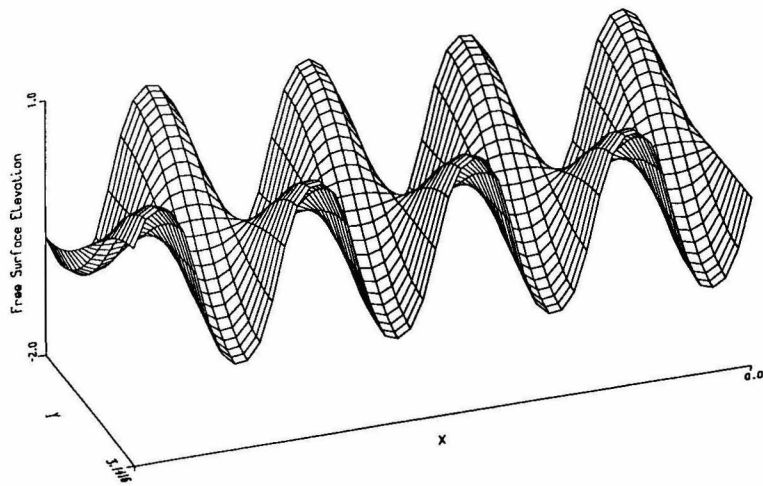


Figure 2.7: Computer-generated plot of the surface elevation for the snoidal wave solution with  $a = 1$  and  $m = 2/3$ .

## Chapter 3

# Standing-Soliton Stability

In the preceding chapter, we derived the governing NLS equation and provided several exact solutions, notably the standing solitary wave and standing kink wave. However, experimental investigations of the standing kink wave and standing solitary wave show that they cannot be observed in all regions of the  $(\alpha, \beta, \gamma)$  parameter space for which they formally exist. This leads to the question of stability of the various stationary solutions of the NLS equation. In this chapter, we start by analyzing the stability of the  $\xi$ -independent solutions. Miles (1984a) analyzed the stability of the  $\xi$ -independent solutions to  $\xi$ -independent perturbations, while Laedke and Spatschek (1991) consider  $\xi$  dependence in their perturbation, but only for  $A > 0$ . A brief review of the  $\xi$ -independent linear-stability analysis is convenient as a springboard into the soliton-stability question. Next, we investigate the linear stability of the standing-soliton (hyperbolic-secant) solution of the NLS equation. We find the continuous spectrum and discrete spectrum of the linear-stability operator. Numerical simulations of the NLS equation are performed and compared with the linear analysis. We conclude the chapter by comparing the stability analysis with our own experimental observations.

### 3.1 Stability of $\xi$ -Independent Solutions

The governing NLS equation and the  $\xi$ -independent solutions found in Chapter 2 are

$$\begin{aligned}
 i\psi_\tau + i\alpha\psi + c^2\psi_{\xi\xi} + \beta\psi + \gamma\psi^* + A|\psi|^2\psi &= 0, \\
 \psi(\xi) &= r_0 e^{i\theta}, \\
 r_0^2 &= -\frac{\beta + \tilde{\gamma}}{A}, \\
 \sin(2\theta) &= \frac{\alpha}{\gamma} \quad \text{and} \\
 \cos(2\theta) &= \pm\sqrt{1 - \frac{\alpha^2}{\gamma^2}} = \frac{\tilde{\gamma}}{\gamma},
 \end{aligned} \tag{3.1}$$

along with the solution  $r_0 \equiv 0$ , which exists for all values of  $(\alpha, \beta, \gamma)$ . The regions of existence for the above solutions are determined by the conditions  $\frac{\alpha}{\gamma} < 1$  and  $r_0^2 > 0$ . The regions of positive  $r_0^2$  depend upon the detuning,  $\beta$ , and the sign of the nonlinear, self-interaction coefficient,  $A$ . A plot of  $r_0^2$  versus  $\gamma$  for varying  $\beta$  conveniently illustrates the solution branches, as shown in Figure 3.1 for  $A > 0$  and in Figure 3.2 for  $A < 0$ . Where  $\gamma < \alpha$ , only the  $r_0 \equiv 0$  stationary solution exists. Physically, when the forcing is insufficient to overcome the dissipation, the only steady solution is a flat surface. When  $\gamma > \alpha$ , the number of steady solutions depends upon the sign of  $\beta$  and  $A$ .

For  $A > 0$ , there are three possible configurations for the nonzero-solution branches as determined by the  $r_0^2 > 0$  condition, as shown in Figure 3.1. When  $\beta > 0$ , only one nonzero branch exists for  $\gamma^2 > \alpha^2 + \beta^2$ . As  $\beta$  is reduced to zero, the inception point of the solution branch moves to  $\gamma = \alpha$ . Lastly, when  $\beta$  becomes negative, the solution develops two nonzero branches for the range  $\alpha < \gamma < \sqrt{\alpha^2 + \beta^2}$ . The two branches are distinguished by the sign of  $\tilde{\gamma} = \pm\sqrt{\gamma^2 - \alpha^2}$ .

As  $\gamma$  is increased past  $\sqrt{\alpha^2 + \beta^2}$ , only one branch keeps  $r_0^2 > 0$ .

For  $A < 0$ , the situation is reversed, as shown in Figure 3.2. When  $\beta < 0$ , only one nonzero branch gives rise to positive  $r_0^2$ . When  $\beta$  is increased to zero, the intersection of the branch with the axis moves to  $\gamma = \alpha$ . Lastly, when  $\beta$  becomes positive, two solution branches exist for  $\alpha < \gamma < \sqrt{\alpha^2 + \beta^2}$ , dropping to one branch when  $\gamma > \sqrt{\alpha^2 + \beta^2}$ .

### 3.1.1 Stability of the Flat Surface

Consider the linear stability of the flat-surface solution,  $r_0 = 0$ , subject to perturbations that depend on  $\xi$ . Letting  $\psi(\xi, \tau) = p + iq$ , and substituting into Equation 2.9 gives

$$\begin{aligned} -q_\tau - \alpha q + c^2 p_{\xi\xi} + (\beta + \gamma)p + Ap(p^2 + q^2) &= 0, \\ p_\tau + \alpha p + c^2 q_{\xi\xi} + (\beta - \gamma)q + Aq(p^2 + q^2) &= 0. \end{aligned} \quad (3.2)$$

Linearizing with respect to  $p$  and  $q$  and taking  $p = p_0 e^{\sigma\tau + i\kappa\xi}$  and  $q = q_0 e^{\sigma\tau + i\kappa\xi}$  leads to

$$\sigma = -\alpha \pm \sqrt{\gamma^2 - (\beta - \kappa^2 c^2)^2}.$$

When the real part of  $\sigma$  is positive, the flat surface is unstable. The condition for instability is then

$$\gamma^2 > \alpha^2 + (\beta - \kappa^2 c^2)^2. \quad (3.3)$$

Modes with  $\kappa = 0$  are independent of  $\xi$  and are unstable when  $\gamma > \sqrt{\alpha^2 + \beta^2}$ . If the value of  $\kappa$  is unrestricted and  $\beta \geq 0$ , there exist unstable modes whenever  $\gamma > \alpha$ . If  $\beta < 0$ , unstable modes exist when  $\gamma > \sqrt{\alpha^2 + \beta^2}$ .

Notice that when  $\gamma = \sqrt{\alpha^2 + (\beta - \kappa^2 c^2)^2} \equiv \gamma_c$ , the eigenvalues are given by  $\sigma_1 = 0$ ,  $\sigma_2 = -2\alpha$ , showing that a center manifold exists about the  $r_0 =$

0 fixed point. Using a result from dynamical systems theory, the stability of linearized system is insufficient to prove stability of the nonlinear system about the fixed point. When  $\xi$  dependence is included in the NLS system, the separation of variables used for the linear system fails when the nonlinear terms are included. However, if  $\xi$  dependence is neglected, we can find the stability property along the center manifold. The analysis is performed in Appendix B. The result is that the  $r_0 \equiv 0$  solution is *unstable* when  $\gamma = \gamma_c$ , and

$$A\beta > 0. \quad (3.4)$$

When  $A$  is positive and  $\beta$  is negative, the  $r_0 \equiv 0$  solution is stable along the critical surface. If  $A$  is negative, the  $\beta$  positive solution is also stable.

### 3.1.2 Stability of the Constant $r_0$ Solutions

Now consider the stability of the nonzero  $r_0$  solutions. Take  $\psi(\xi, \tau) = (r_0 + \eta(\xi, \tau))e^{i\theta}$ , where  $\eta$  is small. Substituting into Equation 2.9 gives

$$i\eta_\tau + i\alpha\eta + c^2\eta_{\xi\xi} + \beta\eta + \gamma\eta^*e^{-2i\theta} + 2r_0^2A\eta + r_0^2A\eta^* + Ar_0\eta^2 + 2Ar_0|\eta|^2 + A\eta|\eta|^2 = 0.$$

Linearize the above equation and make the substitution  $\eta(\xi, \tau) = p + iq$  to get the system

$$\begin{aligned} -q_\tau - 2\alpha q + c^2p_{\xi\xi} + (\beta + \tilde{\gamma})p + 3r_0^2Ap &= 0, \\ p_\tau + c^2q_{\xi\xi} + (\beta - \tilde{\gamma})q + r_0^2Aq &= 0. \end{aligned} \quad (3.5)$$

Taking  $p = p_0e^{\sigma\tau + i\kappa\xi}$  and  $q = q_0e^{\sigma\tau + i\kappa\xi}$  and solving for the eigenvalue  $\sigma$  leads to the following equation:

$$\begin{aligned} \sigma^2 + 2\alpha\sigma + f(\kappa) &= 0 \quad \text{where} \\ f(\kappa) &= \kappa^4c^4 + 2(\beta + 2\tilde{\gamma})\kappa^2c^2 - 4r_0^2A\tilde{\gamma}. \end{aligned} \quad (3.6)$$

Therefore, we have, for the eigenvalues  $\sigma_{1,2}$ ,

$$\sigma_{1,2} = -\alpha \pm \sqrt{\alpha^2 - f(\kappa)}.$$

Instability occurs when  $\sigma > 0$ , so that  $f(\kappa) < 0$  implies instability. There are four cases to consider,  $A > 0$  and  $A < 0$  with  $\tilde{\gamma} > 0$  and  $\tilde{\gamma} < 0$ .

Consider the case where  $A > 0$  and  $\tilde{\gamma} > 0$ . Figure 3.3 shows possible curves for  $f(\kappa)$  in this case. Everywhere  $f(\kappa) < 0$  implies modulational instability. There are always unstable modes in this case. If  $A > 0$  and  $\tilde{\gamma} < 0$ , possible curves for  $f(\kappa)$  are shown in Figure 3.4. This case also possesses unstable modes for all parameters for which the solution exists. When  $\kappa = 0$  so that the perturbations are spatially independent,  $f = -4r_0^2 A \tilde{\gamma}$ . Then for  $A > 0$ , the  $\tilde{\gamma} > 0$  solution is unstable, while the  $\tilde{\gamma} < 0$  solution is stable.

Now take the case  $A < 0$  and  $\tilde{\gamma} > 0$ . In this case, no value of  $\kappa$  makes  $f(\kappa)$  negative, so that the solution is *always* stable, as can be seen in the plot of  $f$  in Figure 3.5. For  $A < 0$  and  $\tilde{\gamma} < 0$ , possible  $f$ 's are shown in Figure 3.6. Here, there are always values of  $\kappa$  that are unstable. When  $\kappa = 0$ , the  $\tilde{\gamma} < 0$  solution is unstable and the  $\tilde{\gamma} > 0$  solution is stable.

Notice that when  $f(\kappa) = 0$ , the eigenvalues become 0 and  $-2\alpha$ , and a center manifold exists near the stationary solution. The linear-stability analysis is insufficient to predict the stability of the stationary solutions along the  $f(\kappa) = 0$  surface. However, the separation of variables of  $\xi$  and  $\tau$  fails when the nonlinear terms are included. No information about the  $f(\kappa) = 0$  surface is gained by neglecting the  $\xi$  dependence since,  $f(0) \neq 0$ , so that the question of stability along the  $f(\kappa) = 0$  surface remains open.

Now, we return to Figures 3.1 and 3.2 and display the stability information

about each branch. When  $A > 0$ , so that the water is above the critical depth, both nontrivial, constant amplitude solutions are unstable to modulations in  $\xi$ , when  $\kappa$  is allowed to take on any value. If  $A < 0$ , so that the water is relatively shallow, the upper branch of constant amplitude solutions is always *stable* while the lower branch is always unstable. Note, however, that a finite-length tank,  $\xi \in (-\ell/2, \ell/2)$ , implies that  $\kappa$  must be greater than  $\frac{\pi}{\ell}$  so that solutions may be stabilized since some values of  $\kappa$  cannot be obtained. Also, while large values of  $\kappa$  are not troublesome mathematically, they imply variations in the laboratory space that contradict our original assumption of slow variations along the length of the tank.

## 3.2 Stability of the Standing Solitary Wave

We now examine the linear stability of the standing solitary-wave solution. The approach is the same as that used for the  $\xi$ -independent solutions. Having identified all the parameter regions for which the solitary wave formally exists, we identify the stability properties of each branch. Although the analysis is linear, the problem is complicated by the addition of spatial variation in the coefficients of the linear operator. The addition of the  $\xi$  dependence in the solution results in a rich system, where variation of the parameters dramatically affects the response of the solitary wave.

The standing solitary wave is a solution of Equation 2.9 when  $A > 0$  ( $kh > 1.022$ ), and is given by Relations 2.15, which are repeated here:

$$\begin{aligned}\psi_0 &= ae^{i\theta} f(\kappa\xi), \\ f(\kappa\xi) &= \operatorname{sech}(\kappa\xi),\end{aligned}$$

$$\begin{aligned}
 \sin(2\theta) &= \frac{\alpha}{\gamma}, \\
 \cos(2\theta) &= \mp \sqrt{1 - \alpha^2/\gamma^2} \equiv -\frac{\tilde{\gamma}}{\gamma}, \\
 \kappa^2 &= \frac{1}{c^2}(-\beta + \tilde{\gamma}) \text{ and} \\
 a^2 &= \frac{2}{A}(-\beta + \tilde{\gamma}). \tag{3.7}
 \end{aligned}$$

Regions in the parametric domain for which the standing solitary wave exists can be determined by analyzing the above relations. Clearly,  $\gamma > \alpha$  is necessary. Further conditions can be visualized by plotting  $\kappa^2 c^2$  versus  $\gamma$ , as was done in the previous section, with  $r_0^2$  replaced by  $\kappa^2 c^2$ . The plot is shown in Figure 3.7. When  $\beta$  is negative, two solitary-wave solutions exist for  $\alpha < \gamma < \sqrt{\alpha^2 + \beta^2}$ , while one exists for  $\gamma > \sqrt{\alpha^2 + \beta^2}$ . For  $\beta = 0$ , only one solitary-wave solution exists for all  $\gamma > \alpha$ . Lastly, when  $\beta > 0$ , no solitary-wave solution exists for  $\alpha < \gamma < \sqrt{\alpha^2 + \beta^2}$ , and one exists for  $\gamma > \sqrt{\alpha^2 + \beta^2}$ .

Take  $\psi(\xi, \tau) = \psi_0(\xi) + e^{i\theta} \eta(\xi, \tau)$ , where  $\eta(\xi, \tau)$  is assumed to be small. Substituting into the nonlinear Schrödinger equation, Equation 2.9, and neglecting terms of  $O(\eta^2)$  gives the following equation:

$$i\eta_\tau + i\alpha\eta + c^2\eta_{\xi\xi} + \beta\eta + \gamma e^{-2i\theta}\eta^* + 2A|\psi_0(\xi)|^2\eta + A|\psi_0(\xi)|^2\eta^* = 0. \tag{3.8}$$

Let  $\eta(\xi, \tau) = \bar{p}(\xi, \tau) + i\bar{q}(\xi, \tau)$  and take  $\bar{\xi} = \kappa\xi$ . Substituting Equation 3.7 for  $\psi_0$  gives

$$\begin{aligned}
 -\bar{q}_\tau - 2\alpha\bar{q} + \kappa^2 c^2 \bar{p}_{\bar{\xi}\bar{\xi}} + (\beta - \tilde{\gamma})\bar{p} + 6\kappa^2 c^2 \text{sech}^2(\bar{\xi})\bar{p} &= 0, \\
 \bar{p}_\tau + \kappa^2 c^2 \bar{q}_{\bar{\xi}\bar{\xi}} + (\beta + \tilde{\gamma})\bar{q} + 2\kappa^2 c^2 \text{sech}^2(\bar{\xi})\bar{q} &= 0.
 \end{aligned}$$

Now take  $\bar{p}(\xi, \tau) = \text{Re}[p(\xi)e^{\sigma\tau}]$  and  $\bar{q}(\xi, \tau) = \text{Re}[q(\xi)e^{\sigma\tau}]$  and drop the bar on  $\bar{\xi}$  for

convenience to get the system

$$\begin{aligned} -\sigma q - 2\alpha q + \kappa^2 c^2 p_{\xi\xi} + (\beta - \tilde{\gamma})p + 6\kappa^2 c^2 \operatorname{sech}^2(\xi)p &= 0, \\ \sigma p + \kappa^2 c^2 q_{\xi\xi} + (\beta + \tilde{\gamma})q + 2\kappa^2 c^2 \operatorname{sech}^2(\xi)q &= 0. \end{aligned} \quad (3.9)$$

Now, since  $\kappa^2 c^2$  is known from Equation 3.7, substitution and rescaling gives the system

$$\begin{aligned} -\bar{\sigma}q - 2\bar{\alpha}q + p_{\xi\xi} - p + 6\operatorname{sech}^2(\xi)p &= 0, \\ \bar{\sigma}p + q_{\xi\xi} - mq + 2\operatorname{sech}^2(\xi)q &= 0, \end{aligned} \quad (3.10)$$

where

$$\begin{aligned} m &= \frac{\beta + \tilde{\gamma}}{\beta - \tilde{\gamma}}, \\ \bar{\sigma} &= \frac{\sigma}{-\beta + \tilde{\gamma}} \quad \text{and} \\ \bar{\alpha} &= \frac{\alpha}{-\beta + \tilde{\gamma}}, \end{aligned} \quad (3.11)$$

so that the coefficients take a simple form. The System 3.10 is nonself-adjoint with regular singular points at  $\xi = \pm\infty$ . We regard  $\bar{\sigma}$  as an eigenvalue and seek eigenfunctions  $(p(\xi), q(\xi))$  satisfying Equation 3.10 with  $(p(\xi), q(\xi)) \rightarrow (0, 0)$  as  $\xi \rightarrow \pm\infty$ . Examination of Equation 3.10 shows that if  $\bar{\sigma}$  is a eigenvalue with eigenfunction  $(p, q)$ , then  $\bar{\sigma}^*$  is an eigenvalue with eigenfunction  $(p^*, q^*)$ . Furthermore, when  $\alpha = 0$ , if  $\bar{\sigma}$  is an eigenvalue with eigenfunction  $(p, q)$ , then  $-\bar{\sigma}$  is an eigenvalue with eigenfunction  $(-p, q)$ .

In the search for eigenfunctions and eigenvalues for the linear system, System 3.10, we expect the singular points at infinity to lead to a continuous spectrum and possibly, a discrete spectrum of eigenvalues. In order to find the eigenvalues for the system, we examine the system by constructing the Frobenius series, about

the singular points, for a general solution of the linear system. By examining the series, we determine the values of  $\sigma$  that lead to solutions satisfying the boundary conditions on  $p$  and  $q$ , thereby finding the eigenvalues and eigenfunctions.

In order to examine the properties of the system, it is convenient to make the transformation  $z = \tanh(\xi)$  to bring the singular points at infinity to  $z = \pm 1$ . Series solutions are found at the singular point  $z = -1$  in the form

$$p(z) = (1+z)^r \sum_{n=0}^{\infty} a_n (1+z)^n \quad \text{and} \quad q(z) = (1+z)^r \sum_{n=0}^{\infty} b_n (1+z)^n.$$

Substitution of the expansions into the linear system determines the coefficients,  $a_n$  and  $b_n$ , and gives for the indices,  $r$ ,

$$r = \pm \frac{1}{2\kappa c} \sqrt{-\beta \pm \sqrt{\gamma^2 - (\alpha + \sigma)^2}}. \quad (3.12)$$

The indices at  $z = 1$  are given by the same expression, since the system is symmetric about  $z = 0$ . In general, the four indices,  $r$ , are complex. Two classes of eigenfunctions may be distinguished and constructed corresponding to continuous-spectrum eigenvalues and discrete-spectrum eigenvalues. The complete algorithm for constructing the eigenfunctions and eigenvalues is given in Appendix C, and a brief outline of the algorithm follows.

There are four independent series that may be constructed at the singular points corresponding to the four independent solutions of the linear system. Where the four values of the index,  $r$ , are distinct and not separated by integers, each index completely determines one series solution. Where there are repeated indices or indices separated by integers, the functional form of the series is different, but four independent series may still be constructed. From ordinary differential equation theory, each series is known to converge in the circle extending to the nearest

neighboring singular point. Therefore, the series solutions starting at  $z = -1$  converge for  $z \in [-1, +1)$ , while the series solutions starting at  $z = 1$  converge for  $z \in (-1, +1]$ . Every solution of the linear system must approach each singular point along a combination of the four series found near each singular point. To construct a complete solution across the entire interval  $[-1, +1]$ , we can match the four series starting at  $z = -1$  *smoothly* to those from  $z = +1$  at any intermediate point  $z_o \in (-1, +1)$ . Let an arbitrary solution be represented by a sum of the four series at  $z = -1$  so that

$$\begin{aligned} p_{-1}(z) &= C_1 p_1^-(z) + C_2 p_2^-(z) + C_3 p_3^-(z) + C_4 p_4^-(z) \\ q_{-1}(z) &= C_1 q_1^-(z) + C_2 q_2^-(z) + C_3 q_3^-(z) + C_4 q_4^-(z), \end{aligned}$$

where the  $C_i$  are arbitrary complex constants, and  $p_j^-$  is one of the four independent series originating at  $z = -1$ . The *same* solution may be represented by a sum of the four series at  $z = +1$  so that

$$\begin{aligned} p_{+1}(z) &= D_1 p_1^+(z) + D_2 p_2^+(z) + D_3 p_3^+(z) + D_4 p_4^+(z) \\ q_{+1}(z) &= D_1 q_1^+(z) + D_2 q_2^+(z) + D_3 q_3^+(z) + D_4 q_4^+(z), \end{aligned}$$

where the  $D_i$  are arbitrary complex constants, and  $p_j^+$  is one of the four independent series originating at  $z = +1$ . A representation of the solution convergent across the entire interval,  $[-1, +1]$  is obtained by matching the two series representations *smoothly* at a point  $z_o \in (-1, +1)$ . A smooth match requires that

$$\begin{aligned} p_{-1}(z_o) &= p_{+1}(z_o), \\ q_{-1}(z_o) &= q_{+1}(z_o), \\ p'_{-1}(z_o) &= p'_{+1}(z_o), \quad \text{and} \\ q'_{-1}(z_o) &= q'_{+1}(z_o). \end{aligned} \tag{3.13}$$

The first two conditions require continuity of the functions, and the second two conditions require continuity of the first derivatives. Application of the differential equations will ensure the continuity of all higher derivatives so that Conditions 3.13 ensure a completely smooth solution. However, not all of the solutions will satisfy the boundary conditions,  $p(\pm 1) = q(\pm 1) = 0$ . The equation for the indices, Equation 3.12, shows that the indices arise in two pairs,  $r = \pm r_i$ , where  $i = 1, 2$ . The form of the indices distinguishes two classes of eigenfunctions.

One class of eigenfunctions occurs when all four indices have a nonzero real part. When this is the case, inspection of Equation 3.12 shows that two indices will have positive real part, and two will have negative real part. In order to satisfy the boundary conditions at  $z = \pm 1$ , only the two indices having positive real part can be present. The two with  $r < 0$  are singular at  $z = \pm 1$  and fail to satisfy the boundary conditions. By including the series at  $z = \pm 1$  that possess indices with positive real part, we can look for eigenfunctions by finding the  $\sigma$ 's for which the series originating at  $z = -1$  can be joined smoothly to the series originating at  $z = +1$  by application of Conditions 3.13. The matching requirements impose four conditions on the four series coefficients,  $C_i, D_i$ ,  $i = 1, 2$ , giving a four-by-four matrix whose determinant must be zero in order for nontrivial solutions to exist. Values of  $\sigma$  that allow the matching conditions to be satisfied with nontrivial series coefficients are eigenvalues. These eigenvalues occur at discrete values of  $\sigma$  for fixed  $(\alpha, \beta, \gamma)$  and are similar to the bound modes of the linear Schrödinger equation,  $\Psi_{\xi\xi} + (E - V(\xi))\Psi = 0$ , when the energy,  $E$ , is less than the maximum potential. For the present system, the discrete-spectrum eigenvalue branches are found as functions of the parameters,  $(\alpha, \beta, \gamma)$ . Asymptotic approximations to

the bound-mode eigenvalues and eigenfunctions are found for small regions of the parameter space and the branches are continued numerically. We use a Newton-Raphson scheme to find the zeros of the determinant of the matrix given by the Conditions 3.13. The scheme is described in detail in Appendix C.

A second class of functions with indices given by Equation 3.12 occurs when pairs of the four indices are purely imaginary and opposite in sign. In this case, at least two of the four general solutions oscillate, without growth or decay, as  $z \rightarrow \pm 1$  ( $\xi \rightarrow \pm\infty$ ). To illustrate the construction of an eigenfunction, let one pair of indices be purely imaginary, while the second pair possesses nonzero real part. The series solutions with a purely imaginary index do not satisfy the boundary conditions, since they oscillate without growth or decay as the singular point is approached. However, in analogy with continuous-spectrum eigenfunctions of the linear Schrödinger equation, we relax the boundary condition at the singular points, looking for bounded solutions at  $z = \pm 1$ . We will show later that the original boundary conditions may be recovered. For the case of one pair of purely imaginary indices, three of the four series solutions are bounded at the singular points. Therefore, by retaining the three bounded series and discarding the singular series, application of the matching conditions, Conditions 3.13, leads to four conditions on the six coefficients,  $C_i, D_i, i = 1, 2, 3$ . The matching conditions can always be satisfied by suitable choices of the six coefficients. Therefore, solutions that are bounded at the singular points and span the interval can always be constructed where at least one pair of indices is purely imaginary.

The case of two imaginary pairs of indices has a similar property. In this case, all four series at the singular points lead to bounded solutions. Therefore,

the matching conditions, Conditions 3.13, impose four conditions on the eight coefficients,  $C_i, D_i, i = 1, \dots, 4$ . These matching conditions can always be satisfied by suitable choices of  $C_i$  and  $D_i$ , so that a bounded solution that spans the interval can always be constructed when both pairs of indices are purely imaginary.

The boundary conditions at  $z = \pm 1, p(\pm 1) = q(\pm 1) = 0$  are recovered for the solutions possessing a pair or pairs of purely imaginary indices by a synthesis of the eigenfunctions that are described above. We find that for fixed parameters,  $(\alpha, \beta, \gamma)$ , eigenvalues leading to purely imaginary indices occur in a continuous range,  $\sigma \in [\sigma_{min}, \sigma_{max}]$ . Therefore, a general solution of the linear system is a synthesis of all the possible eigenfunctions at the fixed values of the parameters,  $(\alpha, \beta, \gamma)$ . For example,

$$p(z) \sim \int_{\sigma_{min}}^{\sigma_{max}} F(\sigma)(1+z)^{i\rho(\sigma)} d\sigma \quad \text{as } z \rightarrow -1,$$

where  $\rho(\sigma)$  is known from Equation 3.12,  $r = i\rho$ , and  $F(\sigma)$  is a well-behaved weighting function determined by the initial conditions. This expression can be shown to go to zero by repeated application of integration by parts. Therefore, solutions satisfying the boundary conditions and the differential equation with a known distribution of eigenvalues may be constructed. This continuous range of eigenvalues is similar to the continuous spectrum of the linear Schrödinger equation and is called the continuous spectrum for the present linear system. Appendix C provides a complete description of the matching algorithm.

### 3.2.1 Continuous Spectrum

Solutions to Equation 3.9 possessing pairs of complex indices at the singular points constitute the continuous spectrum. Purely imaginary indices require that

$$-\beta \pm \sqrt{\gamma^2 - (\alpha + \sigma)^2} \tag{3.14}$$

is real and negative. There are four cases that satisfy this condition. The sign of the leading term,  $-\beta$ , is important, and two cases arise from each sign. Let  $\sigma = \sigma_r + i\sigma_i$  where  $\sigma_r$  and  $\sigma_i$  are real.

First, let  $\beta > 0$  so that only the  $\tilde{\gamma} > 0$  solution is present, and  $\gamma > \sqrt{\alpha^2 + \beta^2}$  is required for existence of the solution. Then Expression 3.14 is real and negative for at least one sign of the square root when

$$\begin{aligned} \sigma_i &= 0, \\ -\alpha - \gamma < \sigma_r < \gamma - \alpha, \end{aligned} \tag{3.15}$$

or when

$$\begin{aligned} \sigma_r &= -\alpha \quad \text{and} \\ \sigma_i &\quad \text{takes on any value.} \end{aligned}$$

Any  $\sigma$  in the regions above leads to an eigenfunction of the linear system. Therefore, since  $\gamma > \alpha$  for any soliton solution, Equation 3.15 shows that eigenfunctions exist with  $0 < \sigma_r < \gamma - \alpha$ , so that these solutions grow exponentially in the slow time and are unstable. Therefore, when  $\beta > 0$ , the lone soliton solution ( $\tilde{\gamma} > 0$ ) is always unstable to the continuous spectrum.

Now let  $\beta < 0$  so that both the  $\tilde{\gamma} > 0$  and  $\tilde{\gamma} < 0$  solutions exist. Expression 3.14 is real and negative, when the *negative* sign of the square root is taken,

for the following two cases:

$$\begin{aligned} \sigma_i &= 0, \quad \text{and} \\ -\alpha - \sqrt{\gamma^2 - \beta^2} &< \sigma_r < -\alpha + \sqrt{\gamma^2 - \beta^2}, \end{aligned} \quad (3.16)$$

when  $\gamma^2 > \beta^2$  and

$$\begin{aligned} \sigma_r &= -\alpha, \quad \text{with} \\ \sigma_i &> \sqrt{\beta^2 - \gamma^2}, \quad \text{or} \\ \sigma_i &< -\sqrt{\beta^2 - \gamma^2}, \end{aligned} \quad (3.17)$$

when  $\gamma^2 < \beta^2$ . In both cases, one pair of indices is purely imaginary and one pair is purely real. At least one pair of imaginary indices exists throughout the parameter space. The eigenvalues leading to these indices have negative real part and nonzero imaginary part when  $\gamma < |\beta|$ , and they have nonzero real part and zero imaginary part when  $\gamma > |\beta|$ . Figures 3.8 and 3.9 show the regions in the parameter space possessing these solutions.

The stability property of the continuous spectrum is described as follows. When  $\beta < 0$  and  $\gamma < |\beta|$ , the continuous spectrum always produces solutions to Equation 3.9 that are *stable*, having real part  $-\alpha$  and nonzero imaginary part as given by Equation 3.17. When  $\gamma$  increases past  $|\beta|$ , the continuous-spectrum solutions have eigenvalues that are purely real and lie within the range given by Equation 3.16. The purely real eigenvalues give rise to unstable solutions when  $\sigma_r = -\alpha + \sqrt{\gamma^2 - \beta^2} > 0$ , implying *instability* when

$$\gamma^2 > \alpha^2 + \beta^2.$$

The above stability result is the same as that found by Laedke and Spatschek (1991). However, we are able to give an analytic expression for the maximum

	$\tilde{\gamma} > 0$	$\tilde{\gamma} < 0$
$\beta > 0$	Always Unstable	Does not exist
$\beta < 0$	Stable for $\gamma < \sqrt{\alpha^2 + \beta^2}$	Always Stable

Table 3.1: Continuous-spectrum stability results.

growth rate of the unstable modes,

$$\sigma_{rmax} = -\alpha + \sqrt{\gamma^2 - \beta^2}, \quad \sigma_{imax} = 0. \quad (3.18)$$

Notice that the above results apply to both solitary-wave solutions, corresponding to  $\tilde{\gamma}$  positive and negative when  $\beta < 0$ . When  $\tilde{\gamma} > 0$ , the stationary solution exists for  $\beta > 0, \beta = 0$ , and  $\beta < 0$ . If  $\beta > 0$ , positive eigenvalues always exist and this solution is always unstable. When  $\beta = 0$ , unstable modes also exist. Lastly, for  $\beta < 0$ , the solution exists for all  $\gamma > \alpha$  and is stable for  $\alpha < \gamma < \sqrt{\alpha^2 + \beta^2}$ .

The second stationary solution,  $\tilde{\gamma} < 0$ , can exist only for  $\beta < 0$  and  $\gamma < \sqrt{\alpha^2 + \beta^2}$ . Hence, the maximum growth rate of the continuous modes is always negative, and this mode is always stable with respect to the continuous spectrum. The response of the two solutions to the continuous spectrum of the linear operator is summarized in Table 3.1.

### 3.2.2 Discrete Spectrum

When the four indices corresponding to Equation 3.9 all possess nonzero real part, eigenfunctions for the linear system occur only at discrete values of  $\sigma$ . The method for constructing eigenfunctions is a combined numerical and asymptotic approach. We can find asymptotic approximations to the bound-mode eigenvalue branches for small  $\alpha$  and  $\gamma$ . By starting a numerical scheme along these approximate branches, we can continue the branches out into the rest of the parametric space.

Originally our computations were performed for arbitrary  $\alpha$  and  $\gamma$ . However, following Barashenkov's work on a similar equation, it is possible to transform our linear system containing nonzero  $\alpha$  into one with  $\alpha = 0$  and thereby reduce the parameter space by one. This transformation is achieved by taking  $\eta(\xi, \tau)$  in Equation 3.8, to be

$$\eta(\xi, \tau) = e^{-\alpha\tau}(p(\xi, \tau) + iq(\xi, \tau)).$$

Taking  $\bar{\alpha} = \alpha/\kappa^2 c^2$  and scaling time as  $\tau = \kappa^2 c^2 \tau$  gives the linear system,

$$\begin{aligned} q_\tau + \bar{\alpha}q &= p_{\xi\xi} - p + 6\text{sech}^2(\xi)p = L_1[p], \\ -p_\tau + \bar{\alpha}p &= q_{\xi\xi} + \frac{\beta + \tilde{\gamma}}{\beta - \tilde{\gamma}}q + 2\text{sech}^2(\xi)q = L_2[q]. \end{aligned}$$

Now, taking  $p(\xi, \tau) = \text{Re}[e^{\sigma\tau}p(\xi)]$  and  $q(\xi, \tau) = \text{Re}[e^{\sigma\tau}q(\xi)]$  gives

$$\begin{aligned} (\sigma + \bar{\alpha})q &= L_1[p], \\ -(\sigma - \bar{\alpha})p &= L_2[q]. \end{aligned}$$

Defining  $\nu^2 = \sigma^2 - \bar{\alpha}^2$  and  $\bar{q}(\xi) = (\sigma + \bar{\alpha})q(\xi)/\nu$ , leads to

$$\begin{aligned} \nu\bar{q} &= L_1[p], \\ -\nu p &= L_2[\bar{q}], \end{aligned}$$

which is just the linear system with  $\bar{\alpha} = 0$ . Hence, only the eigenvalue branch occurring when  $\alpha = 0$  needs to be computed. The eigenvalues for  $\alpha \neq 0$  follow from the inversion of the above transformations. The transformation allows for the elimination of  $\alpha$  in the matching computation only. In order to reconstruct the general stability diagram with nonzero  $\alpha$ , it is necessary to feed the  $\alpha = 0$  branches into a second program to process the inversion. Therefore, while the transformation reduces the root-finding computations to one case, a second computation is needed

to reproduce the general case so that as a practical matter, computational work is only slightly reduced.

The dependence of the eigenvalue on the parameters is shown in Figures 3.10 and 3.11, for the two stationary solutions corresponding to  $\tilde{\gamma}$  positive and negative with  $\beta < 0$ . In Figure 3.10,  $\tilde{\gamma}$  is positive  $\beta < 0$ ,  $\alpha = 0$  and the real and imaginary parts of  $\sigma$  are plotted versus  $\gamma$ . Notice that below a threshold,  $\gamma_u \simeq 0.254|\beta|$ , the real part of  $\sigma$  remains zero, and the imaginary part grows with increasing  $\gamma$ . However, at  $\gamma_u$ , the imaginary part has a vertical tangent, and a new branch of  $\sigma$  emerges with growing real and imaginary parts as  $\gamma$  increases past  $\gamma_u$ . For  $\gamma > \gamma_u$ , the eigenvalue's real part becomes positive, resulting in instability to this discrete mode. When  $\alpha \neq 0$ , the real part of the eigenvalue shifts down so that the point of intersection of the eigenvalue branch with the  $\sigma_r = 0$  line,  $\gamma = \gamma_u(\alpha, \beta)$ , increases with increasing  $\alpha$ . A plot of the critical line,  $\gamma = \gamma_u(\alpha, \beta)$ , above which the solution becomes unstable to the discrete spectrum, is shown and described in the following section. When  $\tilde{\gamma} > 0$  and  $\beta > 0$ , purely real, positive eigenvalues exist wherever the soliton exists for any  $\alpha \geq 0$ , so that the  $\tilde{\gamma} > 0$  soliton is unstable to the discrete spectrum for  $\beta > 0$ .

In Figure 3.11,  $\tilde{\gamma}$  is negative,  $\beta < 0$  and  $\alpha > 0$ . For this stationary solution, purely real, positive, eigenvalues exist throughout the parameter domain for *any* value of  $\alpha \geq 0$ . Therefore, the  $\tilde{\gamma} < 0$  solution is *always* unstable to the discrete spectrum.

The discrete mode stability results may be summarized as follows. For the stationary solution corresponding to  $\tilde{\gamma} < 0$ , unstable, discrete modes exist for *all* parameters for which the stationary solution exists, and therefore, this stationary

	$\tilde{\gamma} > 0$	$\tilde{\gamma} < 0$
$\beta > 0$	Always Unstable	Does not exist
$\beta < 0$	Stable for $\gamma < \gamma_u(\alpha, \beta)$	Always Unstable

Table 3.2: Discrete-spectrum stability results.

solution is always *unstable* to a discrete mode. For the stationary solution corresponding to  $\tilde{\gamma} > 0$  with  $\beta < 0$ , the solution is *stable* to discrete modes for  $\gamma < \gamma_u$  and is *unstable* for  $\gamma > \gamma_u$ , where  $\gamma_u(\alpha, \beta)$  is computed numerically. Lastly, when  $\beta > 0$ , the  $\tilde{\gamma} > 0$  solution is always unstable to the discrete spectrum. Table 3.2 summarizes the stability response to the discrete spectrum.

### Perturbation Expansion for the Discrete Spectrum

To verify, analytically, the existence of the discrete-spectrum branch found using the numerical matching scheme and to start the numerical scheme along a solution branch, it is possible to construct solutions to Equation 3.10 for  $\tilde{\gamma}$  near zero, using a perturbation method. For  $\alpha$  small and  $\tilde{\gamma}$  small, there are four branches that emerge from the  $\tilde{\gamma} = 0$  point, as described in Appendix D. One branch has  $\bar{\sigma} = 0$ . Another has  $\bar{\sigma} = -2\bar{\alpha}$ . For the other two branches, the dependence of  $\bar{\sigma}$  on  $\tilde{\gamma}$  is found to be

$$\bar{\sigma} = -\bar{\alpha} \pm \sqrt{\bar{\alpha}^2 + 8\frac{\tilde{\gamma}}{\beta}} + O(\bar{\alpha}^2), \quad (3.19)$$

as shown in Equation D.11.

To illustrate the behavior of the eigenvalues branches, take  $\bar{\alpha} = 0$  and return to  $\sigma = \bar{\sigma}(-\beta + \tilde{\gamma})$ . The two branches given by Equation 3.19 reduce to

$$\begin{aligned} \sigma &= \pm 2\sqrt{2\beta\gamma} + O(\gamma) \quad \text{for } \tilde{\gamma} > 0, \quad \text{and} \\ \sigma &= \pm 2\sqrt{-2\beta\gamma} + O(\gamma) \quad \text{for } \tilde{\gamma} < 0. \end{aligned} \quad (3.20)$$

When  $\beta < 0$ , Equation 3.20 shows that the  $\tilde{\gamma} > 0$  solution leaves  $\gamma = 0$  with purely imaginary eigenvalues, while  $\tilde{\gamma} < 0$  leaves  $\gamma = 0$  with purely real eigenvalues. When  $\beta > 0$ , the  $\tilde{\gamma} < 0$  solution ceases to exist, and the  $\tilde{\gamma} > 0$  solution possesses purely real eigenvalues near  $\gamma = 0$ . Comparisons of the eigenvalues derived by the perturbation expansion with the results of the matching computation are shown in Figures 3.12 and 3.13. The agreement for small  $\gamma$  is quite good. The eigenfunctions for the approximate asymptotic solutions are known analytically and compare well to those computed using the numerical matching scheme.

### 3.2.3 The Complete Stability Picture

We can now combine the stability results of the continuous spectrum and the discrete spectrum to construct the complete linear-stability diagram for the two standing, solitary-wave, stationary solutions. The stationary solution corresponding to  $\tilde{\gamma} < 0$  was always found to be stable to the continuous spectrum and always *unstable* to discrete modes. Therefore, instabilities will always exist for this stationary solution, and the solution is generally *unstable* everywhere in the parametric domain.

The stationary solution corresponding to  $\tilde{\gamma} > 0$  was always found to be unstable to the continuous spectrum when  $\beta \geq 0$ . When  $\beta < 0$ , the solution is unstable to the continuous spectrum for  $\gamma > \sqrt{\alpha^2 + \beta^2}$ . The solution is unstable to discrete modes when  $\gamma > \gamma_u(\alpha, \beta)$ , where  $\gamma_u$  is computed numerically. The region of stability of the  $\tilde{\gamma} > 0$  mode can be conveniently plotted, for  $\alpha > 0$ , in the  $\bar{\gamma} \equiv \gamma/\alpha$  versus  $\bar{\beta} \equiv \beta/\alpha$  plane. Figure 3.14 shows the regions of linear stability and instability. The region labelled *I* is unstable to the continuous spectrum. Region *II* is unstable to the discrete spectrum. Region *III* is stable to

all small perturbations. Laedke and Spatschek found the instability that was due to the continuous spectrum as well as the instability for all  $\tilde{\gamma} < 0$ . However, the unstable, discrete mode was not found because their perturbation expansion in the region  $\beta < 0, \tilde{\gamma} > 0, \gamma < \sqrt{\alpha^2 + \beta^2}$  is for small  $\gamma$ . When the eigenvalue branch is continued numerically, the emergence of a positive real part can be seen. The stability of the stationary solutions along the  $\sigma = 0$  surfaces in the parameter space cannot be determined by the preceding linear theory. The stability analysis there must include the nonlinear terms that were initially neglected in the linearization.

### 3.2.4 Standing-Soliton Numerical Simulations

We may now compare the preceding linear-stability analysis with numerical solutions of the nonlinear Schrödinger equation (NLS), Equation 2.9. The above stability analysis provides an excellent platform for validation of a numerical code for solving the parametrically forced NLS equation. By choosing initial conditions near the stationary soliton solution and the system parameters in an unstable region, we should observe, in due time, the instabilities predicted by the foregoing theory with known eigenvalues. For unstable solutions, no superimposed initial perturbation is necessary, since any numerical code will have errors that provide a perturbation. For stable solutions, superimposed initial perturbations should decay, and the solution should approach the stationary solution. Lastly, the numerical simulations help to describe how the system behaves after instability occurs, information that cannot be ascertained from the preceding analysis.

Several numerical schemes have been developed to solve the parametrically forced NLS equation. The simplest scheme is a finite-difference scheme using a Runge-Kutta time step and central differences in space. A second scheme is

pseudospectral, using Fourier transforms and time marching in phase space. The invariants given for  $\alpha = 0$ , Equations 2.11, provide a test for numerical accuracy when  $\alpha = 0$ . Deviations from their constant value indicate numerical instability. The results shown here are produced using a finite-difference scheme in  $\xi$  space, with second-order central differences in  $\xi$  and a fourth-order Runge-Kutta time-marching method. Boundary conditions on  $\xi$  are  $\frac{d}{d\xi}\Psi = 0$  at  $\xi = \pm\ell/2$ , where  $\ell$  is much larger than the characteristic length of the soliton. When  $\alpha \neq 0$ , the numerical code is quite stable, allowing for large steps ( $\Delta t = 0.2$ ) in the nondimensional time. When  $\alpha = 0$ , the time step needs to be reduced considerably in order to obtain numerical stability. In the presentation of the simulations, the evolution of the solution of the envelope is shown as a three-dimensional plot in  $\xi$  and  $\tau$ . A plot of the evolution of a point fixed in  $\xi$  with time,  $\tau$ , follows, demonstrating the nature of the eigenvalue and allowing for comparison with the analysis.

The first series of simulations examines the stability of the  $\tilde{\gamma} < 0$  stationary solution. In this case,  $\beta < 0$  and  $\gamma^2 < \alpha^2 + \beta^2$ , and the soliton is predicted to be unstable to bound modes. Figure 3.15 shows the evolution of the soliton envelope in time as computed from the nonlinear Schrödinger Equation for fixed  $\alpha, \beta$ , and  $\gamma$  falling within this region. The case shown in the figure is characteristic of the evolution when the parameters fall in this region. Figure 3.16 shows the eigenfunction computed from the matching scheme for the bound mode described above. The predicted eigenfunction is in good agreement with the growth observed in Figure 3.15. Lastly, Figure 3.17 compares the growth rate observed from the nonlinear evolution with that predicted by the bound-mode instability, again showing good agreement for small times. As the solution evolves for long times, it decays and

approaches the flat surface. From the linear-stability analysis of the flat surface, we know that the flat-surface solution is stable when  $\gamma < \sqrt{\alpha^2 + \beta^2}$ .

The second series of simulations examines the stability of the  $\tilde{\gamma} > 0$  stationary solution. When  $\beta \geq 0$ ,  $\gamma \geq \sqrt{\alpha^2 + \beta^2}$ , and the solution is unstable to the continuous spectrum, as shown in Figure 3.18. Notice that the instability tends to create neighboring disturbances. Figure 3.19 shows a time history of a single point along the  $\xi$  axis. For small times, the solution grows away from the stationary solution exponentially, and the maximum growth rate may be compared to that predicted by Equation 3.15 as shown in the figure. The comparison is good for small times, when the deviation of the solution from the stationary solution is small. For longer times, the direct simulation shows that the growth is capped by nonlinear effects. In this case, the solution evolves into a cnoidal-wave solution of the NLS equation, one of the solutions found in Chapter 2.

For  $\tilde{\gamma} > 0$  and  $\beta < 0$ , the solution may be stable, unstable to the discrete spectrum, unstable to the continuous spectrum, or unstable to both. Figure 3.20 shows the evolution of the stationary solution when the parameters fall into region *I*, of Figure 3.14, unstable to the continuous spectrum. Again, the solution evolves into a system of neighboring disturbances, and the maximum growth rate may be compared to that given by Equation 3.18. Figure 3.21 shows the region of the stability diagram in which the parameters fall for this case. Figure 3.22 shows the time evolution of a point fixed in  $\xi$  compared with the growth rate predicted by the linear theory. Here the predicted growth rate is purely real. The agreement between the theory and the simulation is good for small times. As the solution grows away from the soliton solution, the linear theory will be a poor

approximation, and we expect deviation from the theory for longer times. For the continuous-spectrum instability, the system grows away from the stationary soliton and towards a cnoidal-wave solution of the NLS equation.

When the parameters fall into region *II* of Figure 3.14, the solution is unstable to the discrete mode. Here, the solution grows with an oscillatory component, and the tendency is for the solution to peak, as seen in Figure 3.23. The region of the stability diagram giving rise to these bound-mode instabilities is shown in Figure 3.24. The eigenvalue for the growing mode in this region may be computed using the Frobenius matching scheme and compared to the oscillatory growth of the nonlinear evolution, as shown in Figure 3.25. The agreement is good for small times. The solution approaches the flat surface after experiencing the instability that is due to the discrete spectrum. The linear-stability analysis of the flat surface shows that it is stable in this case.

Lastly, we choose parameters in the stable region, region *III*. The evolution of the nonlinear Schrödinger equation is shown in Figure 3.26. Here, the small initial disturbances are seen to decay with an oscillatory component, and the stationary solution is approached, as predicted. The region of the stability diagram leading to stable solitons is shown in Figure 3.27. Figure 3.28 shows the time evolution of a point fixed in  $\xi$  compared with the eigenvalue found by the preceding theory. The agreement in this case is excellent since small perturbations become smaller, thereby keeping the system within the assumptions made for the linear-stability analysis.

A very interesting phenomenon occurs when the parameters lie in region *II* (unstable to bound modes) but near region *III* (stable) of Figure 3.14. The linear-

stability theory here predicts that the stationary solution will be unstable to bound modes. The instability has an oscillatory component, and the eigenfunction tends to focus the energy towards the peak of the soliton. When the full, nonlinear evolution equation is computed, we find that initially we have growth away from the stationary solution as predicted. However, when the perturbation grows to be sufficiently large, we find that the growth is capped, and the flow approaches a periodic orbit about the stationary solution. The numerical solution for this case is shown in Figure 3.29, with the appropriate region of the stability diagram shown in Figure 3.30 and the time evolution of a point fixed in  $\xi$  shown in Figure 3.31. The capping of the solution after initial growth is the result of the nonlinear terms not included in Equation 3.9. The linear theory is a good approximation for small times, so that the solution grows initially. However, as the solution grows away from the soliton solution, the nonlinear terms neglected in the linearization of the NLS equation become large and bound the motion, leading to a solution that is periodic in the slow time. The periodic orbit cannot be predicted using the linear-stability analysis alone, and its identification is a nice result of the direct simulation.

### 3.2.5 Standing-Soliton Experiments

Experiments were performed to investigate the standing solitary-wave stability and to evaluate the theoretical and numerical results. Several tanks were used, each rectangular in cross section and constructed from acrylic. Vertical sinusoidal oscillations were provided by an electromagnetic shake table with a linear potentiometer attached to the driving surface, giving drive displacement. A resistive-type wave gauge was used to measure surface elevations. The liquid used in the experiment

was distilled water, with several drops of Kodak Photo-Flo to decrease the tendency of the water to pin against the walls. Surface tension of the water was also measured. The frequency-detuning parameter,  $\beta$ , is given by

$$\begin{aligned}\beta &= \frac{\omega^2 - \omega_o^2}{2\omega_o^2}, \\ \omega_o &= \sqrt{gk \tanh(kh)(1 + \sigma_t)}, \\ \sigma_t &= \frac{k^2 T}{\rho g}, \quad k = \frac{\pi}{b},\end{aligned}$$

where  $T$  is the surface tension of the water,  $\rho$  is the density of the water,  $b$  is the width of the tank,  $h$  is the undisturbed water depth,  $g$  is the constant acceleration that is due to gravity, and  $\omega$  is one half of the drive frequency. The forcing parameter,  $\gamma$ , is given by

$$\gamma = \frac{a_o \omega^2}{g},$$

where  $a_o$  is the drive amplitude. Hence,  $T$ ,  $\rho$ ,  $b$  and  $h$  are known and fixed for a given run, and  $\omega_o$ , the natural frequency of the  $(0, 1)$  mode, may be computed. The drive frequency,  $2\omega$ , is measured using a frequency counter, and the drive amplitude,  $a_o$ , is measured using the linear potentiometer. The remaining parameter,  $\alpha$ , is measured by finding the  $\gamma$  for which motion ceases to exist. This minimum forcing, from the preceding theory, is equal to  $\alpha$ . The forcing-frequency measurement had an uncertainty of two percent. The plate-displacement measurement had an uncertainty of six percent, because of sticking of the potentiometer at its extremum, particularly at small drive displacements. Wave amplitudes were accurate to five percent.

The effects of friction are represented in the preceding theory by the single parameter,  $\alpha$ . In the laboratory, several frictional effects are present. First, the presence of viscosity in the liquid leads to boundary layers on the tank walls and

bottom as well as the free surface. The boundary layers on the tank walls have a thickness on the order of one millimeter. Contaminants on the free surface also contribute to frictional losses. Lastly, the motion of the interface consisting of the liquid, the air and the tank wall is hysteretic, and there are frictional losses at this interface. The liquid advancing on a dry wall behaves differently than the liquid receding down the wall. All of these frictional effects are absorbed into the single parameter,  $\alpha$ , which is obtained experimentally. The functional form of  $\alpha$  may be motivated, however we do not attempt a rigorous derivation of the form of each of the foregoing frictional effects.

First, the stability boundaries for the standing solitary wave with  $\beta < 0$  and  $\tilde{\gamma} > 0$  (the only case possessing stable solutions) were experimentally identified. These boundaries were loosely identified in the original paper by Wu et al. (1984). The method is to fix  $\beta$  and put  $\gamma$  inside the stable region of Figure 3.14, region *III*. Within this region, the soliton is generated by sloshing a small paddle inside the tank. Once a stable soliton is produced,  $\gamma$  is slowly reduced until the forcing can no longer overcome the frictional effects. By averaging the minimum  $\gamma$  for varying  $\beta$ , we find  $\alpha$ . Next, the stable soliton is again generated, and  $\gamma$  is slowly increased until the soliton becomes unstable and gives way to a new solution. The process is then repeated for a new  $\beta$ .

Figure 3.32 shows the experimental results plotted in the  $\beta/\alpha$  versus  $\gamma/\alpha$  plane for a tank width,  $b$ , of 2.5 cm. Figure 3.33 shows the result for a tank width of 5.0 cm. Outside the filled dots, the soliton ceases to exist. When  $\gamma/\alpha < 1$ , the forcing is insufficient to overcome friction. When  $\gamma/\alpha$  is above the dots, the soliton has become unstable. The two sets of data represent two different tank

sizes. As expected, no solitons are observable for  $\beta > 0$ . When the parameters lie in region *i* of the figures, the wave goes unstable to the continuous spectrum, and the agreement between the theory and the experiment is quite good. As predicted by the numerical simulations, the soliton in the laboratory goes unstable by continually generating neighboring disturbances, eventually developing into a cnoidal wave solution. Region *ii* of the figures indicates points at which the soliton goes unstable to discrete-spectrum instabilities. Here, the soliton increases in amplitude and decreases in breadth until it breaks down and the system tends toward the flat surface, in agreement with the numerical predictions. Region *iii* of the experimental stability figures is the region in which the soliton is completely stable. Here the envelope is stationary in the slow time.

Lastly, region *iv* of the figures is a region possessing the slow-time, periodic, envelope solutions predicted by the direct, numerical simulations. In this region, the solution initially grows away from the soliton and approaches a slow-time periodic solution. We observe a breathing period for the wave in this region, where the wave focuses and peaks, followed by decay and spreading. The boundary of this breathing region has not been determined analytically. Notice that the boundary of the periodic solutions in the stability diagram differs for the two different tank widths. This difference points to the influence of nonlinear terms in the capping of the growth predicted by the linear theory. The parameter  $kh$ , different for the two tanks, does not play a role in the linear-stability theory. However, when the solution grows away from the soliton, the linear approximation breaks down and the nonlinear terms become important. These nonlinear terms depend upon  $A(kh)$ , so that the different-sized tanks should have a different response for the

periodic solutions.

When the parameters fall within the region leading to instability to eigenvalues in the continuous spectrum, we can measure the maximum growth rate of the unstable modes by placing a wave gauge in the region neighboring a stable soliton and increasing  $\gamma$  into the unstable region. A sample time trace for a wave gauge so positioned is shown in Figure 3.34. By computing the growth rate from the wave gauge output, having measured  $\gamma$  and  $\beta$ , a comparison between the theoretically predicted growth rate and the observed one can be made. The results of such a comparison are shown in Figure 3.36. The solid line represents the maximum growth rate given by Equation 3.18, while the dots represent measured growth rates for many experimental runs. When  $\beta$  and  $\gamma$  are small, the agreement is very good. For larger values of  $\gamma$ , the theoretical prediction overshoots the experimental evidence. There are two probable causes for the overprediction by the linear theory. First, the losses that are due to the liquid's advancing on a dry wall is not included in the theory and is sure to reduce the measured growth rate with respect to the theoretical case. Second, the nonlinear terms neglected in the linear analysis bound the exponential growth, so that as the wave grows away from the stationary solution, the actual growth rate is smaller than that predicted by the linear theory. For higher-growth rates, it is reasonable to expect greater disagreement with the theory, since higher-growth rates lead to higher amplitudes. A combination of the two effects is responsible for the overprediction seen in the figure.

A wave gauge time history for a solution whose envelope is periodic in slow time is shown in Figure 3.35. The wave gauge is placed at the soliton peak. The fast oscillation in the trace is due to the fast-time sloshing ( $\sim 5$  Hz), while the slow

modulations are due to the breathing ( $\sim \frac{1}{5}$  Hz). The breathing phenomenon was also observed in the numerical simulations of the nonlinear Schrödinger equation, Figure 3.29.

For large values of  $|\beta|$ , the flat parts of the free surface become unstable to longitudinal modes that compete with the sloshing mode of interest. The effect of this interaction is beyond the range of validity of the theory presented here and represents the boundary between the small detuning approximation and the linear theory of Benjamin and Ursell (1954) for finite forcing and detuning. The frequencies and forcing amplitudes at which the plane free surface becomes unstable to modes other than the (0,1) mode can be computed, using their result. The inception of unstable, longitudinal modes may be delayed by putting wave-absorbing material at the tank ends.

The experimental results for the standing soliton are summarized as follows. For small detuning and small forcing amplitude, the instability that is due to the continuous spectrum of the linear-stability equations accurately describes the physical situation. Envelope solitons, in this case, lose stability to sloshing waves modulated by a cnoidal-type envelope, in agreement with numerical simulations of the NLS equation. The initial growth rates in this case compare well with those predicted by linear theory. When the parameters are in the region leading to the bound-mode instability, but near the boundary with the stable region, the soliton gives way to a slow-time, periodic solution, in which the envelope disturbance is localized in space and unsteady in slow time. For large, negative detuning, the soliton is unstable to the bound mode and may break or excite longitudinal modes in the tank, both of which are beyond the scope of the linear theory. No solitons

were observed for positive detuning, again in agreement with the theory.

### **Figures for Chapter 3**

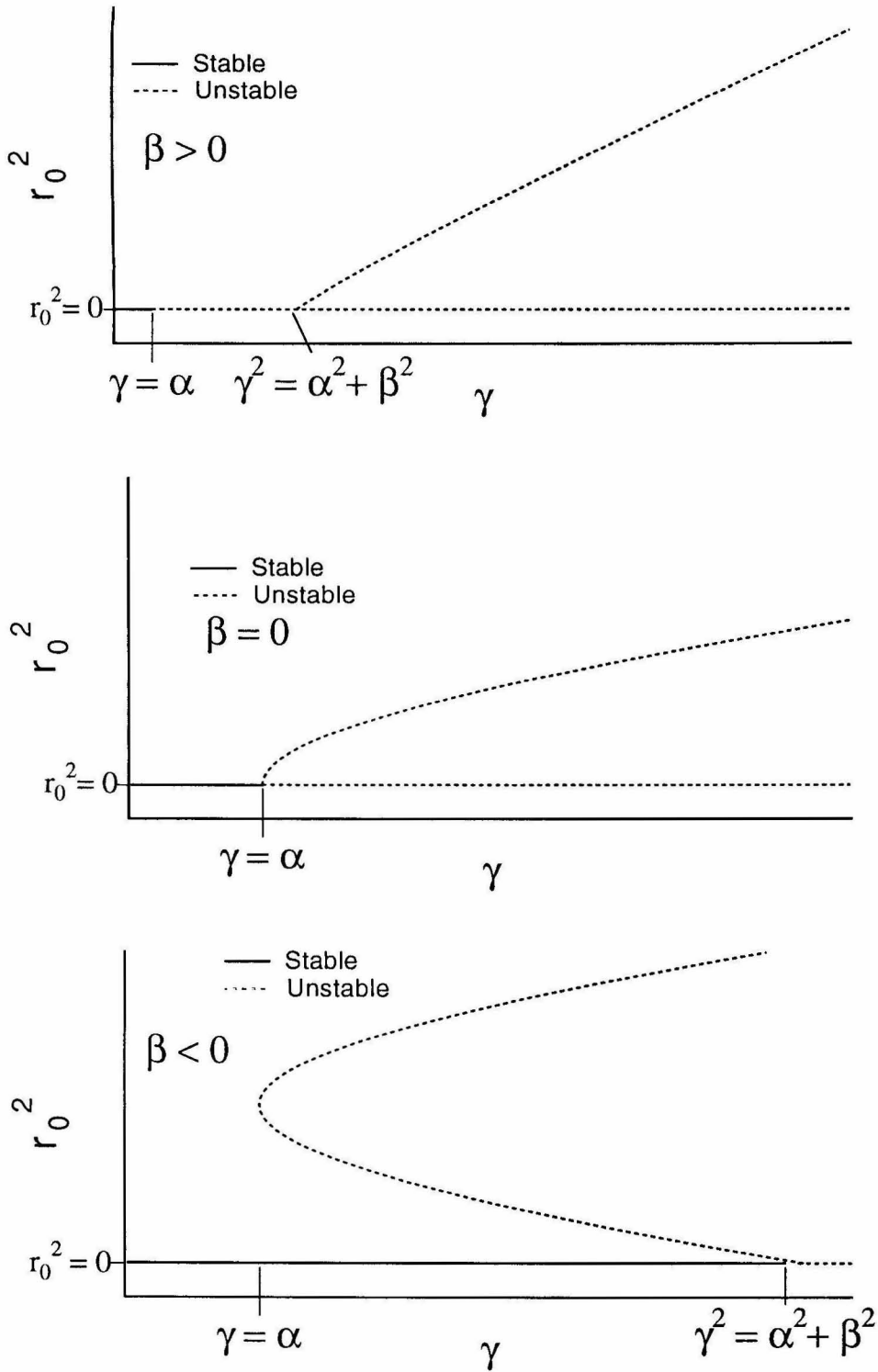


Figure 3.1: Solution branches of the  $\xi$ -independent solution. The amplitude,  $r_0^2$ , is plotted against  $\gamma$  for different values of  $\beta$  when  $A > 0$ .

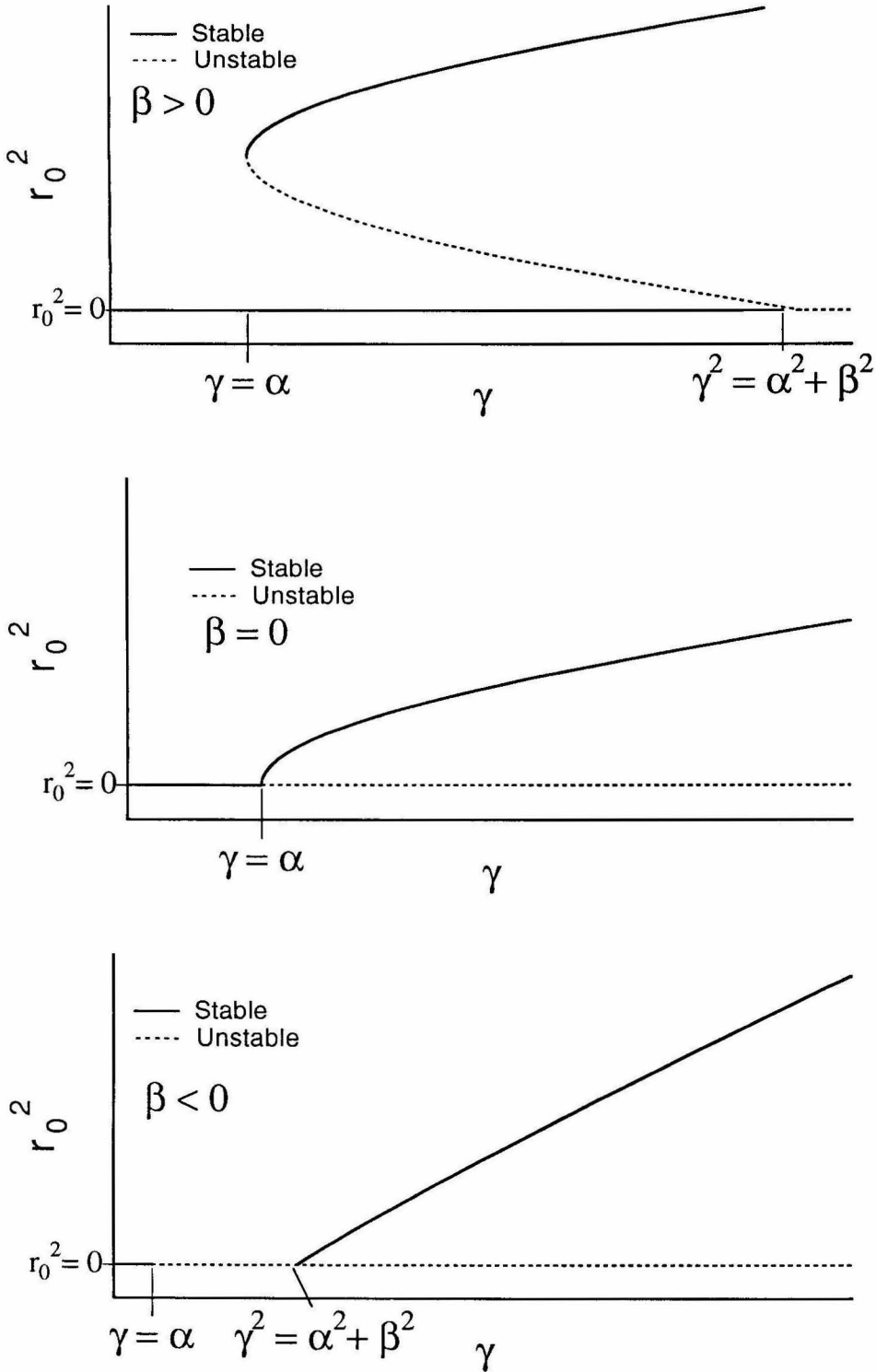


Figure 3.2: Solution branches of the  $\xi$ -independent solution. The amplitude,  $r_0^2$ , is plotted against  $\gamma$  for different values of  $\beta$  when  $A < 0$ .

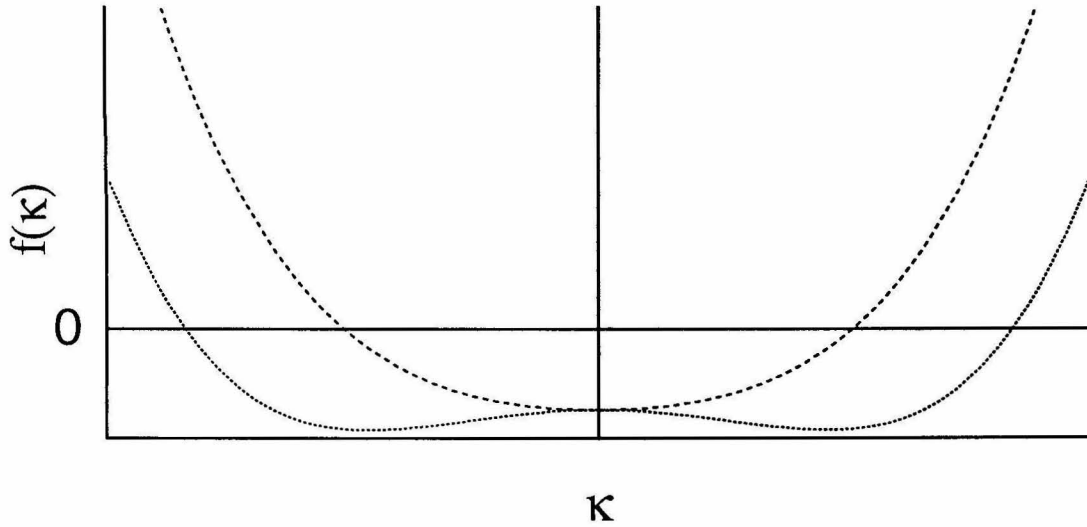


Figure 3.3: Possible curves for  $f(\kappa)$  when  $A > 0$  and  $\tilde{\gamma} > 0$ . If  $f(\kappa) < 0$ , the constant  $r_0$  solution will be unstable with wave number  $\kappa$ .

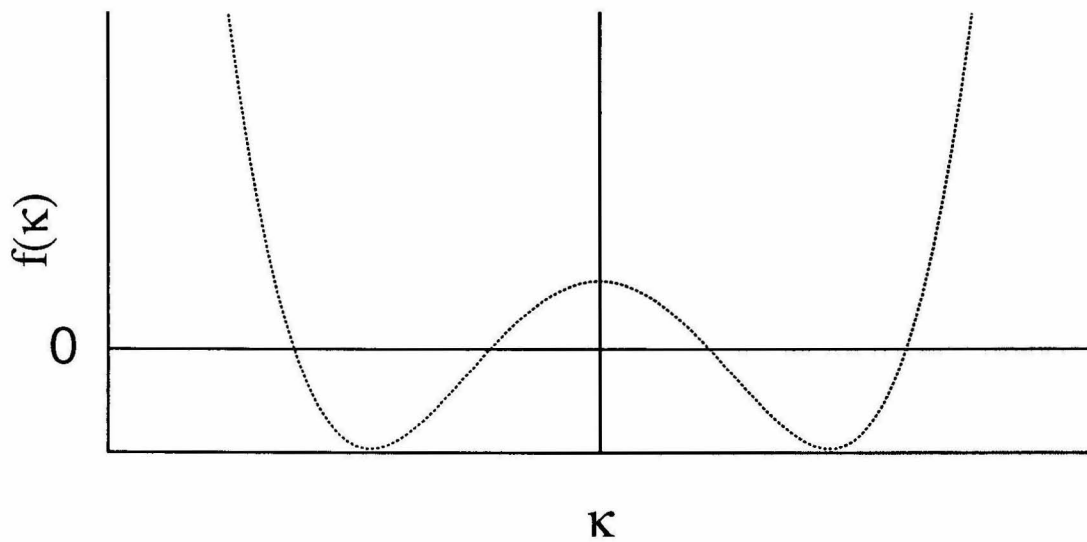


Figure 3.4: Possible curves for  $f(\kappa)$  when  $A > 0$  and  $\tilde{\gamma} < 0$ . If  $f(\kappa) < 0$ , the constant  $r_0$  solution will be unstable with wave number  $\kappa$ .

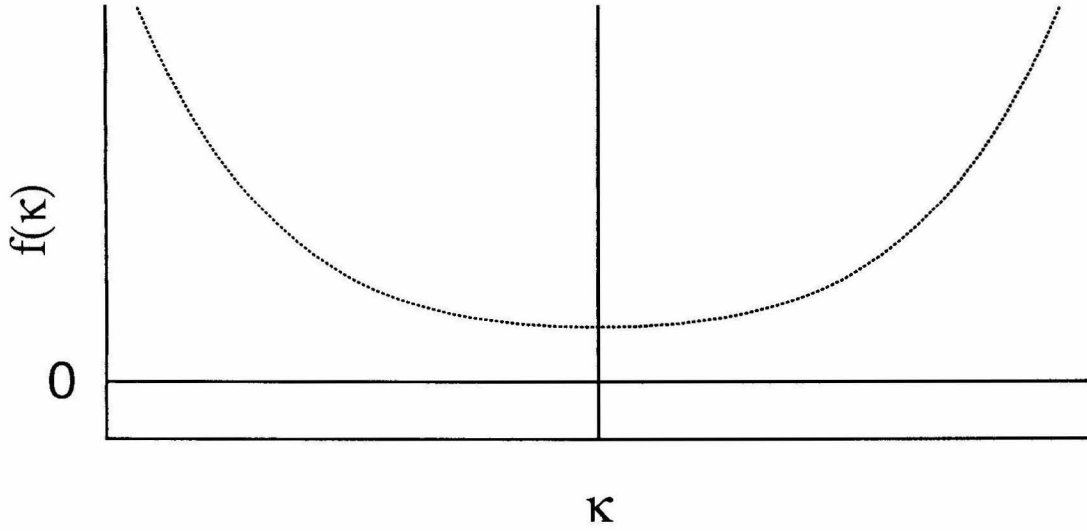


Figure 3.5: Possible curves for  $f(\kappa)$  when  $A < 0$  and  $\tilde{\gamma} > 0$ . If  $f(\kappa) < 0$ , the constant  $r_0$  solution will be unstable with wave number  $\kappa$ .

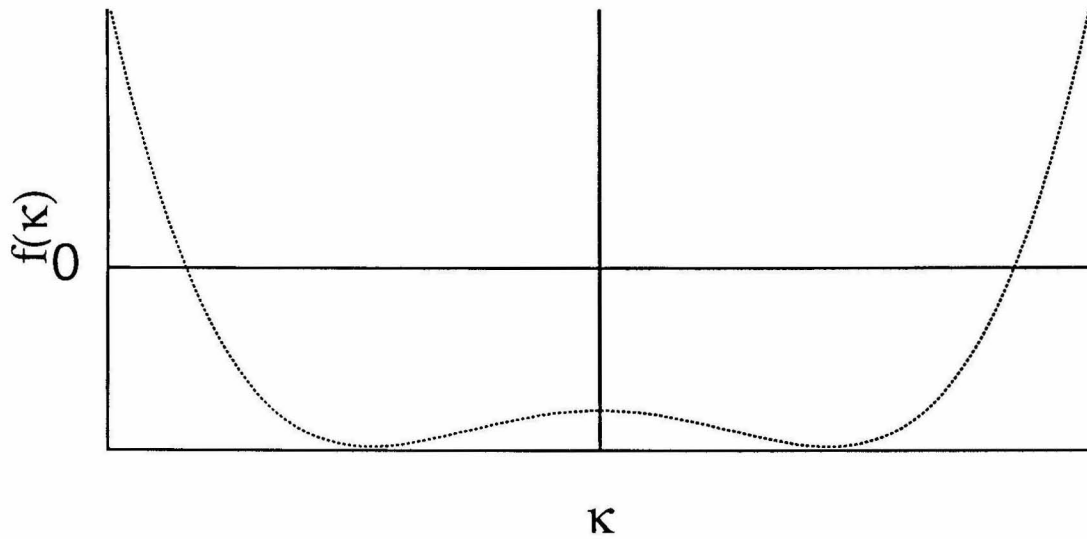


Figure 3.6: Possible curves for  $f(\kappa)$  when  $A < 0$  and  $\tilde{\gamma} < 0$ . If  $f(\kappa) < 0$ , the constant  $r_0$  solution will be unstable with wave number  $\kappa$ .

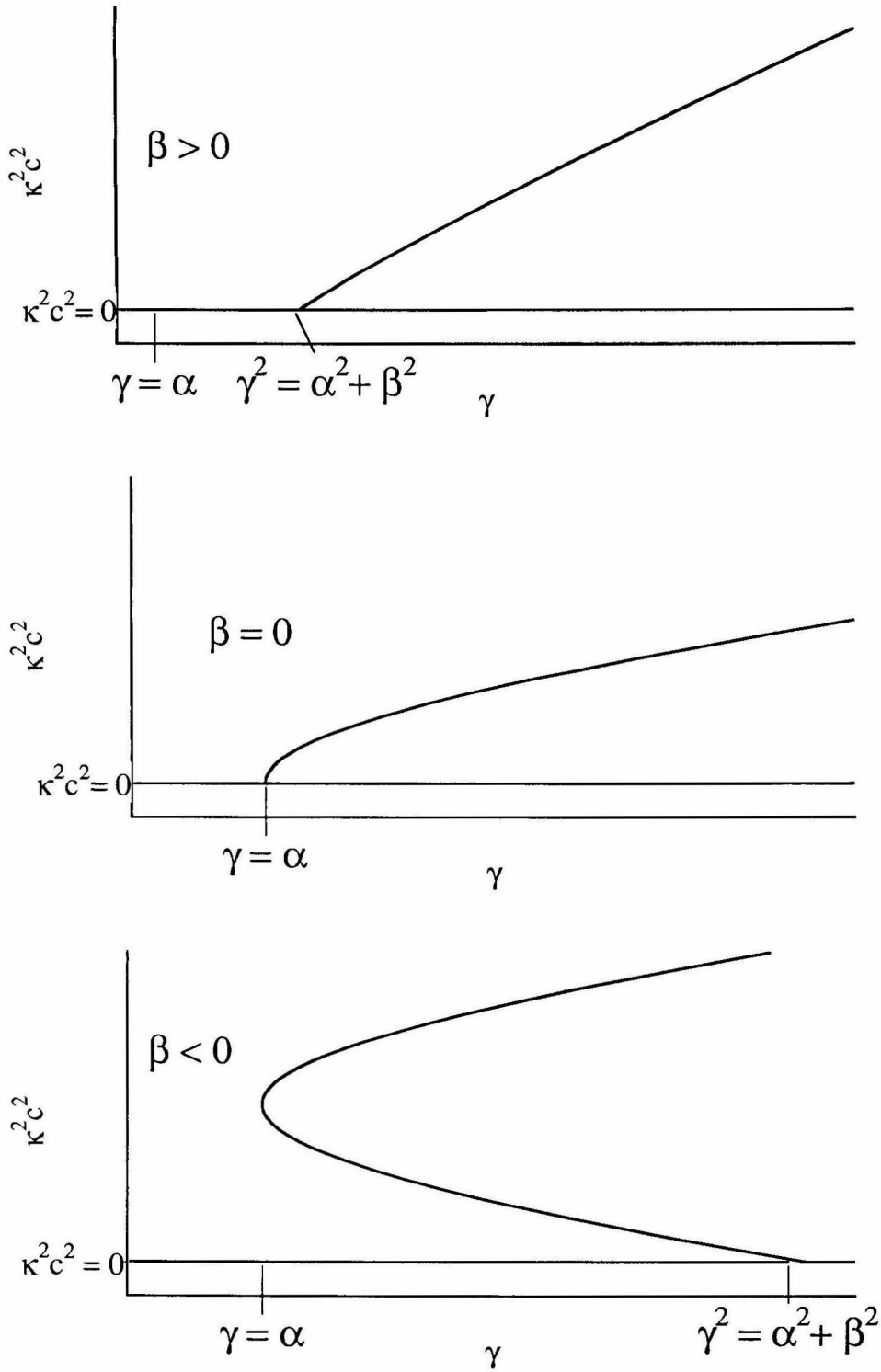


Figure 3.7: Stationary solution branches for the standing solitary wave. *a* :  $\beta > 0$ , *b* :  $\beta = 0$ , *c* :  $\beta < 0$ .

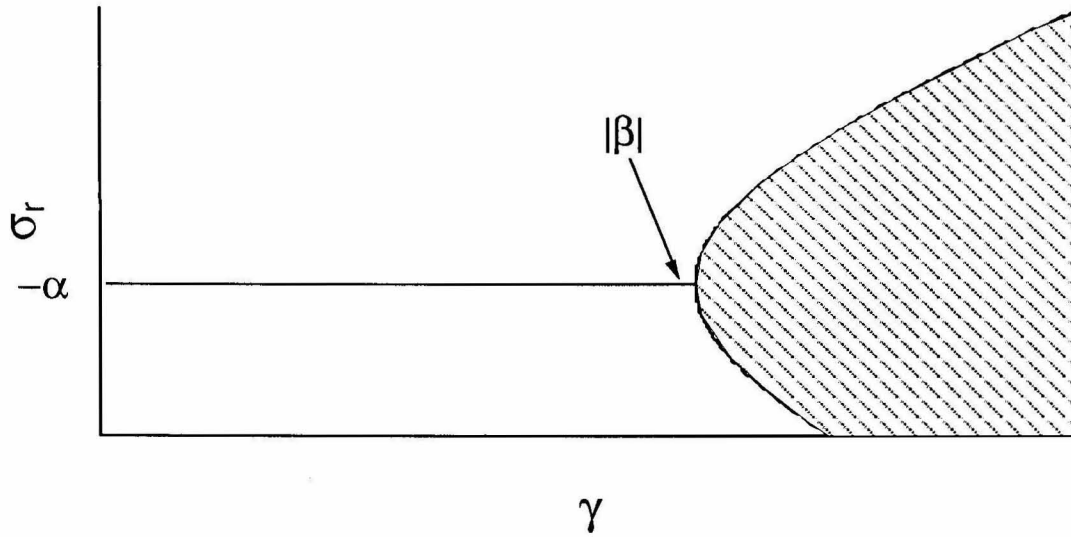


Figure 3.8: Eigenvalue regions giving rise to purely imaginary indices. Real part of the eigenvalue,  $\sigma_r$ .

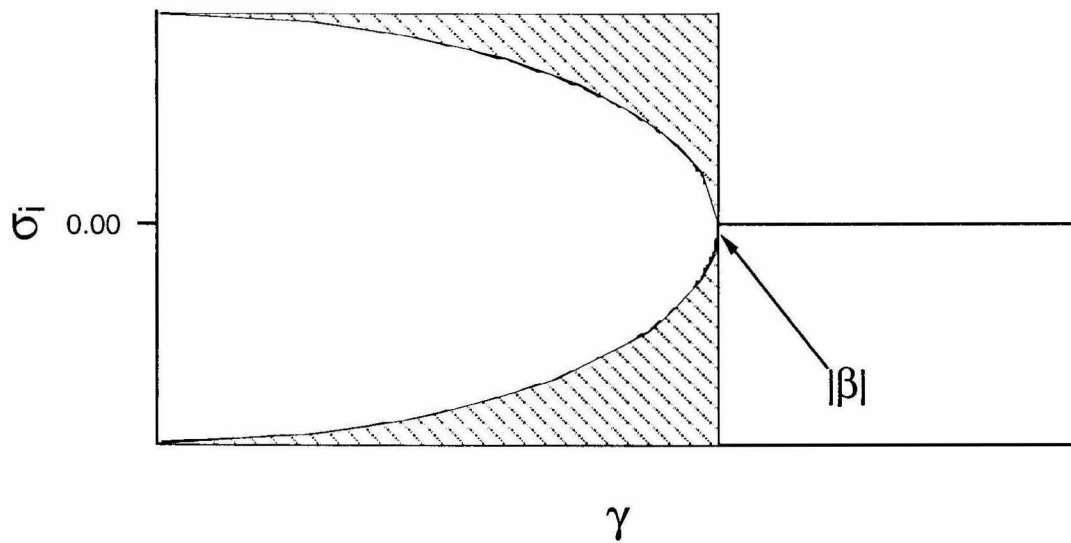


Figure 3.9: Eigenvalue regions giving rise to purely imaginary indices. Imaginary part of the eigenvalue,  $\sigma_i$ .

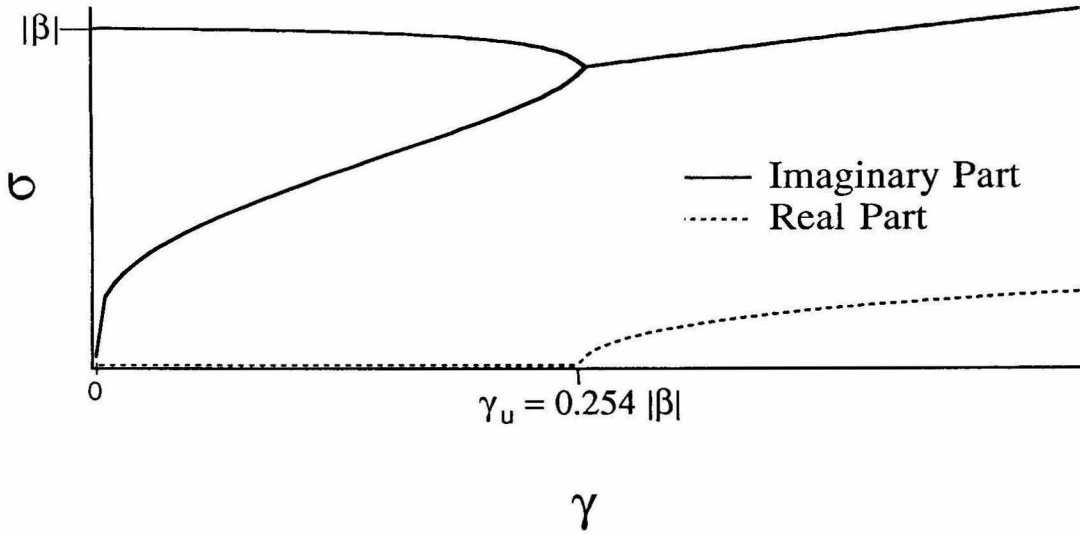


Figure 3.10: The complex eigenvalue,  $\sigma = \sigma_r + i\sigma_i$ , plotted against  $\gamma$ , for  $\alpha = 0$  and  $\beta = -1$ , when  $\tilde{\gamma} > 0$ .

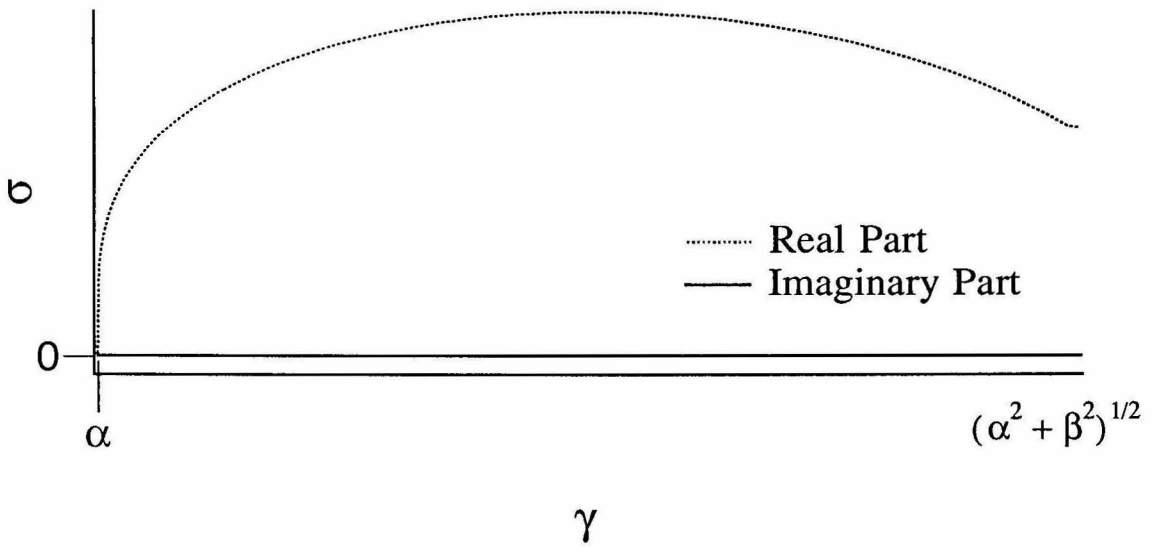


Figure 3.11: The complex eigenvalue,  $\sigma = \sigma_r + i\sigma_i$ , plotted against  $\gamma$ , for  $\beta = -1$ ,  $\tilde{\gamma} < 0$  and  $\alpha = 0.1$ .

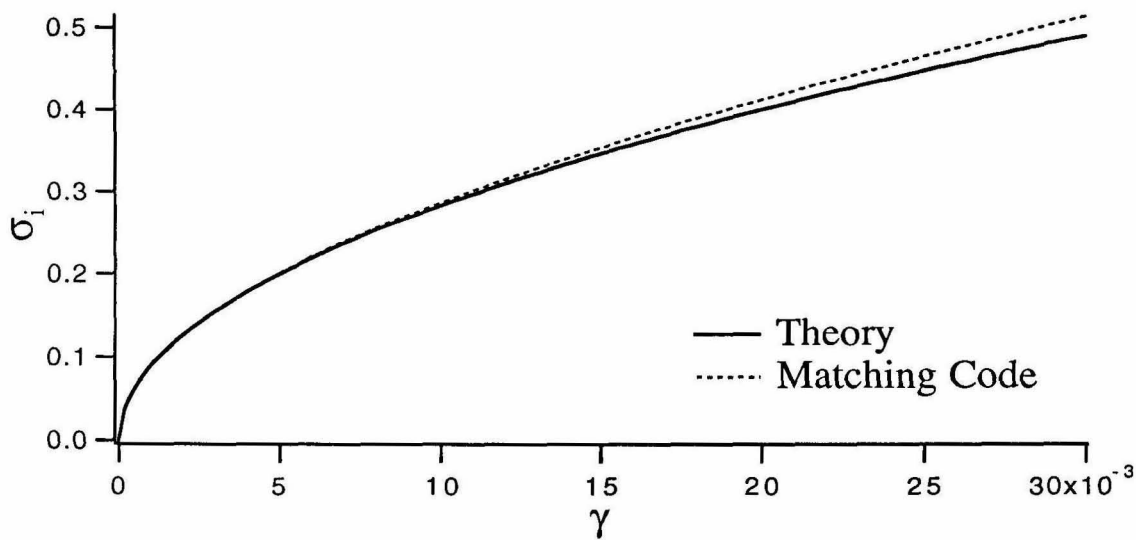


Figure 3.12: Comparison of perturbation expansion and matching computation of eigenvalue dependence,  $\sigma$  against  $\gamma$  for  $\alpha = 0$  and  $\beta = -1$  and  $\tilde{\gamma} > 0$ .

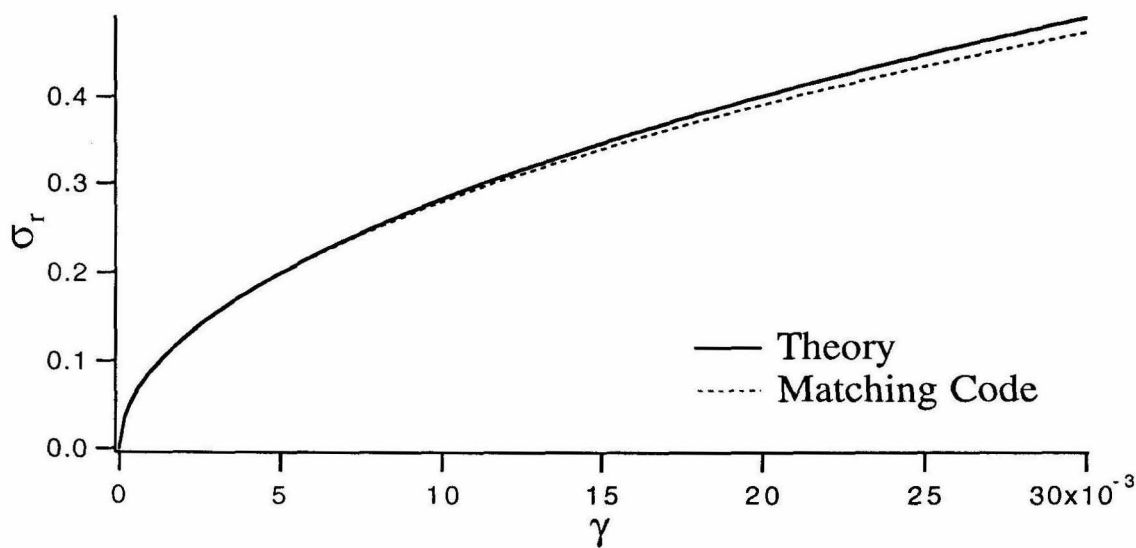


Figure 3.13: Comparison of perturbation expansion and matching computation of eigenvalue dependence,  $\sigma$  against  $\gamma$  for  $\alpha = 0$  and  $\beta = -1$  and  $\tilde{\gamma} < 0$ .

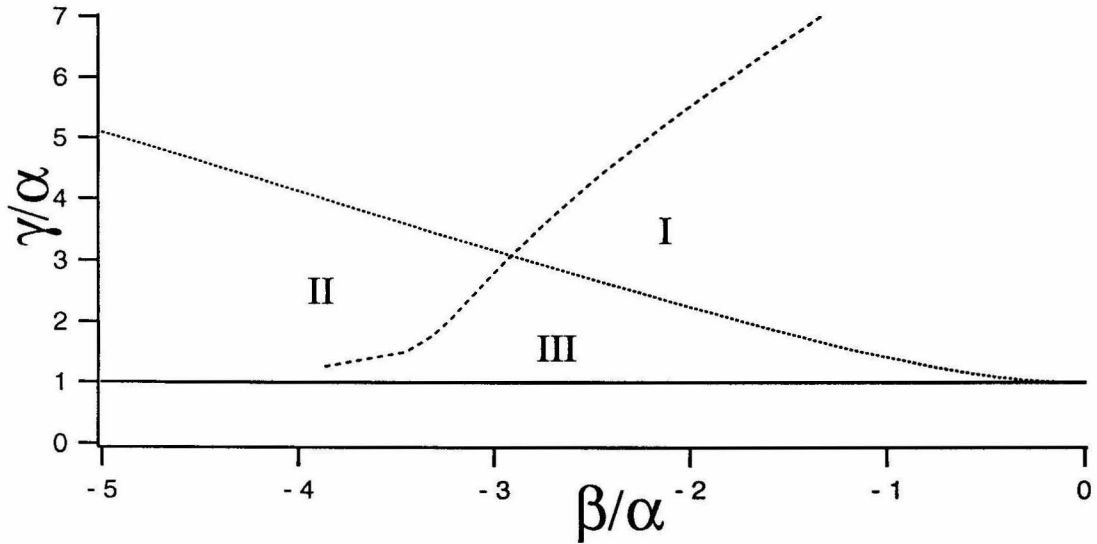


Figure 3.14: Stability diagram for  $\tilde{\gamma} > 0, \beta < 0$ . Region *I* is unstable to the continuous spectrum. Region *II* is unstable to the discrete spectrum, and region *III* is stable to all small perturbations.



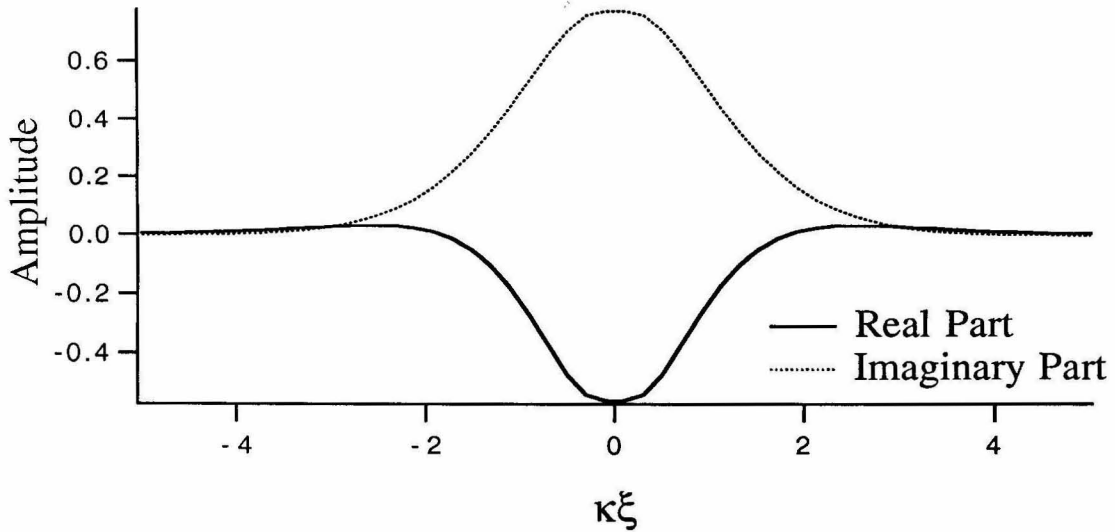


Figure 3.16: Evolution of NLS for  $\tilde{\gamma} < 0$ . The eigenfunction of the unstable bound mode. In this case,  $\beta = -1$ ,  $\gamma = 0.25$  and  $\alpha = 0.001$ .

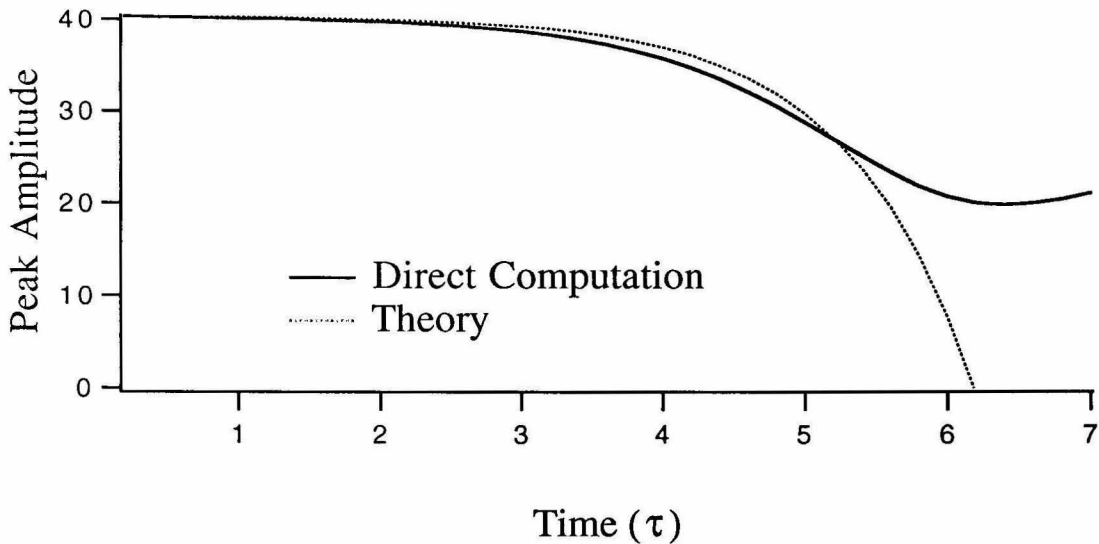


Figure 3.17: Evolution of NLS for  $\tilde{\gamma} < 0$ . Comparison of NLS growth rate to that predicted by linear theory. The evolution of a point fixed in  $\xi$  is shown as a function of time. In this case,  $\beta = -1$ ,  $\gamma = 0.25$  and  $\alpha = 0.001$ .

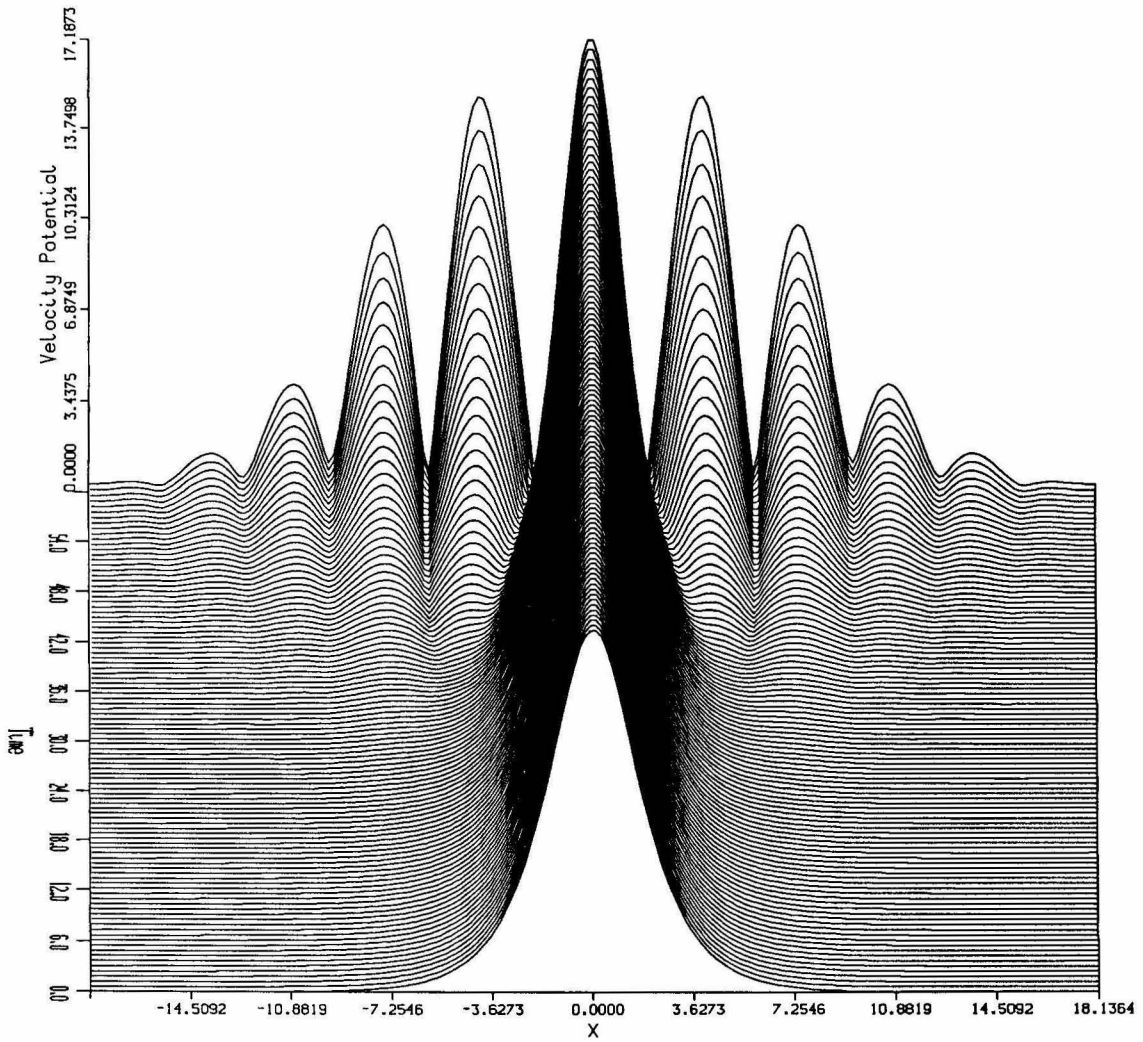


Figure 3.18: Nonlinear Schrödinger Equation evolution when  $\tilde{\gamma} > 0$ ,  $\beta > 0$ . For this plot,  $\beta = 0.145$ ,  $\gamma = 0.25$  and  $\alpha = 0.1$ .

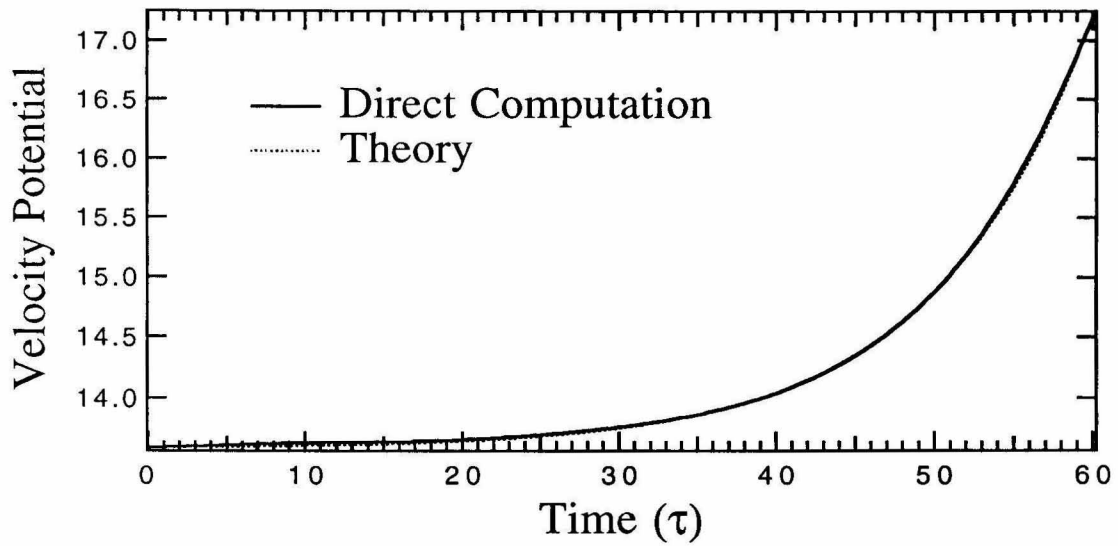


Figure 3.19: Nonlinear Schrödinger Equation evolution when  $\tilde{\gamma} > 0$ ,  $\beta > 0$ . Evolution of a point fixed in  $\xi$  with time. For this plot,  $\beta = 0.145$ ,  $\gamma = 0.25$  and  $\alpha = 0.1$ .

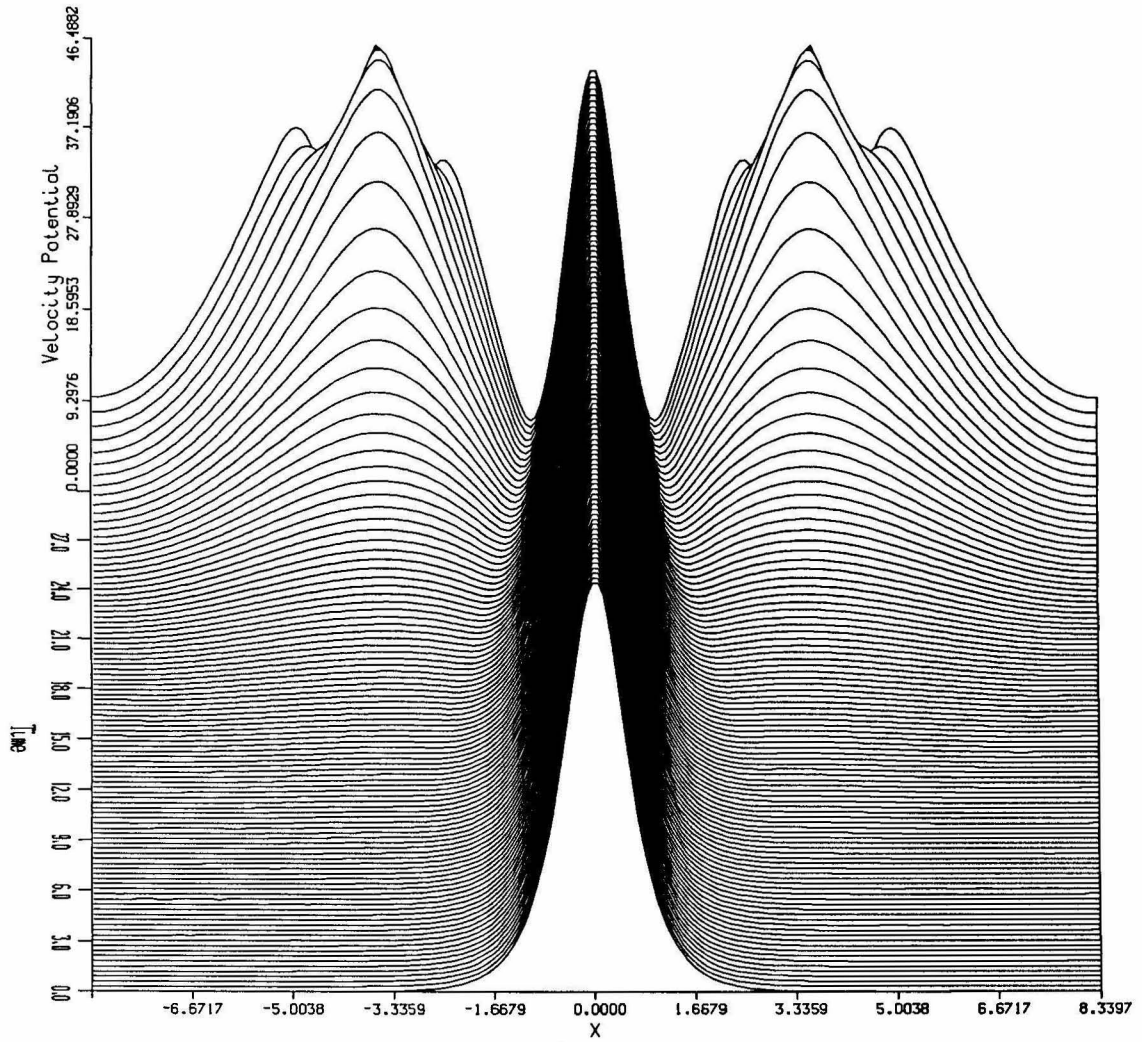


Figure 3.20: Wave evolution for  $\tilde{\gamma} > 0$ ,  $\beta < 0$ , when the soliton is unstable to the continuous spectrum. For this plot,  $\beta = -0.29$ ,  $\gamma = 0.5$  and  $\alpha = 0.1$ .

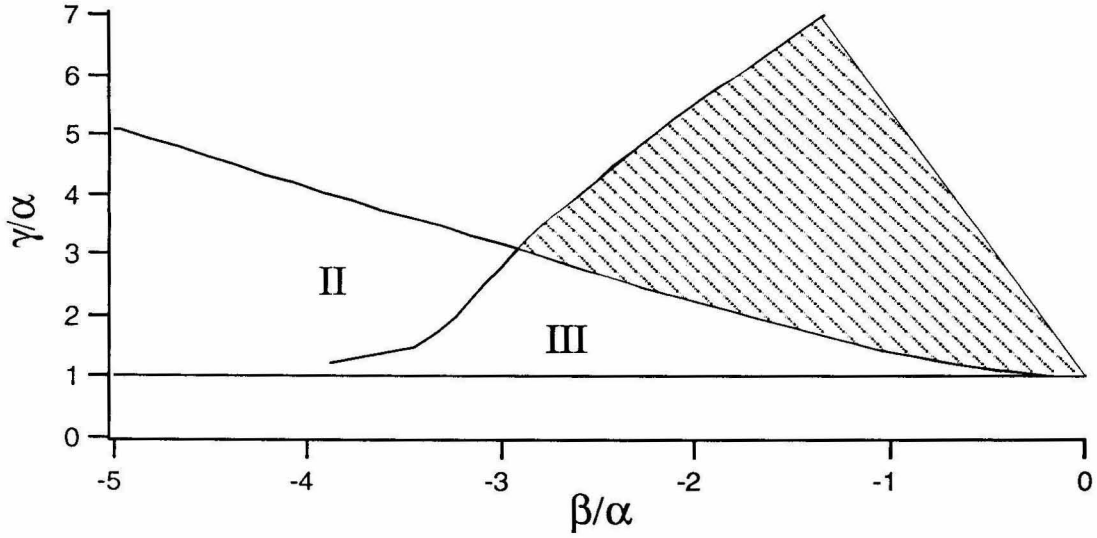


Figure 3.21: Region of the stability diagram in which the parameters lie when the soliton is unstable to the continuous spectrum.

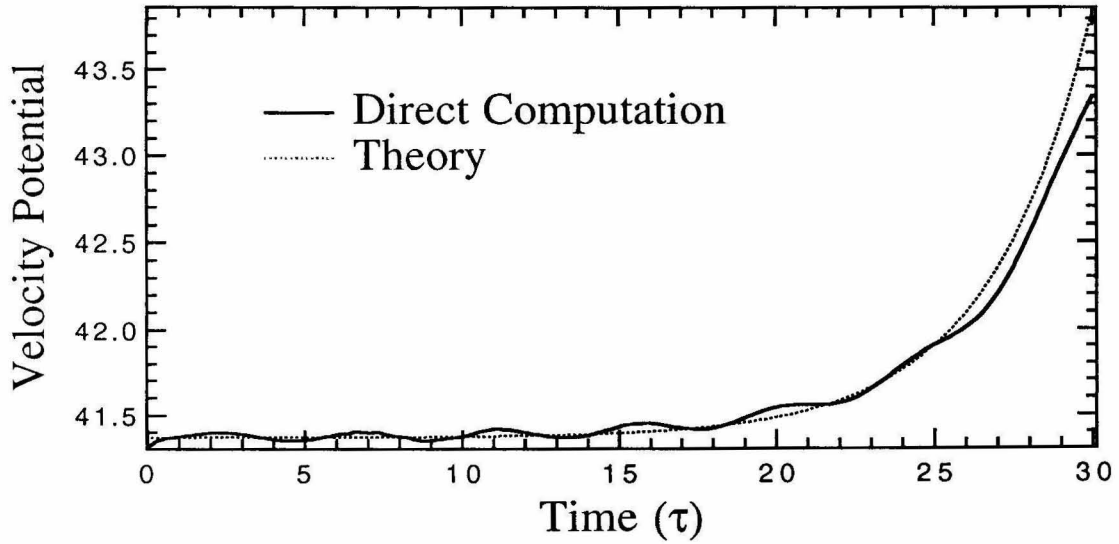


Figure 3.22: Evolution of a fixed point in time when the soliton is unstable to the continuous spectrum. The time and space evolution is shown in the preceding figures. For this plot,  $\beta = -0.29$ ,  $\gamma = 0.5$  and  $\alpha = 0.1$ .

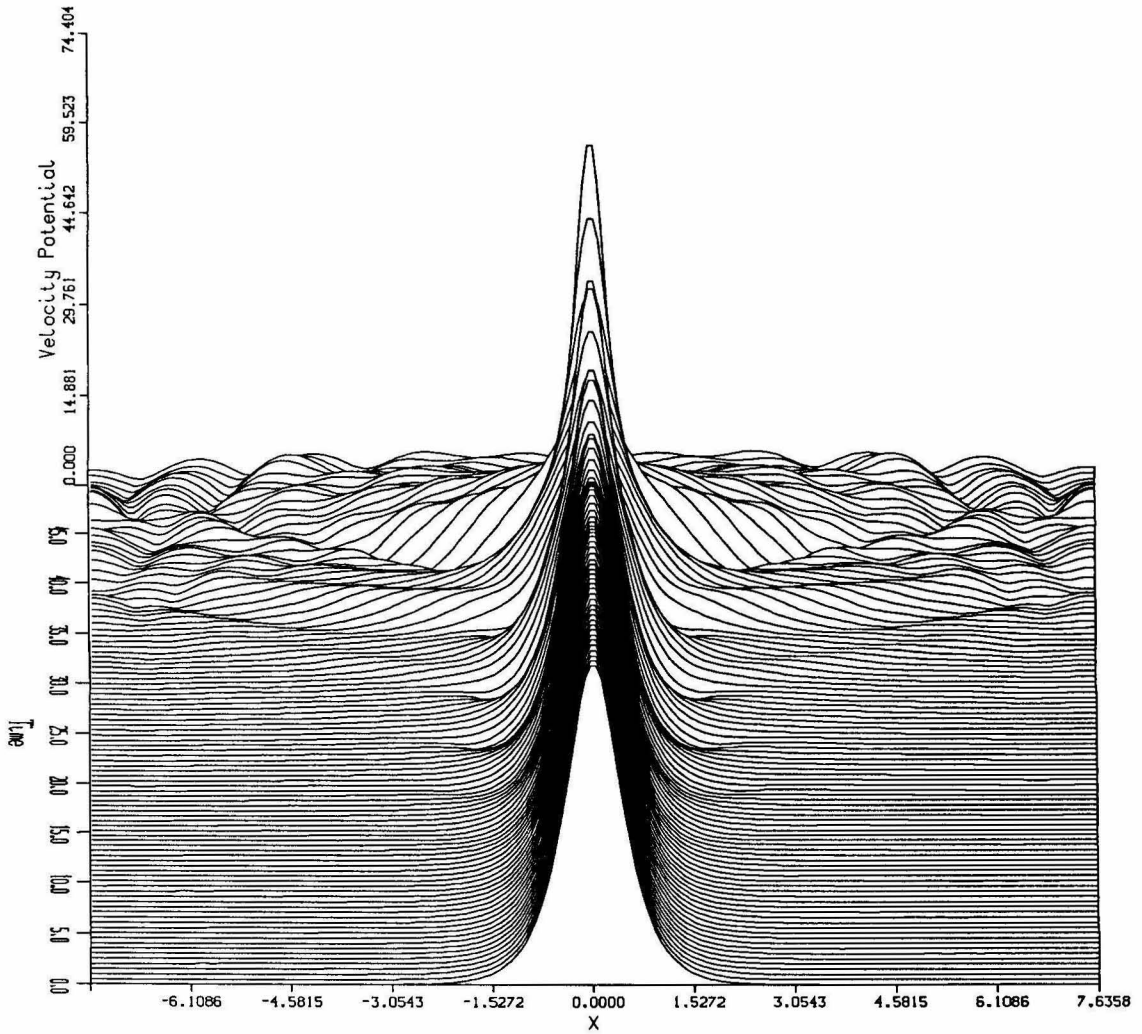


Figure 3.23: Wave evolution for  $\tilde{\gamma} > 0$ ,  $\beta < 0$ , when the stationary solution is unstable to the discrete spectrum. For this plot,  $\beta = -0.99$ ,  $\gamma = 0.25$  and  $\alpha = 0.1$ .

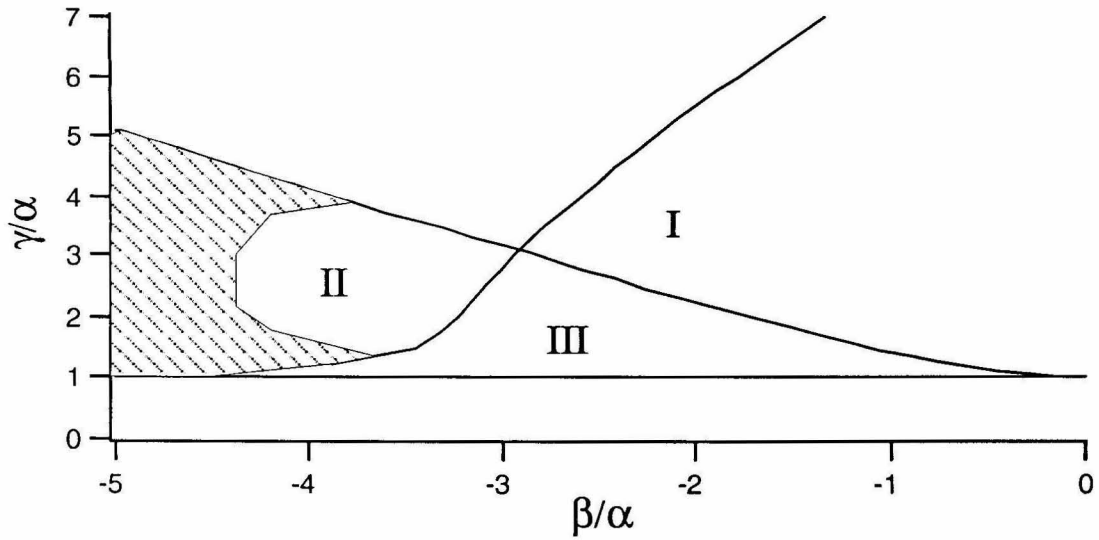


Figure 3.24: Region of the stability diagram in which the parameters lie when the stationary solution is unstable to the discrete spectrum.

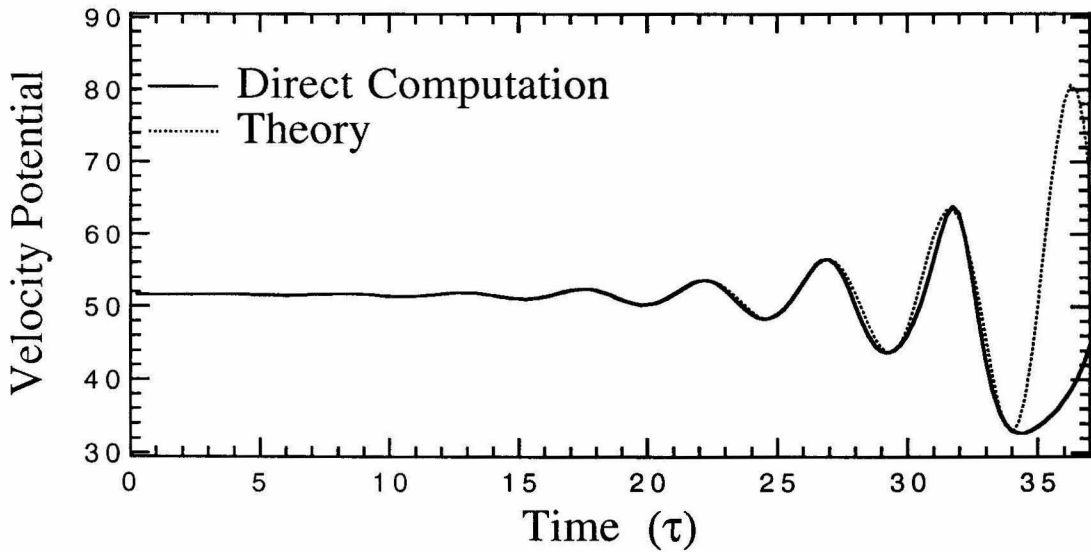


Figure 3.25: Evolution of a fixed point in time when the soliton is unstable to the discrete spectrum. The time and space evolution is shown in the preceding figures. For this plot,  $\beta = -0.99$ ,  $\gamma = 0.25$  and  $\alpha = 0.1$ .

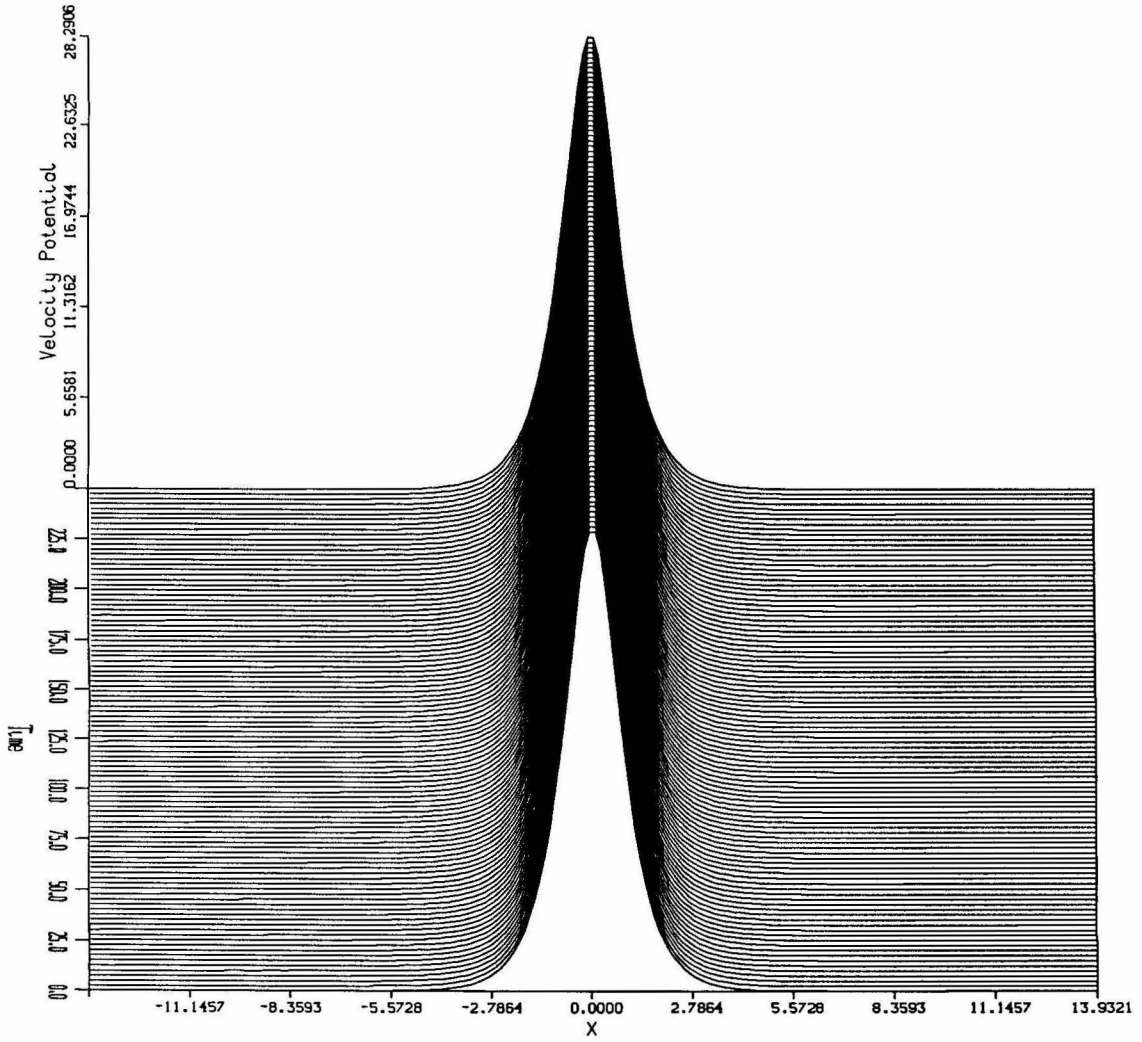


Figure 3.26: Wave evolution for  $\tilde{\gamma} > 0$ ,  $\beta < 0$ , when the stationary solution is stable to all small perturbations. For this plot,  $\beta = -0.29$ ,  $\gamma = 0.125$  and  $\alpha = 0.1$ .

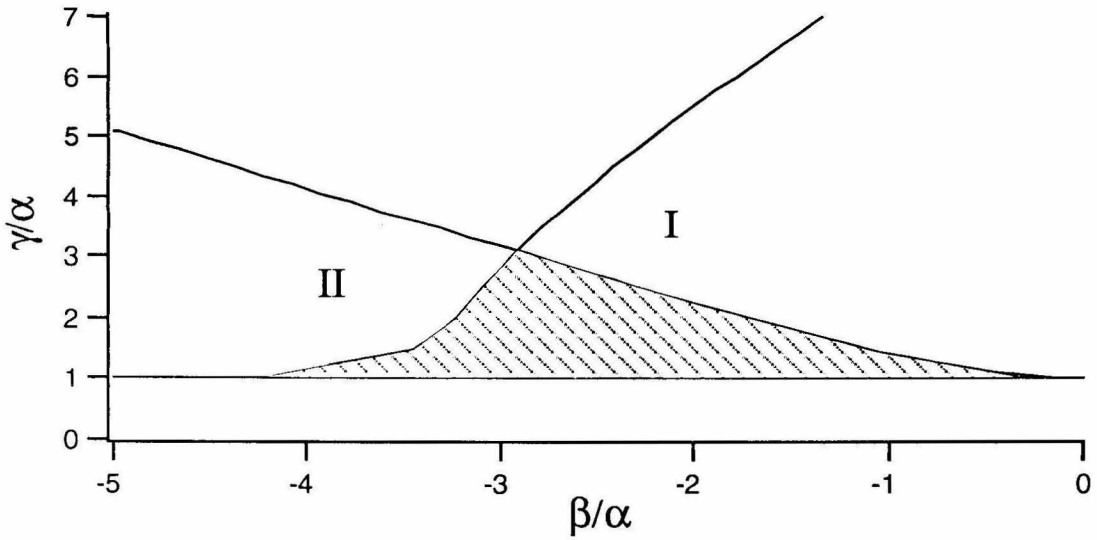


Figure 3.27: Region of the stability diagram in which the parameters lie when the soliton is stable.

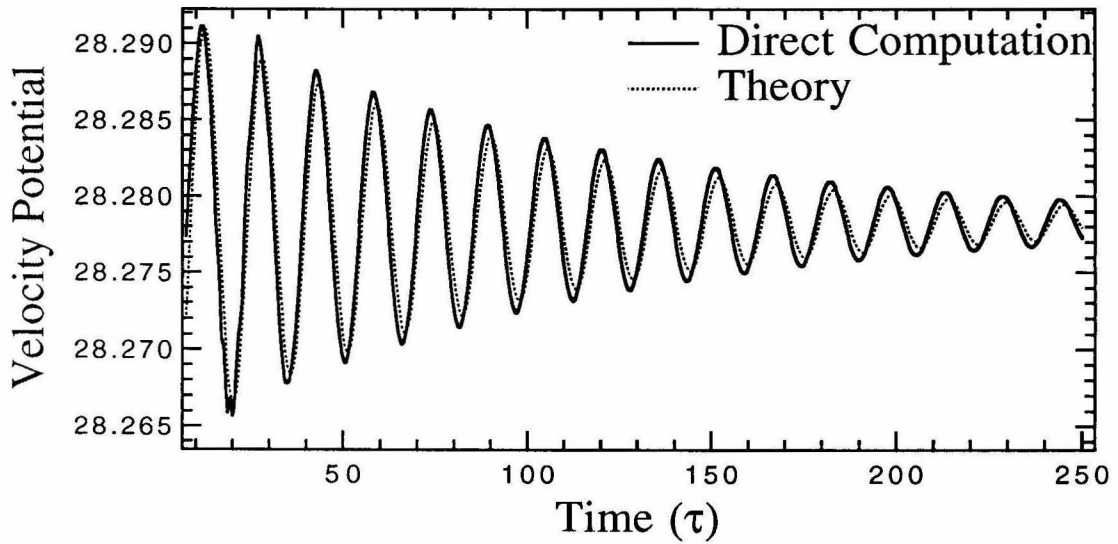


Figure 3.28: Evolution of a fixed point in time when the soliton is stable. The time and space evolution is shown in the preceding figures. For this plot,  $\beta = -0.29$ ,  $\gamma = 0.125$  and  $\alpha = 0.1$ .

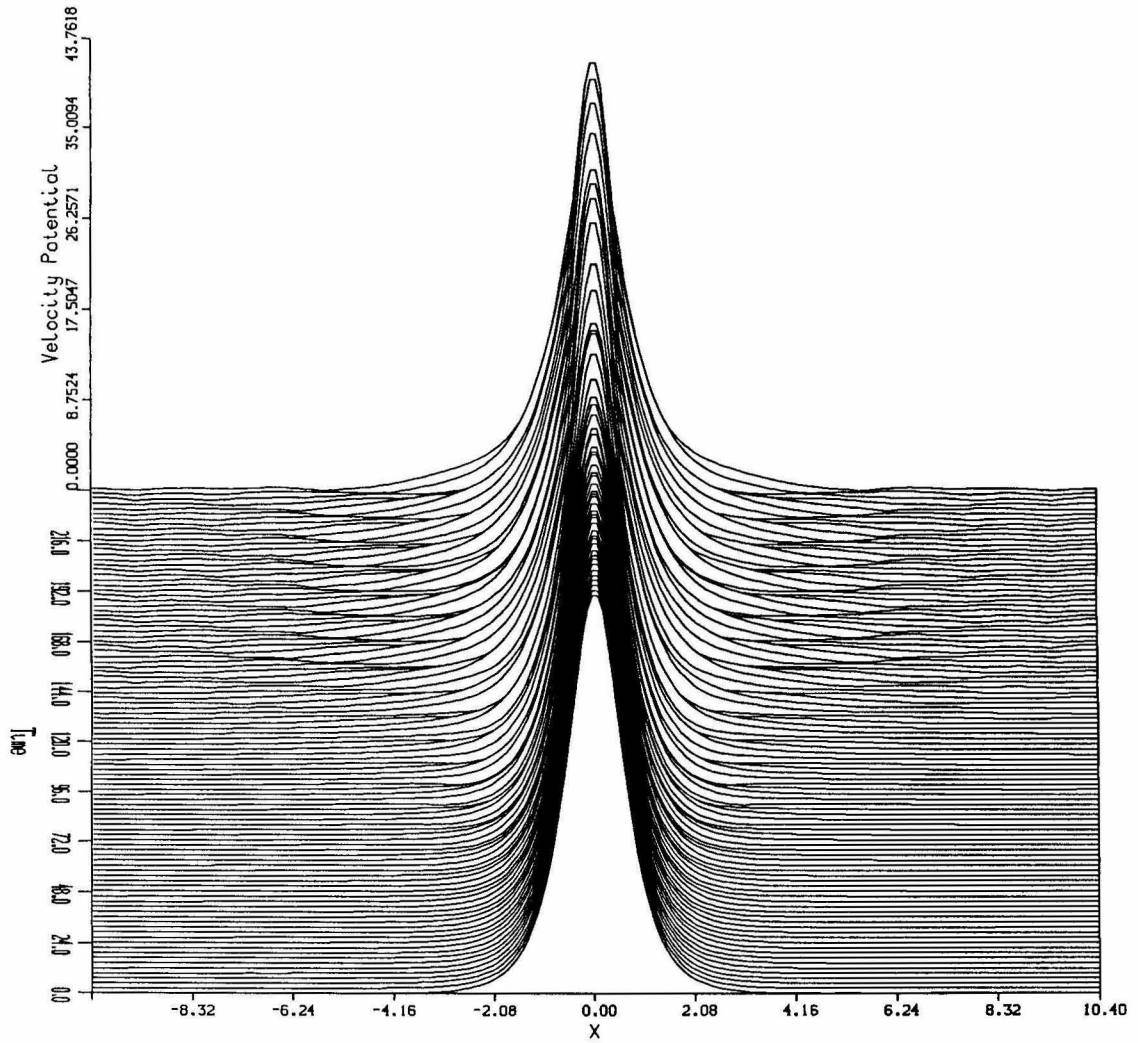


Figure 3.29: For values of the parameters making the solution weakly unstable to the discrete modes, nonlinear terms cap the linear growth and stabilize the stationary solution. For this plot,  $\beta = -0.58$ ,  $\gamma = 0.125$  and  $\alpha = 0.1$ .

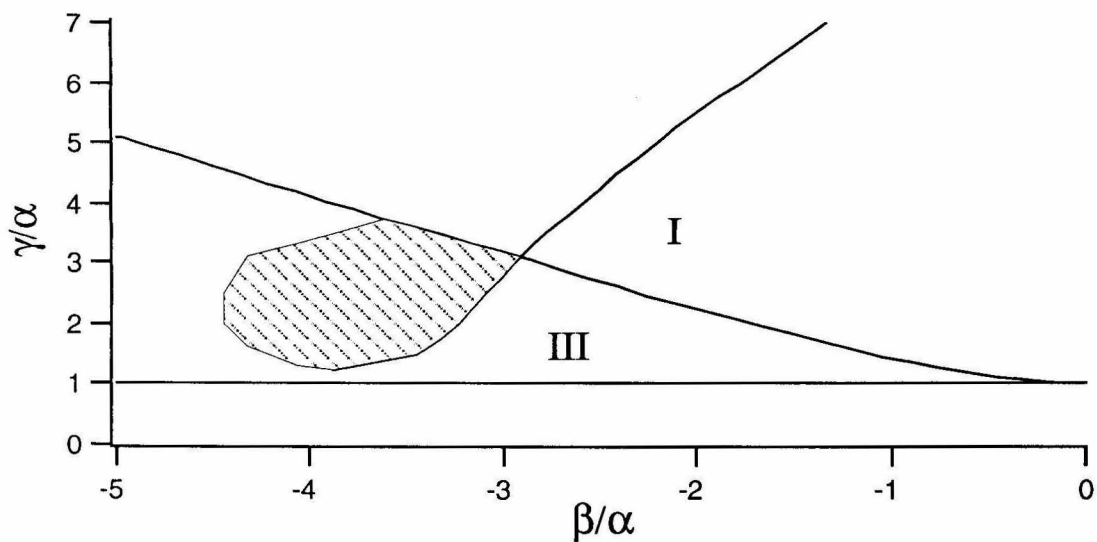


Figure 3.30: Region of the stability diagram in which the parameters lie when the soliton is bounded by a periodic solution.

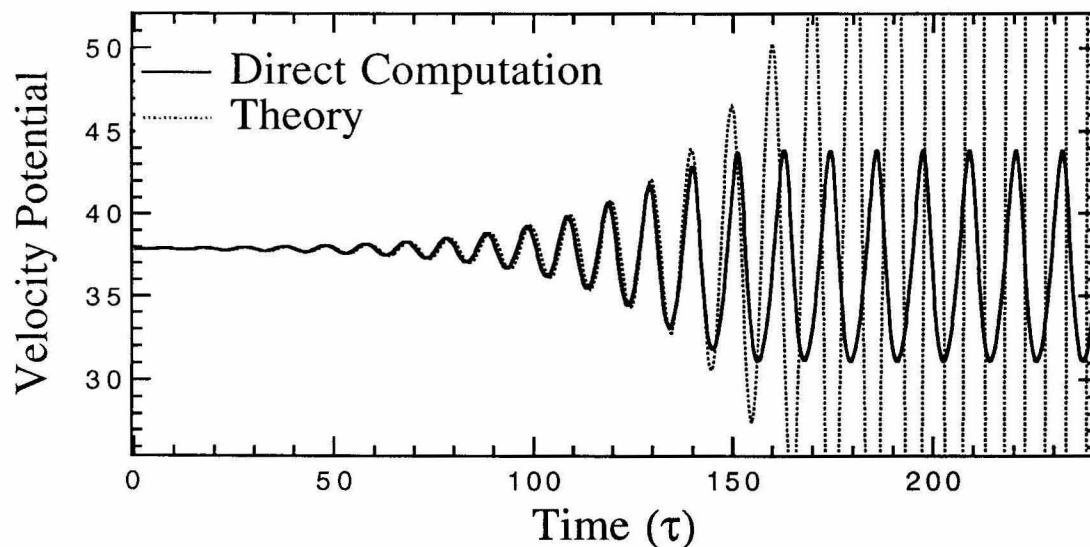


Figure 3.31: Evolution of a fixed point in time when the soliton goes to a slow-time, periodic solution. The time and space evolution is shown in the preceding figures. For this plot,  $\beta = -0.58$ ,  $\gamma = 0.125$  and  $\alpha = 0.1$ .

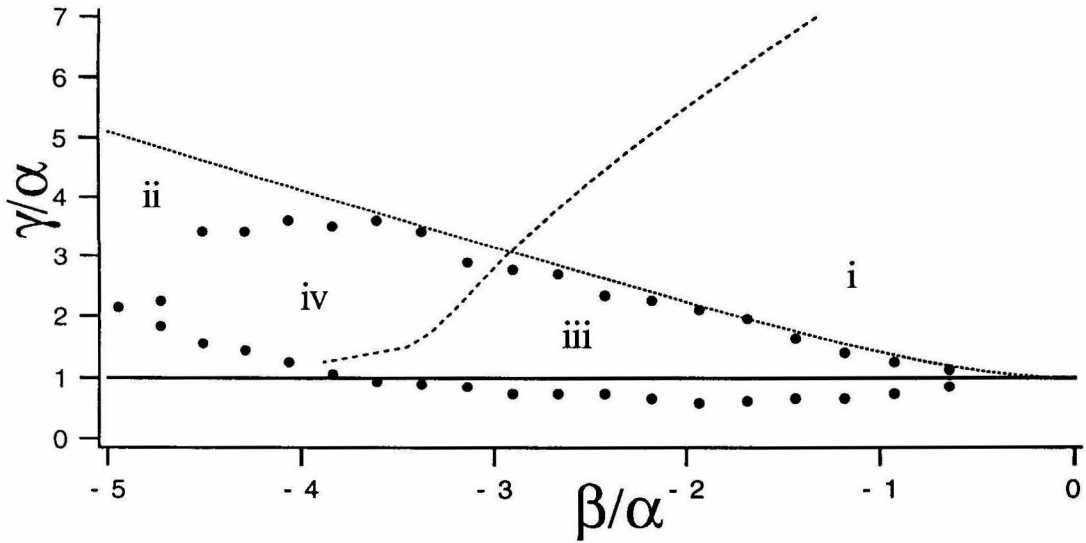


Figure 3.32: Experimental stability diagram for the standing solitary wave. The dots are the experimentally determined stability boundaries, and the lines are the linearized stability results. The width of the tank is 2.54 cm and the undisturbed water depth is 2.1 cm.

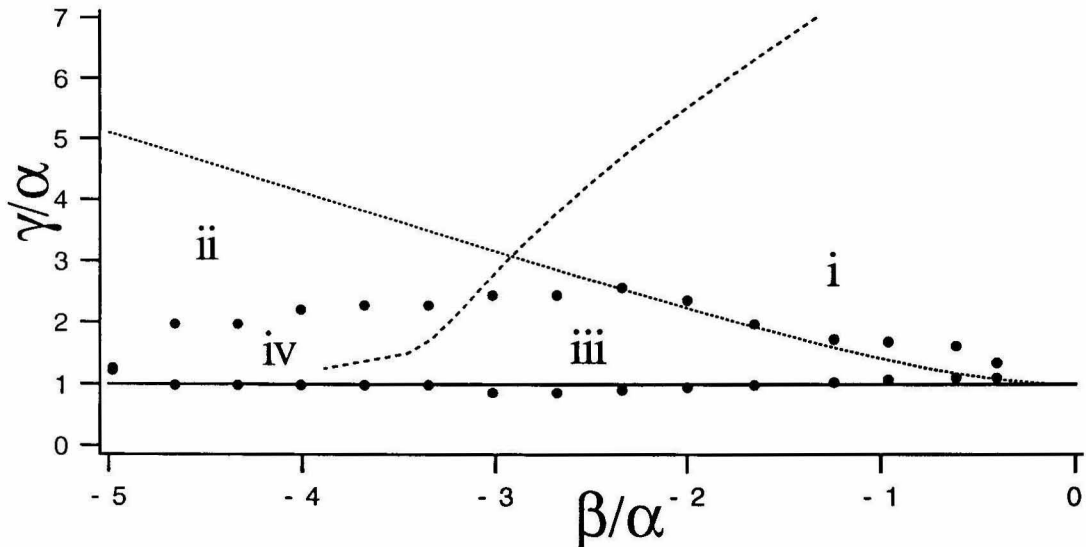


Figure 3.33: Experimental stability diagram for the standing solitary wave. The dots are the experimentally determined stability boundaries, and the lines are the linearized stability results. The width of the tank is 5 cm and the undisturbed water depth is 5.25 cm.

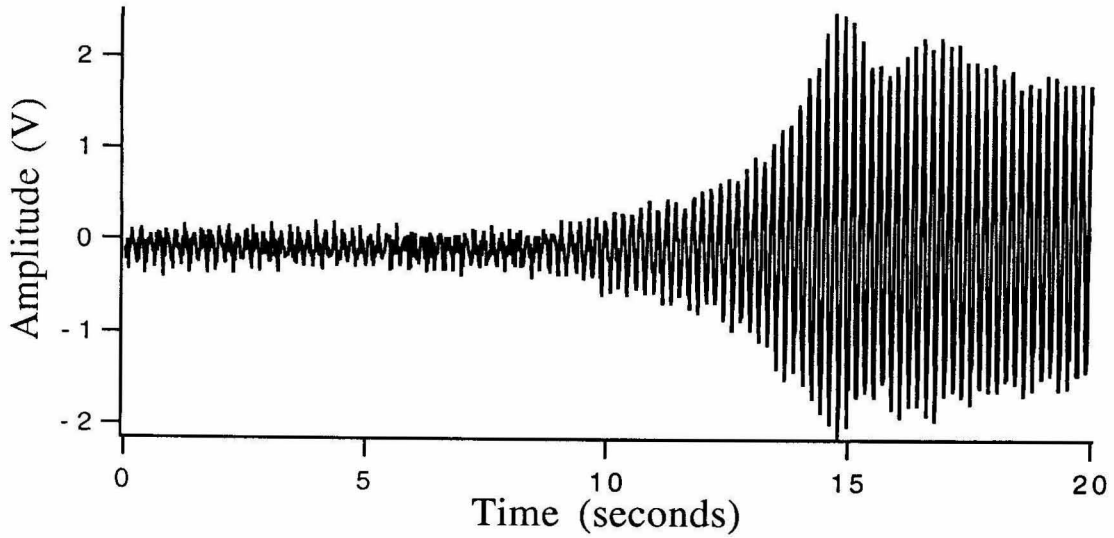


Figure 3.34: Wave gauge time trace for an unstable mode in the continuous spectrum. For this plot,  $\beta = -0.021$ ,  $\gamma = 0.055$  and  $\alpha = 0.032$ .

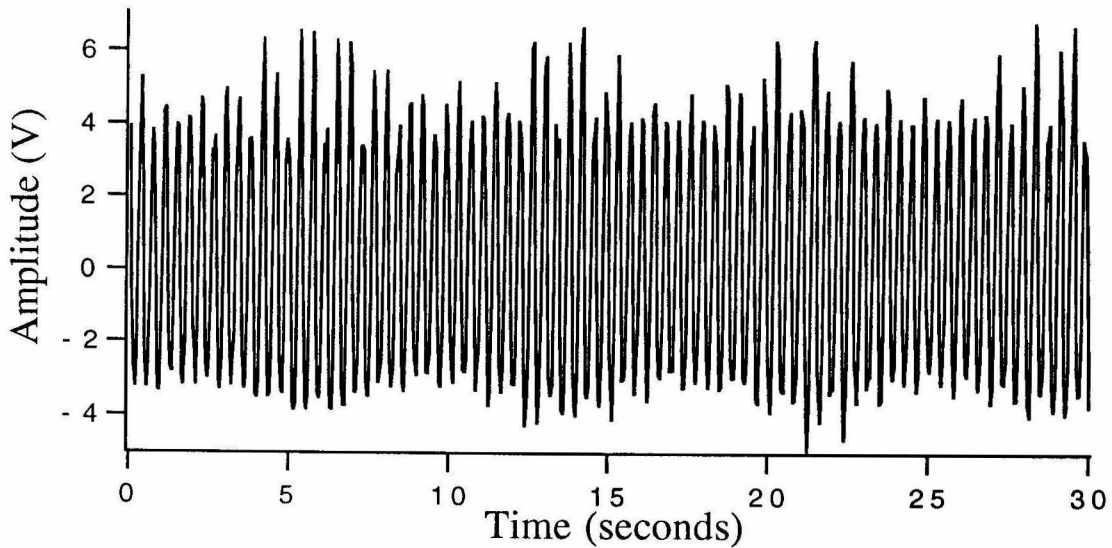


Figure 3.35: Wave gauge time trace of a solitary wave in the region unstable to linear, discrete modes but possessing periodic solutions. In this case,  $\beta = -0.046$ ,  $\gamma = 0.019$  and  $\alpha = 0.008$ .

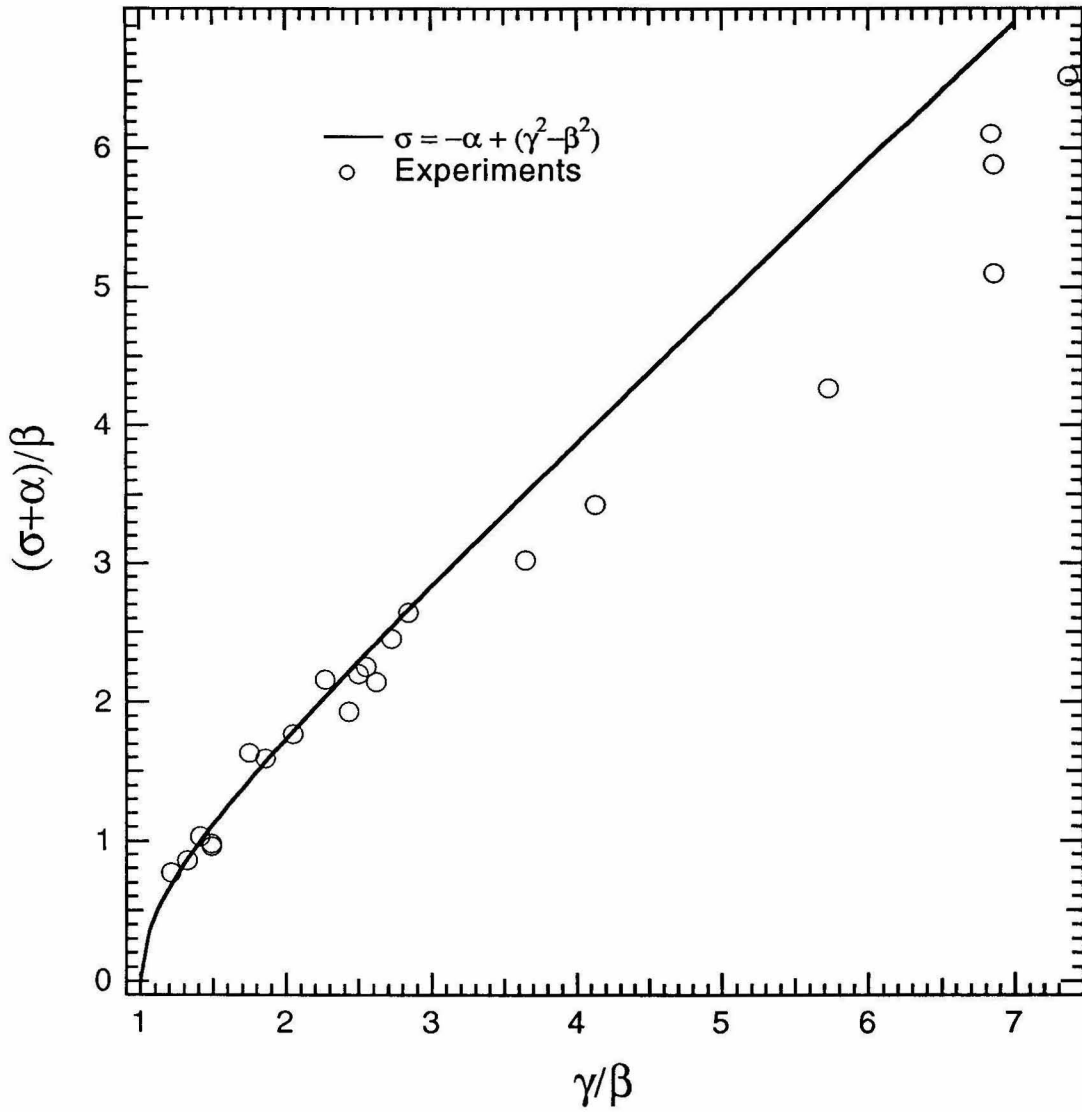


Figure 3.36: Comparison of continuous-spectrum growth rates. The line is the theoretical result, while the dots are the experimental results.

# Chapter 4

## Kink-Wave Stability

We now analyze the stability of the standing kink wave or hyperbolic-tangent solution of the governing NLS equation, Equation 2.9. As in the case of the hyperbolic-secant solution, we perturb the stationary solution and linearize the system. The continuous spectrum of the linear operator is identified, and we draw conclusions about the stability of the wave relative to the continuous spectrum. When bound-mode branches are investigated, some branches are found numerically. However, asymptotic solutions for the bound-mode branches, used in Chapter 3 to verify the numerical findings, could not be found for the kink wave. We improve upon the result of the linear-stability analysis by constructing a proof of Lyapunov stability for one of the two kink stationary solutions under the nonlinear dynamics of the NLS equation when dissipation is neglected. The stability behavior of the hyperbolic-tangent solutions is found to be simpler than that of the hyperbolic-secant solutions. Direct, numerical simulations of the NLS equation are performed and compared with the preceding theory, confirming all of the theoretical results. Lastly, the stability analysis is compared to experimental observations of the stability of hyperbolic-tangent solutions.

## 4.1 Kink-Wave Linear Stability

Now consider the stability of kink-wave, stationary solutions. Kink-wave solutions occur when  $A$  of Equation 2.9 is negative, and the stationary solutions are given by Relations 2.17, repeated as follows:

$$\begin{aligned}
 i\psi_\tau + i\alpha\psi + c^2\psi_{\xi\xi} + \beta\psi + \gamma\psi^* + A|\psi|^2\psi &= 0, \\
 \psi_0 &= ae^{i\theta} f(\kappa\xi), \\
 f(\kappa\xi) &= \tanh(\kappa\xi), \\
 \sin(2\theta) &= \frac{\alpha}{\gamma}, \\
 \cos(2\theta) &= \pm\sqrt{1 - \alpha^2/\gamma^2} \equiv \frac{\tilde{\gamma}}{\gamma}, \\
 \kappa^2 &= \frac{1}{2c^2}(\beta + \tilde{\gamma}) \text{ and} \\
 \alpha^2 &= \frac{1}{-A}(\beta + \tilde{\gamma}). \tag{4.1}
 \end{aligned}$$

As with the standing solitary wave, the number of possible standing kink-wave solutions depends upon the parameters,  $\alpha, \beta, \gamma$ . We have  $A < 0$  and  $\gamma > \alpha$  for the existence of any kink solutions. Plotting  $\kappa^2 c^2$  (or  $-A\alpha^2$ ) versus  $\gamma$  helps to visualize the solution branch, as shown in Figure 4.1. Where  $\beta$  is negative, no solutions exist for  $\gamma < \sqrt{\alpha^2 + \beta^2}$ , while one solution, corresponding to  $\tilde{\gamma} > 0$ , exists for  $\gamma > \sqrt{\alpha^2 + \beta^2}$ . When  $\beta = 0$ , one stationary kink solution exists for all  $\gamma > \alpha$ . Lastly, when  $\beta > 0$ , two solutions exist for  $\gamma < \sqrt{\alpha^2 + \beta^2}$ , while only one exists when  $\gamma$  is greater than  $\sqrt{\alpha^2 + \beta^2}$ .

We proceed to analyze stability of the kink wave by perturbing a solution of the NLS equation as follows. Take a solution of the NLS equation to be  $\psi(\xi, \tau) =$

$\psi_0(\xi) + e^{i\theta}\eta(\xi, \tau)$ , where  $\eta$  is assumed to be small. The linearized system is

$$i\eta_\tau + i\alpha\eta + c^2\eta_{\xi\xi} + \beta\eta + \gamma e^{-2i\theta}\eta^* + 2A|\psi_0(\xi)|^2\eta + A|\psi_0(\xi)|^2\eta^* = 0, \quad (4.2)$$

which is the same form as in Chapter 3 with  $\psi_0$  now a hyperbolic tangent and  $A < 0$ . Substituting Relations 4.1 into the above equation, taking  $\eta(\xi, \tau) = \bar{p}(\xi, \tau) + i\bar{q}(\xi, \tau)$  and scaling  $\xi$  by  $\kappa$  give the system

$$\begin{aligned} -\bar{q}_\tau - 2\alpha\bar{q} + \frac{1}{2}(\beta + \tilde{\gamma})\bar{p}_{\xi\xi} + (\beta + \tilde{\gamma})(1 - 3\tanh^2(\xi))\bar{p} &= 0, \\ \bar{p}_\tau + \frac{1}{2}(\beta + \tilde{\gamma})\bar{q}_{\xi\xi} + (\beta - \tilde{\gamma})\bar{q} - (\beta + \tilde{\gamma})\tanh^2(\xi)\bar{q} &= 0. \end{aligned}$$

Separating the time dependence as  $\bar{p} = Re[p(\xi)e^{\sigma\tau}]$  and  $\bar{q} = Re[q(\xi)e^{\sigma\tau}]$ , dividing through by  $(\beta + \tilde{\gamma})/2$  and using  $\text{sech}^2(\xi) + \tanh^2(\xi) = 1$  give the following simple form:

$$\begin{aligned} -\bar{\sigma}q - 2\bar{\alpha}q + p_{\xi\xi} - 4p + 6\text{sech}^2(\xi)p &= 0, \\ \bar{\sigma}p + q_{\xi\xi} - mp + 2\text{sech}^2(\xi)q &= 0, \end{aligned} \quad (4.3)$$

where

$$\bar{\sigma} = \frac{2\sigma}{\beta + \tilde{\gamma}}, \quad (4.4)$$

$$\bar{\alpha} = \frac{2\alpha}{\beta + \tilde{\gamma}} \quad \text{and} \quad (4.5)$$

$$m = \frac{4\tilde{\gamma}}{\beta + \tilde{\gamma}}. \quad (4.6)$$

The System 4.3 is fourth-order, nonself-adjoint and possesses regular singular points as  $\xi \rightarrow \pm\infty$ . We regard  $\sigma$  as an eigenvalue and seek eigenfunctions,  $(p, q)$ , that go to zero at infinity. If  $\sigma$  is an eigenvalue, so is  $\sigma^*$ . If  $\alpha = 0$ , an eigenvalue  $\sigma$  implies that  $-\sigma$  is also an eigenvalue.

In analyzing System 4.3, we proceed by introducing the transformation  $z = \tanh(\xi)$ , taking the points  $\xi \rightarrow \pm\infty$  to  $z = \pm 1$ , and examining the indices at the singular points. The procedure is the same as that used to analyze the linear system as described in Chapter 3, and is described in detail in Appendix C. The eigenfunctions are represented by Frobenius series about the regular singular points. For the series originating at  $z = -1$ , the series are

$$p(z) = (1+z)^r \sum_{n=0}^{\infty} a_n (1+z)^n, \quad q(z) = (1+z)^r \sum_{n=0}^{\infty} b_n (1+z)^n.$$

Now, by substituting the above expansions into System 4.3, solving for the index,  $r$ , and the coefficients,  $a_n$  and  $b_n$ , gives for the indices,

$$r = \pm \frac{1}{2\kappa c} \sqrt{\beta + 2\tilde{\gamma} \pm \sqrt{\beta^2 - 2\alpha\sigma - \sigma^2}}. \quad (4.7)$$

The four values of  $r$  given by the above are arranged in pairs. When all four indices possess nonzero real part, two indices lead to solutions that satisfy the boundary conditions (those with positive, real part) and two give rise to solutions that do not satisfy the boundary conditions (those with negative, real part). In this case we expect discrete-spectrum eigenvalues, as outlined in Chapter 3. If the indices possess a pair of purely imaginary indices, we expect a continuous spectrum of eigenvalues, a synthesis of which will satisfy the boundary conditions at the singular points. Appendix C describes the algorithm for constructing eigenvalues and eigenfunctions in detail.

### 4.1.1 Continuous Spectrum

We determine the range of eigenvalues leading to a continuous spectrum by finding the values of  $\sigma$  that make at least one pair of indices purely imaginary. From

Equation 4.7, a purely imaginary index requires

$$\beta + 2\tilde{\gamma} \pm \sqrt{\beta^2 - 2\alpha\sigma - \sigma^2}$$

to be real and negative. There are several eigenvalue regions that satisfy this condition with the sign of the first term,  $\beta + 2\tilde{\gamma}$ , distinguishing two cases. Let  $\sigma = \sigma_r + i\sigma_i$ .

First consider the  $\tilde{\gamma} < 0$  solution and take  $\beta > 0$ . If  $|\tilde{\gamma}| > \beta/2$  so that  $\beta + 2\tilde{\gamma} < 0$ ; then the following ranges of  $\sigma$  lead to at least one pair of imaginary indices:

$$\begin{aligned} \sigma_i &= 0, \\ -\alpha - \sqrt{\alpha^2 + \beta^2} < \sigma_r < -\alpha + \sqrt{\alpha^2 + \beta^2}, \end{aligned} \quad (4.8)$$

or

$$\begin{aligned} \sigma_r &= -\alpha \quad \text{and} \\ \sigma_i &\quad \text{takes on any value.} \end{aligned}$$

Where  $\sigma_r > 0$ , we have eigenfunctions that grow exponentially in the slow time implying instability. Equation 4.8 shows that when  $\beta + 2\tilde{\gamma} < 0$ , there are always eigenvalues in the range  $0 < \sigma_r < -\alpha + \sqrt{\alpha^2 + \beta^2}$  so that this case is always unstable.

Now let  $\beta + 2\tilde{\gamma} > 0$  and consider stationary kink solutions corresponding to both signs of  $\tilde{\gamma}$ . The following ranges of  $\sigma$  lead to one pair of purely imaginary indices corresponding to the negative sign of the inner square root in Equation 4.7:

$$\sigma_i = 0,$$

$$\begin{aligned}\sigma_r &< -\alpha + \sqrt{\alpha^2 - 4\tilde{\gamma}(\beta + \tilde{\gamma})}, \\ \sigma_r &> -\alpha - \sqrt{\alpha^2 - 4\tilde{\gamma}(\beta + \tilde{\gamma})},\end{aligned}\tag{4.9}$$

when  $4\tilde{\gamma}(\beta + \tilde{\gamma}) < \alpha^2$  and

$$\begin{aligned}\sigma_r &= -\alpha, \\ \sigma_i &> \sqrt{4\tilde{\gamma}(\beta + \tilde{\gamma}) - \alpha^2}, \\ \sigma_i &< -\sqrt{4\tilde{\gamma}(\beta + \tilde{\gamma}) - \alpha^2},\end{aligned}\tag{4.10}$$

when  $4\tilde{\gamma}(\beta + \tilde{\gamma}) > \alpha^2$ . The maximum growth rate is given by the first inequality of Equation 4.9,

$$\sigma_{rmax} = -\alpha + \sqrt{\alpha^2 - 4\tilde{\gamma}(\beta + \tilde{\gamma})}.\tag{4.11}$$

The condition for instability is  $\sigma_{rmax} > 0$ , implying

$$\tilde{\gamma}(\beta + \tilde{\gamma}) < 0.\tag{4.12}$$

However,  $\kappa^2 c^2 = (\beta + \tilde{\gamma})/2 > 0$ ; therefore,  $(\beta + \tilde{\gamma})$  is always positive wherever the stationary solutions exist. Therefore, the stationary solution having  $\tilde{\gamma} < 0$  satisfies Condition 4.12 for instability for all values of the parameters for which the solution exists and as a consequence, is always *unstable* to continuous modes. Conversely, the stationary solution having  $\tilde{\gamma} > 0$  never satisfies Condition 4.12 and is *stable* to continuous modes for all parameters for which the stationary solution exists. A summary of the stability properties of the continuous spectrum is shown in Table 4.1.

### 4.1.2 Discrete Spectrum

When both pairs of  $r$  possess nonzero real parts, we look for eigenfunctions in the discrete spectrum. The eigenvalues and eigenfunctions are computed using the

	$\tilde{\gamma} > 0$	$\tilde{\gamma} < 0$
$\beta > 0$	Always Stable	Always Unstable
$\beta < 0$	Always Stable	Does not exist

Table 4.1: Continuous-spectrum stability results.

same kind of scheme described in Chapter 3, with the series solutions computed from Equation 4.3. The series coefficients and the numerical scheme are given in Appendix C.

We look for eigenvalue branches for both the  $\tilde{\gamma}$  positive and the  $\tilde{\gamma}$  negative kink solutions. When considering the  $\tilde{\gamma} < 0$  stationary solution, only the trivial branch  $\sigma \equiv 0$  is found. Also, for the second stationary solution,  $\tilde{\gamma} > 0$ , with  $\beta < 0$ , no nonzero eigenvalue branch is found. Surprisingly, a bound-mode branch exists for the case  $\beta > 0$ ,  $\tilde{\gamma} > 0$  and is shown in Figure 4.2. The eigenvalue of this branch always possesses negative real part for nonzero dissipation,  $\alpha$ . We are unable to find a perturbation expansion in terms of analytic functions to verify the branch found numerically. However, by simulating the linear-evolution equation directly, Equation 4.3, we verify the matching code. The direct simulation uses a fourth-order, Runge-Kutta time-stepping scheme with central differences in space. When the eigenfunction computed by the matching scheme is introduced as an initial condition to the evolution code, the resulting eigenvalue can be extracted and compared with that predicted by the matching scheme. Figure 4.3 shows the result of such a computation. Figure 4.4, a plot of the centerline time evolution, shows excellent agreement between the predicted eigenvalue and that found using the evolution computation. In summary, the kink-wave, stationary solutions corresponding to  $\tilde{\gamma} > 0$  and  $\tilde{\gamma} < 0$  are found to be everywhere stable to discrete-

	$\tilde{\gamma} > 0$	$\tilde{\gamma} < 0$
$\beta > 0$	Always Stable	No Branches Found
$\beta < 0$	No Branches Found	Kink does not exist

Table 4.2: Discrete-spectrum stability results.

spectrum perturbations. A summary of the discrete-spectrum results is shown in Table 4.2.

### 4.1.3 The Linear-Stability Picture

The complete linear-stability picture for the standing kink wave is summarized as follows. For the stationary solution with  $\tilde{\gamma} < 0$ , the kink solution is always *unstable* to the continuous spectrum with a maximum growth rate as given by Equation 4.9 or Equation 4.8. For this solution, no bound branches are found. For the stationary solution with  $\tilde{\gamma} > 0$ , the solution is always *stable* to both the continuous modes and the discrete modes. The stability diagram for this stationary solution is shown in Figure 4.5. Notice that the solution is observable for both  $\beta > 0$  and  $\beta < 0$  in comparison with the hyperbolic-secant solution, which is observable only for  $\beta < 0$ . Also, the stability of the stationary solutions along the  $\sigma = 0$  line remains unknown, since the nonlinear terms, neglected in the linear analysis, will become important there. The linear theory predicts that the stable region of the  $\tilde{\gamma} > 0$  solution is unbounded in  $\gamma$  and  $\beta$ . However, when  $\beta$  and  $\gamma$  become relatively large, the assumption of weak forcing and weak detuning will become a poor approximation. Therefore, we expect that the kink wave will deviate from the linear theory for some large  $\beta$  and  $\gamma$  as a result of dynamics that has not been modeled in the NLS system.

## 4.2 Kink-Wave Nonlinear-Stability Property

The preceding linear-stability analysis shows that one stationary kink solution is stable to the continuous spectrum, while the other is unstable to the continuous spectrum. A complete stability conclusion for the  $\tilde{\gamma} > 0$  solution can be provided when the dissipation is taken to be zero. Here stability is meant in the Lyapunov sense, and the analysis follows the reasoning established by Benjamin (1972) regarding the stability of soliton solutions of the Korteweg-de Vries (KdV) equation. Benjamin introduced the idea of stability of the shape of the soliton and used two time-invariant, nonlinear functionals of solutions of the KdV equation to establish Lyapunov stability. Improvements in the method of the proof were made by Bona (1975). Stability of solitary-wave solutions to the unforced, undamped, nonlinear Schrödinger equation was shown by Zhidkov (1986), using a method similar to Benjamin's. Linear and nonlinear stability of solitary-wave solutions to the forced KdV (fKdV) equation were examined by Camassa & Wu (1991) and Holm, Marsden, Ratiu & Weinstein (1985) provide an overview of nonlinear-stability proofs in fluid and plasma problems.

In the present work, we apply similar ideas to the problem of nonlinear stability of kink-wave, stationary solutions of the parametrically forced, undamped NLS equation. Nonlinear stability is intended in the sense that there exists a metric  $d(\cdot, \cdot)$  in an appropriate functional space on which the parametrically forced NLS equation is defined, so that given any  $\epsilon > 0$ , there exists a  $\delta > 0$  such that  $d(\Psi, \Psi_o) < \delta$  at  $\tau = 0$  implies that  $d(\Psi, \Psi_o) < \epsilon$  for any  $\tau > 0$ , where  $\Psi$  and  $\Psi_o$  are solutions of the NLS equation.

In defining the metric,  $d(\cdot, \cdot)$ , we note that the parametrically forced NLS

equation is invariant to translations in  $\xi$ ,  $\xi = \tilde{\xi} + \xi_o$ . With this invariance in mind, we use the idea of stability of the shape of the solution used first in Benjamin's work. A translation of the stationary solution in  $\xi$  without a change in the form of the solution is considered stable within this definition. Define  $\|\eta\|_1 = \int_{-\infty}^{+\infty} |\eta|^2 + |\eta_\xi|^2 d\xi$ , the Sobolev norm. Then  $d(\cdot, \cdot)$  is defined to be

$$d(\Psi_1(\xi, \tau), \Psi_2(\xi, \tau)) = \inf_{\nu \in R} \|\Psi_1(\xi, \tau) - \Psi_2(\xi - \nu, \tau)\|_1. \quad (4.13)$$

The existence of the metric,  $d$ , and its continuity in time has been shown by Bona (1975). A similar definition of the metric is used by Zhidkov (1986).

Let  $\Psi(\xi, \tau)$  be a general solution of the forced NLS equation and  $\Psi_o(\xi)$  be the kink-wave, stationary solution. In the work that follows,  $\eta(\xi, \tau) = \Psi(\xi, \tau) - \Psi_o(\xi - \nu)$  is taken to be at  $\nu$  such that

$$\|\eta\|_1 = \inf_{\nu \in R} \|\Psi(\xi, \tau) - \Psi_o(\xi - \nu)\|_1. \quad (4.14)$$

We assume that  $\eta \rightarrow 0$  as  $\xi \rightarrow \pm\infty$  and that  $\|\eta\|_1$  exists. Note that  $\|\Psi_o\|_1$  is infinite. However, this does not pose a problem, since only differences of solutions,  $\eta$ , are used to demonstrate stability. In the following analysis, the  $\tau$  dependence of  $\eta$  and  $\Psi$  is dropped from the notation for convenience, since it does not play an active role.

We note that the undamped, parametrically forced NLS equation possesses two functionals that are invariant in time, as given by Noether's First Theorem. The two functionals arise from the invariance of the Lagrangian with respect to translations in time,  $\tau$ , and space,  $\xi$ . The time-invariant functionals are

$$H(\Psi) = - \int_{-\infty}^{+\infty} \left( \frac{\beta}{2} |\Psi|^2 + \frac{A}{4} |\Psi|^4 + \frac{\gamma}{4} (\Psi^2 - \Psi^{*2}) - \frac{c^2}{2} |\Psi_\xi|^2 \right) d\xi, \quad (4.15)$$

$$L(\Psi) = \frac{1}{2i} \int_{-\infty}^{+\infty} (\Psi \Psi_\xi^*) d\xi. \quad (4.16)$$

The energy integral, used as an invariant in Zhidkov's proof,

$$E(\Psi) = \int_{-\infty}^{+\infty} |\Psi|^2 d\xi,$$

is not invariant with time when  $\gamma \neq 0$ . Let a general solution of Equation 2.9 be denoted  $\Psi(\xi, \tau) = \eta(\xi, \tau) + \Psi_o(\xi)$ , where  $\eta(\xi, \tau)$  is taken at the location in  $\xi$  for which the difference between the solution and the stationary kink is a minimum. For the case under consideration,  $\tilde{\gamma} > 0$ ,  $\kappa^2 c^2 = (\beta + \gamma)/2$  and  $\Psi_o(\xi) = a \tanh(\kappa\xi)$ , where  $\Psi_o$  is purely real. We construct the total variations of the functionals about the stationary solution; namely,

$$\begin{aligned} \Delta H = H(\eta + \Psi_o) - H(\Psi_o) = \\ - \int_{-\infty}^{+\infty} \left[ \frac{\beta}{2} |\eta|^2 + \frac{A}{4} (\Psi_o^* \eta^{*2} + \Psi_o \eta^2 + 4 |\Psi_o|^2 |\eta|^2) + \frac{\gamma}{4} (\eta^2 + \eta^{*2}) - \kappa^2 c^2 |\eta_\xi|^2 \right] d\xi - \\ - \int_{-\infty}^{+\infty} \frac{A}{2} (\Psi_o^* |\eta|^2 \eta + \Psi_o |\eta|^2 \eta^*) d\xi - \int_{-\infty}^{+\infty} \frac{A}{4} |\eta|^4 d\xi, \end{aligned}$$

and

$$\Delta L = a\kappa \int_{-\infty}^{+\infty} \text{sech}^2(\kappa\xi) q d\xi + \int_{-\infty}^{+\infty} p_\xi q d\xi,$$

where  $\eta(\xi, \tau) = p(\xi, \tau) + iq(\xi, \tau)$ . For convenience, let  $\bar{\xi} = \kappa\xi$ . Now consider the functional

$$\begin{aligned} \Delta M &= \Delta H + \frac{\kappa^2 c^2}{a^2} (\Delta L)^2 & (4.17) \\ &= \kappa^2 c^2 \int_{-\infty}^{+\infty} \left[ (p_\xi)^2 + (4 - 6 \text{sech}^2(\xi)) p^2 \right] d\xi + \\ &+ \kappa^2 c^2 \int_{-\infty}^{+\infty} \left[ (q_\xi)^2 + (C - 2 \text{sech}^2(\xi)) q^2 \right] d\xi + \\ &+ a|A| \int_{-\infty}^{+\infty} \tanh(\xi) |\eta|^2 p d\xi + \frac{|A|}{4} \int_{-\infty}^{+\infty} |\eta|^4 d\xi + \\ &+ \frac{4}{3} \kappa^2 c^2 F_1^2 + \frac{4\kappa^2 c^2 F_1}{\sqrt{3}a} \int_{-\infty}^{+\infty} p_\xi q d\xi + \frac{\kappa^2 c^2}{a^2} \left( \int_{-\infty}^{+\infty} p_\xi q d\xi \right)^2, \end{aligned}$$

where  $F_1 = \frac{\sqrt{3}}{2} \int_{-\infty}^{+\infty} q \operatorname{sech}^2(\xi) d\xi$ ,  $C = \frac{4\gamma}{\beta+\gamma}$ , and the bar over  $\xi$  has been dropped.

Note that  $C > 0$ , since

$$\gamma > 0 \quad \text{and} \quad \beta + \gamma = 2\kappa^2 c^2 > 0.$$

$\Delta M$  is invariant in time since  $\Delta H$  and  $\Delta L$  are both invariant in time. The motivation for choosing this particular combination of  $\Delta H$  and  $\Delta L$  will become apparent later.

The method of the proof is to establish an upper bound on  $\Delta M$  that depends upon  $\|\eta\|_1$  and to bound a second function of  $\|\eta\|_1$  by  $\Delta M$ . Then, fixing a  $\delta$  at  $\tau = 0$  fixes  $\Delta M$  for all time since it is invariant. The form of the inequalities on  $\Delta M$  determines the relationship between  $\epsilon$  and  $\delta$ .

### 4.2.1 Upper Bound for $\Delta M$

An upper bound for  $\Delta M$  may be established as follows. First, consider the second-order terms

$$\begin{aligned} & \int_{-\infty}^{+\infty} [(p_\xi)^2 + (4 - 6\operatorname{sech}^2(\xi))p^2] d\xi + \int_{-\infty}^{+\infty} [(q_\xi)^2 + (C - 2\operatorname{sech}^2(\xi))q^2] d\xi \\ & \leq \int_{-\infty}^{+\infty} [(p_\xi)^2 + 4p^2] d\xi + \int_{-\infty}^{+\infty} [(q_\xi)^2 + Cq^2] d\xi \\ & \leq C_1 \|\eta\|_1^2, \end{aligned}$$

where  $C_1 = \max[4, C]$ . Next, we can bound the term

$$\begin{aligned} F_1 &= \frac{\sqrt{3}}{2} \int_{-\infty}^{+\infty} \operatorname{sech}^2(\xi) q d\xi \\ &\leq \frac{\sqrt{3}}{2} \int_{-\infty}^{+\infty} \operatorname{sech}^2(\xi) |q| d\xi \\ &\leq \frac{\sqrt{3}}{2} \int_{-\infty}^{+\infty} \operatorname{sech}^2(\xi) |\eta| d\xi \\ &\leq \frac{\sqrt{3}}{2} |\eta|_\infty \int_{-\infty}^{+\infty} \operatorname{sech}^2(\xi) d\xi \end{aligned}$$

$$\leq \frac{\sqrt{3}}{\sqrt{2}} \|\eta\|_1, \quad (4.18)$$

where  $|\cdot|_\infty$  is the supremum norm and the Sobolev inequality,  $|\eta|_\infty \leq \|\eta\|_1/\sqrt{2}$ , has been used in the last step. Continuing to reduce each term we take

$$\begin{aligned} \int_{-\infty}^{+\infty} pq_\xi \, d\xi &\leq \int_{-\infty}^{+\infty} \frac{1}{2}(p + q_\xi)^2 \, d\xi \\ &\leq \frac{1}{2} \int_{-\infty}^{+\infty} (p + q_\xi)^2 + (q + p_\xi)^2 \, d\xi \\ &\leq \frac{1}{2} \int_{-\infty}^{+\infty} p^2 + q^2 + p_\xi^2 + q_\xi^2 + \frac{1}{2} \frac{d}{d\xi} (p + q)^2 \, d\xi \\ &= \frac{1}{2} \|\eta\|_1^2. \end{aligned} \quad (4.19)$$

Also,

$$\begin{aligned} \int_{-\infty}^{+\infty} \tanh(\xi) p|\eta|^2 \, d\xi &\leq \int_{-\infty}^{+\infty} |p| |\eta|^2 \, d\xi \\ &\leq \int_{-\infty}^{+\infty} |\eta| |\eta|^2 \, d\xi \\ &\leq \frac{\|\eta\|_1}{\sqrt{2}} \|\eta\|^2 \\ &\leq \frac{\|\eta\|_1^3}{\sqrt{2}}. \end{aligned} \quad (4.20)$$

Finally, we can bound

$$\begin{aligned} \int_{-\infty}^{+\infty} |\eta|^4 \, d\xi &\leq \left( \int_{-\infty}^{+\infty} |\eta|^2 \, d\xi \right)^2 \\ &\leq \|\eta\|_1^4. \end{aligned} \quad (4.21)$$

Combining the above results gives an upper bound for  $\Delta M$ ; namely,

$$\Delta M \leq D_1 \|\eta\|_1^2 + D_2 \|\eta\|_1^3 + D_3 \|\eta\|_1^4, \quad (4.22)$$

where  $D_1 = \kappa^2 c^2 (\max[4, C] + 2)$ ,  $D_2 = \frac{a|A|}{\sqrt{2}} + \frac{\kappa^2 c^2 \sqrt{2}}{a}$  and  $D_3 = \frac{\kappa^2 c^2}{4a^2} + \frac{|A|}{4}$ . All the coefficients,  $D_i$ , are positive.

### 4.2.2 Lower Bound for $\Delta M$

We now proceed to construct the lower bound for our invariant. First, consider the implication of the translation condition given by Definition 4.13. As in Benjamin's work, the following alternative translation simplifies the analysis. The solution  $\Psi(\xi)$  is relocated to  $\Psi(\xi - \nu_o)$ , where  $\nu_o(\tau)$  is determined by

$$\int_{-\infty}^{+\infty} |\Psi(\xi - \nu_o) - \Psi_o(\xi)|^2 d\xi = \inf_{\nu \in R} \int_{-\infty}^{+\infty} |\Psi(\xi - \nu) - \Psi_o(\xi)|^2 d\xi.$$

However, since  $\Psi_o(\xi)$  is purely real, translations in  $\xi$  will not affect contributions to the integral from the imaginary part of the difference. Let  $\Psi(\xi) = r(\xi) + is(\xi)$  and recall the assumption that  $|\Psi(\xi) - \Psi_o(\xi)| \rightarrow 0$  as  $\xi \rightarrow \pm\infty$ . Then,

$$\int_{-\infty}^{+\infty} |\Psi(\xi - a) - \Psi_o(\xi)|^2 d\xi = \inf_{\nu \in R} \int_{-\infty}^{+\infty} (r(\xi - \nu) - \Psi_o(\xi))^2 d\xi + \int_{-\infty}^{+\infty} s(\xi, t)^2 d\xi.$$

Differentiation of the above integral with respect to  $\nu$  at  $\nu = a$  gives

$$\begin{aligned} 0 &= \int_{-\infty}^{+\infty} r'(\xi - a)(r(\xi - a) - \Psi_o(\xi)) d\xi, \\ &= - \int_{-\infty}^{+\infty} r'(\xi - a)\Psi_o(\xi) d\xi, \\ &= \int_{-\infty}^{+\infty} r(\xi - a)\Psi'_o(\xi) d\xi. \end{aligned}$$

Setting  $r(\xi - a) = p(\xi) + \Psi_o(\xi)$ , the above integral reduces to

$$\begin{aligned} \int_{-\infty}^{+\infty} \Psi'_o(\xi)p(\xi) d\xi &= 0, \quad \text{or} \\ \int_{-\infty}^{+\infty} \text{sech}^2(\xi)p d\xi &= 0, \end{aligned} \tag{4.23}$$

giving a condition imposed on  $p$  by the translation of the solution in  $\xi$ .

Following Benjamin, spectral theory is used to establish the second-order inequalities. Again we proceed term by term, starting with the second-order variations. The second-order integral involving  $p$  is

$$I_p = \kappa^2 c^2 \int_{-\infty}^{+\infty} (p_\xi)^2 + (4 - 6\text{sech}^2(\xi))p^2 d\xi.$$

We can provide a lower bound for  $I_p$  by considering the form

$$J = \int_{-\infty}^{+\infty} (p_\xi)^2 - 6\text{sech}^2(\xi)p^2 d\xi + \int_{-\infty}^{+\infty} p^2 d\xi. \quad (4.24)$$

Appeal is now made to spectral theory to evaluate the first integral. Consider the eigenvalue problem

$$\phi'' + (\lambda + 6\text{sech}^2(\xi))\phi = 0, \quad \phi(\pm\infty) \rightarrow 0,$$

where  $\lambda$  is real. Recalling some fundamental results for this case (the limit-point case), the set of eigenvalues  $\lambda$  consists of a finite number of discrete, negative values together with a continuous spectrum of values from 0 to  $\infty$ . In general, if  $p \in L_2(-\infty, \infty)$ , there exists a transform

$$G(\lambda) = \int_{-\infty}^{+\infty} \phi(\xi; \lambda)p(\xi) d\xi,$$

with an inversion in the form

$$p(\xi) = \int_{-\infty}^{+\infty} \phi(\xi; \lambda)G(\lambda)d\rho(\lambda),$$

where  $\rho(\lambda)$  is the so-called spectral function. For the above eigenvalue problem, there are two discrete eigenvalues,

$$\lambda_1 = -4, \quad \lambda_2 = -1,$$

with corresponding eigenfunctions

$$\phi_1(\xi) = \frac{\sqrt{3}}{2}\text{sech}^2(\xi), \quad \phi_2(\xi) = \frac{\sqrt{3}}{\sqrt{2}}\text{sech}(\xi)\tanh(\xi),$$

where the eigenfunctions have been chosen such that

$$\int_{-\infty}^{+\infty} \phi_{1,2}^2 d\xi = 1.$$

With  $p$  expressed in terms of the above spectrum, we can form the following equality,

$$\int_{-\infty}^{+\infty} [(p_\xi)^2 - 6\text{sech}^2(\xi)p^2] d\xi = -4G_1^2 - G_2^2 + \int_0^{+\infty} \lambda G^2 d\rho(\lambda),$$

where  $G_1$  and  $G_2$  are given by

$$\begin{aligned} G_1 &= \int_{-\infty}^{+\infty} \phi_1 p d\xi, \\ G_2 &= \int_{-\infty}^{+\infty} \phi_2 p d\xi. \end{aligned}$$

However, application of the translation condition, Equation 4.23, shows that  $G_1 = 0$ . Therefore, we can conclude that

$$\int_{-\infty}^{+\infty} [(p_\xi)^2 - 6\text{sech}^2(\xi)p^2] d\xi = -G_2^2 + \int_0^{+\infty} G^2 \lambda d\rho(\lambda) \geq - \int_{-\infty}^{+\infty} p^2 d\xi.$$

Returning to  $J$ , Equation 4.24, the above inequality shows that  $J \geq 0$ . Finally, decompose the original integral,  $I_p$ , as

$$\begin{aligned} I_p &= \frac{\kappa^2 c^2}{12} \int_{-\infty}^{+\infty} (p_\xi)^2 + 31p^2 d\xi + \frac{11\kappa^2 c^2}{12} J + \frac{\kappa^2 c^2}{2} \int_{-\infty}^{+\infty} p^2 (1 - \text{sech}^2(\xi)) d\xi \\ &\geq \frac{\kappa^2 c^2}{12} \|p\|_1^2, \end{aligned} \tag{4.25}$$

establishing the bound desired.

The second-order integrals involving  $q$  are now considered. They are given by

$$\begin{aligned} I_q &= \kappa^2 c^2 \int_{-\infty}^{+\infty} (q_\xi)^2 - 2\text{sech}^2(\xi)q^2 + Cq^2 d\xi + \frac{4}{3}\kappa^2 c^2 F_1^2, \quad \text{where} \\ F_1 &= \frac{\sqrt{3}}{2} \int_{-\infty}^{+\infty} \text{sech}^2(\xi)q d\xi. \end{aligned} \tag{4.26}$$

In order to establish lower bound for  $I_q$ , it is necessary to separate  $q$  into its odd and even parts,  $q(\xi) = f(\xi) + g(\xi)$ , where  $f(\xi)$  is even and  $g(\xi)$  is odd.

The contribution to the integral from the even part,  $f$ , may be written

$$I_{qf} = \frac{\kappa^2 c^2}{3} \int_{-\infty}^{+\infty} (f_\xi)^2 - 6 \operatorname{sech}^2(\xi) f^2 d\xi + \kappa^2 c^2 \int_{-\infty}^{+\infty} C f^2 d\xi + \frac{4}{3} \kappa^2 c^2 F_1^2 + \frac{2\kappa^2 c^2}{3} \int_{-\infty}^{+\infty} (f_\xi)^2 d\xi.$$

Notice that the first integral is the same as that used to analyze the second-order  $p$  contribution, with the additional restriction that we are considering only even functions. Therefore,

$$\int_{-\infty}^{+\infty} (f_\xi)^2 - 6 \operatorname{sech}^2(\xi) f^2 d\xi = -4F_1^2 + \int_0^{+\infty} \lambda F^2 d\rho(\lambda) \geq -4F_1^2.$$

Inserting this result into the expression for  $I_{qf}$  shows that

$$I_{qf} \geq \kappa^2 c^2 \int_{-\infty}^{+\infty} \frac{2}{3} (f_\xi)^2 + C f^2 d\xi \geq C_{01} \|f\|_1^2, \quad (4.27)$$

where  $C_{01} = \min[\frac{2}{3}, C]$ , which is in the form desired. The reason for constructing the peculiar combination of  $\Delta H$  and  $\Delta L$  in  $\Delta M$  can now be seen. In the combination specified, we can cancel out the  $F_1$  terms in the invariant and reduce the integral to the desired form.

The contribution to  $I_q$  from odd functions is determined as follows. Let  $\mu$  be a real number such that  $\mu \in [0, 1]$ . The odd function contribution may be written

$$\begin{aligned} I_{qg} &= \kappa^2 c^2 \int_{-\infty}^{+\infty} (g_\xi)^2 - 2 \operatorname{sech}^2(\xi) g^2 d\xi + \kappa^2 c^2 \int_{-\infty}^{+\infty} C g^2 d\xi \\ &= \kappa^2 c^2 (1 - \mu) \int_{-\infty}^{+\infty} (g_\xi)^2 - 2 \operatorname{sech}^2(\xi) g^2 d\xi + \mu \kappa^2 c^2 \int_{-\infty}^{+\infty} (g_\xi)^2 + \left(\frac{C}{\mu} - 2\right) g^2 d\xi \\ &\quad + \kappa^2 c^2 \int_{-\infty}^{+\infty} 2\mu(1 - \operatorname{sech}^2(\xi)) g^2 d\xi, \end{aligned}$$

for any  $\mu$  in the specified range. Now, appealing again to spectral theory, the integral

$$\int_{-\infty}^{+\infty} (g_\xi)^2 - 2 \operatorname{sech}^2(\xi) g^2 d\xi \geq 0,$$

since the spectrum of the underlying operator,  $K = d^2/d\xi^2 + (\lambda + 2\text{sech}^2(\xi))$ , has no bound eigenvalues with odd eigenfunctions. Recalling that  $C > 0$ , we can always choose  $\mu < C/2$ . Then

$$I_{qq} \geq \mu\kappa^2c^2 \int_{-\infty}^{+\infty} (g_\xi)^2 + \left(\frac{C}{\mu} - 2\right)g^2 d\xi \geq C_{02}\|g\|_1^2, \quad (4.28)$$

where  $C_{02} = \kappa^2c^2\min[\mu, C - 2\mu]$ . Now, combining the results for the odd and even parts of  $q$ , Equation 4.27 and Equation 4.28, give for the  $I_q$  term,

$$I_q \geq C_{03}\|q\|_1^2, \quad (4.29)$$

where  $C_{03} = \min [C_{01}, C_{02}]$ . Using the relation  $\|\eta\|_1^2 = \|p\|_1^2 + \|q\|_1^2$  and combining the results for the second-order variations,  $I_q$  and  $I_p$ , Equations 4.25 and 4.29, give the result

$$I_p + I_q \geq C_1\|\eta\|_1^2, \quad (4.30)$$

with  $C_1 = \min[C_{03}, \frac{\kappa^2c^2}{12}]$ .

We have derived the lower bound for the second-order term in  $\Delta M$ . Approximations to the higher-order terms follow easily, using results already derived. We have shown

$$\begin{aligned} \Delta M \geq & C_1\|\eta\|_1^2 \\ & + a|A| \int_{-\infty}^{+\infty} \tanh(\xi)|\eta|^2 p d\xi + \frac{|A|}{4} \int_{-\infty}^{+\infty} |\eta|^4 d\xi + \\ & + \frac{4\kappa^2c^2F_1}{\sqrt{3}a} \int_{-\infty}^{+\infty} p_\xi q d\xi + \frac{\kappa^2c^2}{a^2} \left( \int_{-\infty}^{+\infty} p_\xi q d\xi \right)^2. \end{aligned}$$

From Inequalities 4.18, 4.19, 4.20 and 4.21, we have the results

$$\begin{aligned} F_1 & \leq \sqrt{\frac{3}{2}}\|\eta\|_1^2, \\ \int_{-\infty}^{+\infty} p q_\xi d\xi & \leq \frac{1}{2}\|\eta\|_1^2, \end{aligned}$$

$$\int_{-\infty}^{+\infty} \tanh(\xi) p|\eta|^2 d\xi \leq \frac{1}{\sqrt{2}}\|\eta\|_1^3, \quad \text{and}$$

$$\int_{-\infty}^{+\infty} |\eta|^4 d\xi \leq \|\eta\|_1^4.$$

Therefore, we can conclude that

$$\begin{aligned} \Delta M &\geq C_1\|\eta\|_1^2 \\ &\quad - \frac{a|A|}{\sqrt{2}}\|\eta\|_1^3 - \frac{|A|}{4}\|\eta\|_1^4 \\ &\quad - \frac{\sqrt{2}\kappa^2c^2}{a}\|\eta\|_1^3 - \frac{\kappa^2c^2}{4a^2}\|\eta\|_1^4. \end{aligned}$$

The above expression may be written

$$\Delta M \geq C_1\|\eta\|_1^2 - C_2\|\eta\|_1^3 - C_3\|\eta\|_1^4, \quad (4.31)$$

where  $C_2 = \frac{a|A|}{\sqrt{2}} + \frac{\sqrt{2}\kappa^2c^2}{a}$  and  $C_3 = \frac{|A|}{4} + \frac{\kappa^2c^2}{4a^2}$ . Equation 4.31 represents the bound on  $\|\eta\|_1$  necessary for the proof of stability. Note that  $C_1, C_2$  and  $C_3$  are positive.

### 4.2.3 Proof of Stability

We are now able to establish stability. The previous sections have provided the Inequalities 4.31 and 4.22 repeated here,

$$\begin{aligned} \Delta M &\geq C_1\|\eta\|_1^2 - C_2\|\eta\|_1^3 - C_3\|\eta\|_1^4, \\ \Delta M &\leq D_1\|\eta\|_1^2 + D_2\|\eta\|_1^3 + D_3\|\eta\|_1^4. \end{aligned}$$

The proof proceeds as follows. Let  $\|\eta\|_1 < \delta$  at  $\tau = 0$ . Then  $\Delta M \leq \nu(\delta)$ , where  $\nu(\delta) = D_1\delta^2 + D_2\delta^3 + D_3\delta^4$ . Define the function  $F(\|\eta\|_1) = C_1\|\eta\|_1^2 - C_2\|\eta\|_1^3 - C_3\|\eta\|_1^4$ . A plot of  $F$  is shown in Figure 4.13. From the figure, it can be seen that  $F$  takes on a maximum positive value of  $F_{max}$  at  $\|\eta\|_{max}$ . Take  $\delta$  to be sufficiently

small such that at  $\tau = 0$ ,  $\nu(\delta) < F_{max}$ . Let  $\|\eta\|_\delta$  be the value of  $\|\eta\|_1$  such that  $F(\|\eta\|_\delta) = \nu(\delta)$ . Then the inequality

$$\Delta M \geq F(\|\eta\|_1),$$

assures that

$$\|\eta\|_1 \leq \|\eta\|_\delta \quad \text{for all } \tau > 0,$$

since  $\Delta M$  is independent of time. Hence we have established a  $\delta$  dependent bound for  $\|\eta\|_1$  for all  $\tau > 0$ . Finally, given an  $\epsilon > 0$ , we can determine a  $\delta > 0$ , such that  $\|\eta\|_\delta < \epsilon$ , thereby showing  $\|\eta\|_1 < \epsilon$  for all  $\tau > 0$  when  $\|\eta\|_1 < \delta$  at  $\tau = 0$ . Hence, we can conclude stability of the kink shape for the parametrically forced, nonlinear Schrödinger equation for the mode  $\tilde{\gamma} > 0$ .

If the above argument is applied to the second kink mode,  $\tilde{\gamma} < 0$ , it fails because  $C \rightarrow \frac{-4\gamma}{\beta-\gamma}$ , which is negative everywhere this kink exists. The bounds on  $\Delta M$  that were formed previously cannot be established, and the analysis fails to draw the conclusion of stability. Such a failure is expected, since the linear-stability analysis shows that this particular mode is unstable to continuous-spectrum eigenfunctions.

### 4.3 Kink-Wave Numerical Simulations

Numerical simulations of the nonlinear Schrödinger equation, Equation 2.9, are computed to verify the preceding analytical results. The codes used are the same as those described in Chapter 3. As before, the numerical simulations provide information about the evolution of the system after instabilities occur near stationary solutions, a property that cannot be found from the preceding analysis. There are only two stability conclusions for solutions starting near the kink-wave

solutions. Solutions near the  $\tilde{\gamma} > 0$  solution are expected to be stable, while those near the  $\tilde{\gamma} < 0$  solution are expected to be unstable. The simulations verify these conclusions.

The first case examines the stationary kink solution given by  $\tilde{\gamma} < 0$ . Figure 4.6 shows the evolution of the kink in this case, clearly showing the evolution of unstable modes. The instability is to the continuous spectrum of the linear operator and results in the spreading of energy away from the kink center. Remarkably, the long-time evolution of the NLS equation shows that after the onset of instability, the system tends towards the second stationary kink solution, the  $\tilde{\gamma} > 0$  solution, which is known to be stable everywhere it exists. The next figure, Figure 4.7, shows the evolution of the center point of the space as a function of time and compares the growth rate to the maximum growth rate predicted by Equation 4.11. The predicted growth rate is good for short times with nonlinear effects creating differences for longer times. The centerline time evolution shows the approach to the stationary kink solution. The evolution of the  $\tilde{\gamma} < 0$  kink into the  $\tilde{\gamma} > 0$  kink is typical for our simulations. The above instability cannot be observed in the laboratory, since the negative  $\tilde{\gamma}$  solution is nowhere stable.

The evolution of a solution near the stationary solution given by  $\tilde{\gamma} > 0$  with  $\beta > 0$  is shown in Figure 4.8. Notice that despite a relatively large initial perturbation, the solution quickly returns to the stationary solution. The evolution of a point along the centerline is shown as a function of time in Figure 4.9. Figure 4.10 shows the evolution of the perturbed solution when  $\tilde{\gamma} > 0$  and  $\beta < 0$ . Again, the solution is stable to perturbations, as predicted. In each case, the stability analysis predicts the stability behavior of the kink wave.

## 4.4 Kink-Wave Experiments

We observe the standing kink wave in the laboratory, using the experimental apparatus described in Chapter 3. With the undisturbed water depth such that  $kh < 1$ , the kink soliton is generated by an impulsive twist of the tank about a line directed vertically upward through the centroid of the tank's rectangular cross section. The kink is more difficult to observe than the standing soliton because the appropriate initial condition is difficult to obtain. Also, the shallowness of the water tends to amplify the effects of irregularities in the tank's walls and bottom, resulting in preferred locations for the kink transitions. Once established, the kink wave is stable.

Denardo, Wright, Larazza & Putterman (1990) provide an experimental-existence diagram for the kink wave. While no stability analysis is offered, they experimentally identify the regions of existence of the kink wave. A plot of their experimental results, rescaled in terms of  $\beta$  and  $\gamma$ , is shown in Figure 4.12. For small  $\beta$  and  $\gamma$ , the stability region is bounded only by the lines required for formal existence of the solution. This result is in agreement with the foregoing analysis, which shows that the  $\tilde{\gamma} > 0$  solution is always stable. Denardo et al. properly identified the formal existence lines in their work, but they did not perform a stability analysis.

For large positive  $\beta$  it is observed that the kink wave develops variations along the length of the tank on the order of the tank's width, eventually giving way to oscillations containing more than the primary mode. These oscillations can be attributed to the instability of higher modes in the tank that are described by Benjamin & Ursell's (1954) work and are beyond the scope of this single-mode

analysis. Furthermore, for large values of  $\gamma$ , the kink wave appears to become unstable spatially, running towards the tank's ends and eventually annihilating itself in the tank's corner and leading to the plane (0,1)-sloshing mode (observed by Denardo et al. and ourselves). No explanation has been given for this instability, since  $\gamma$  is clearly large enough to violate the assumption of smallness in this work.

## **Figures for Chapter 4**

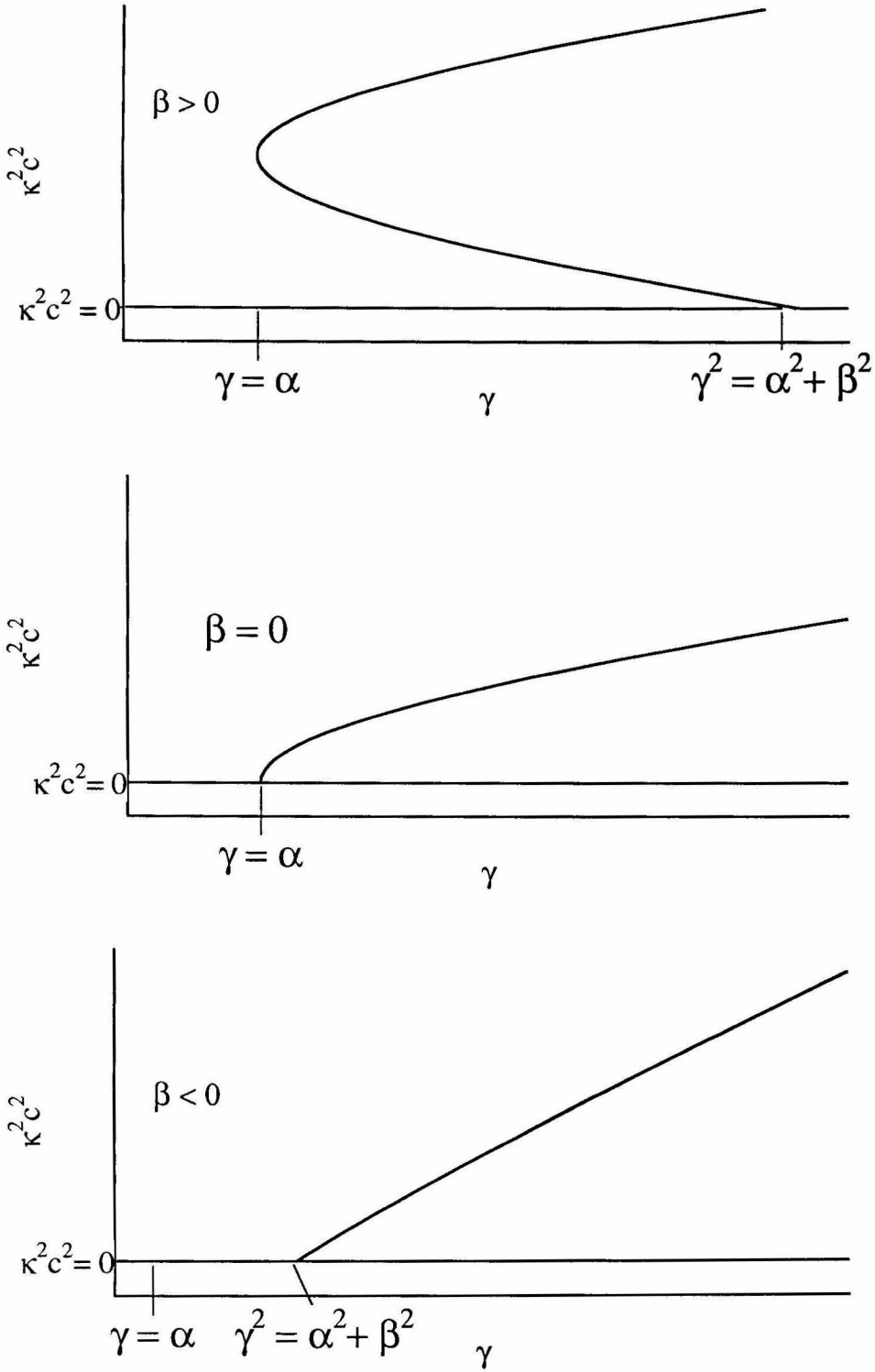


Figure 4.1: Branches for stationary, kink-wave solutions. *a* :  $\beta > 0$ , *b* :  $\beta = 0$ , *c* :  $\beta < 0$ .

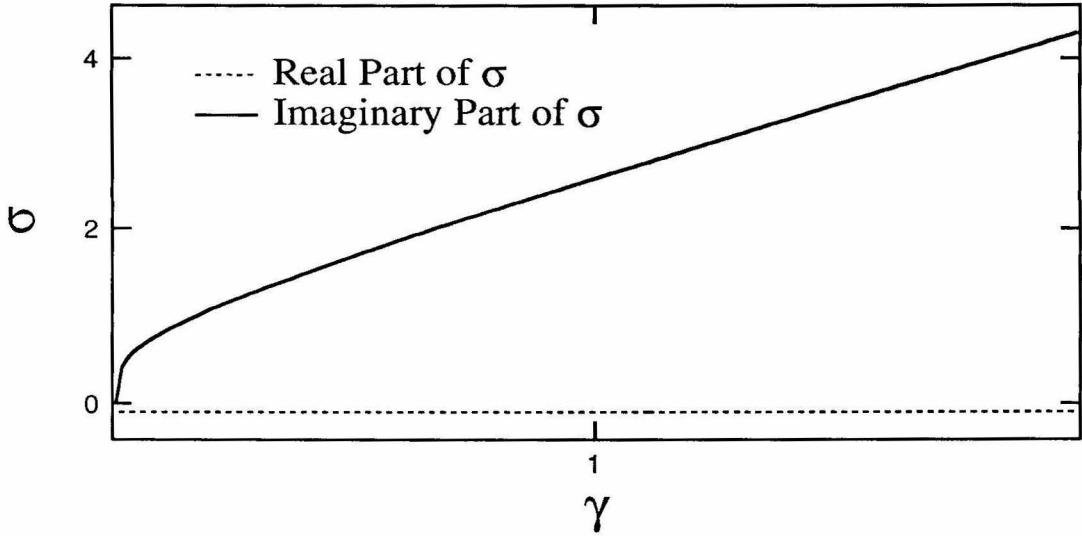


Figure 4.2: Bound-mode branch for the kink wave when  $\beta > 0$  and  $\tilde{\gamma} > 0$ . The case shown here has  $\beta = 1$  and  $\alpha = 0.1$ .

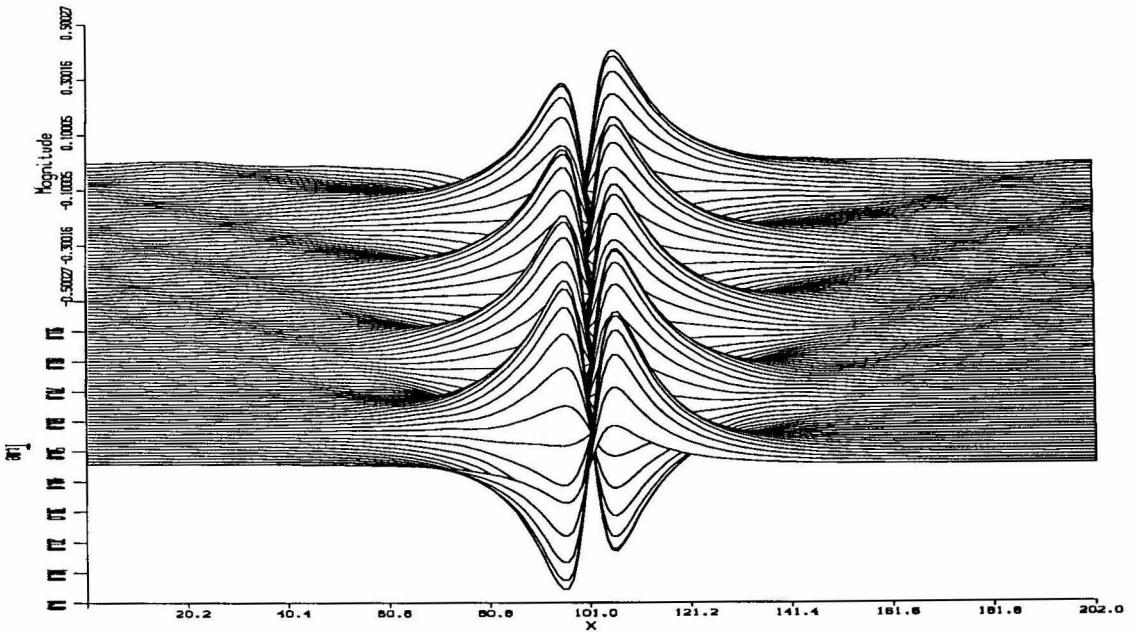


Figure 4.3: Evolution of the linear-stability equation in the bound-mode region. For this case,  $\beta = 1$ ,  $\gamma = 1.1$  and  $\alpha = 0.01$ .

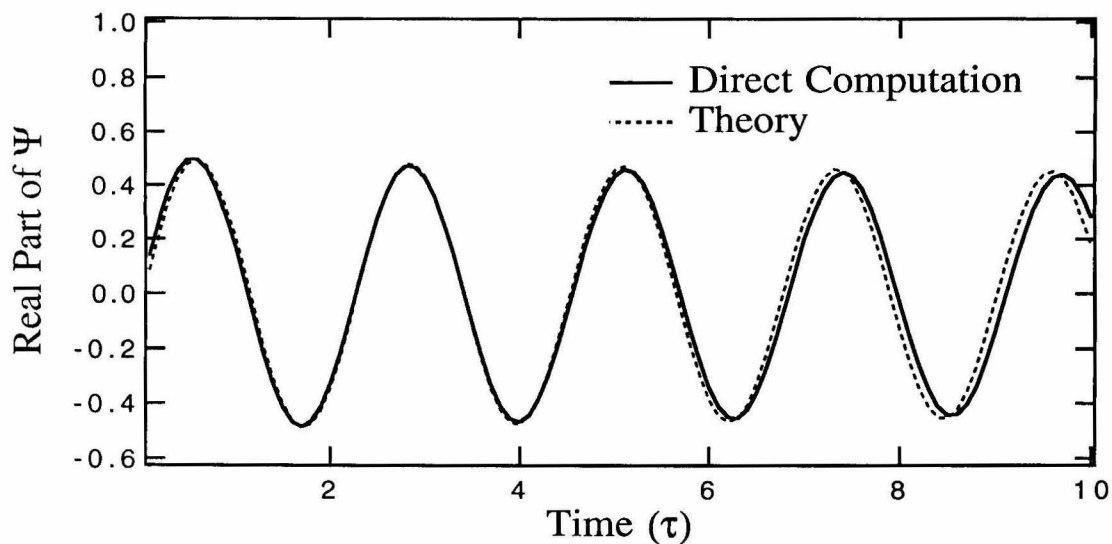


Figure 4.4: Evolution of the linear-stability equation in the bound-mode region. Comparison of the center line motion with that predicted by the matching code for  $\beta = 1$ ,  $\gamma = 1.1$  and  $\alpha = 0.01$ .

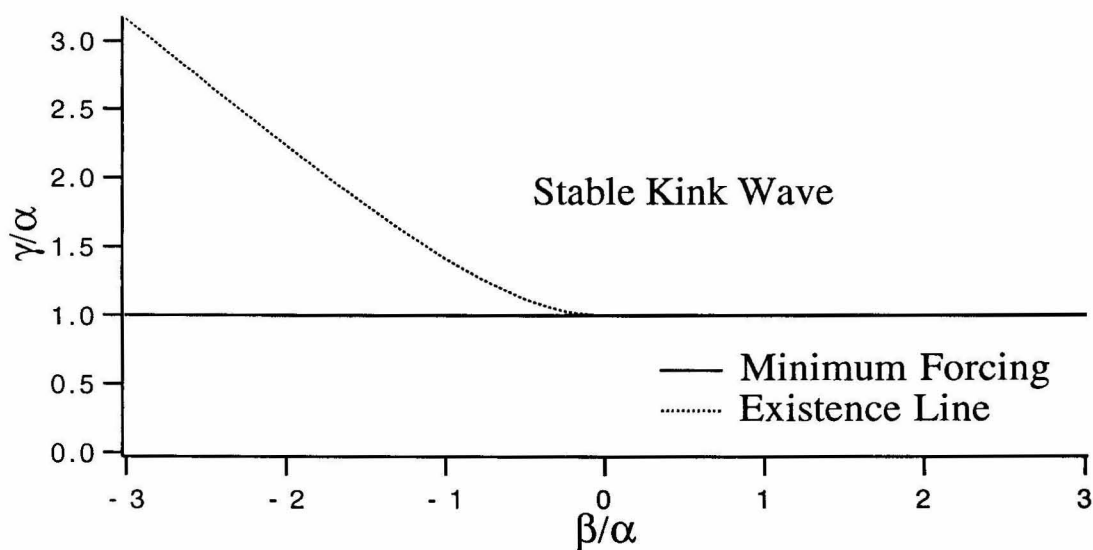


Figure 4.5: Linear-stability diagram for the  $\tilde{\gamma} > 0$  solution.

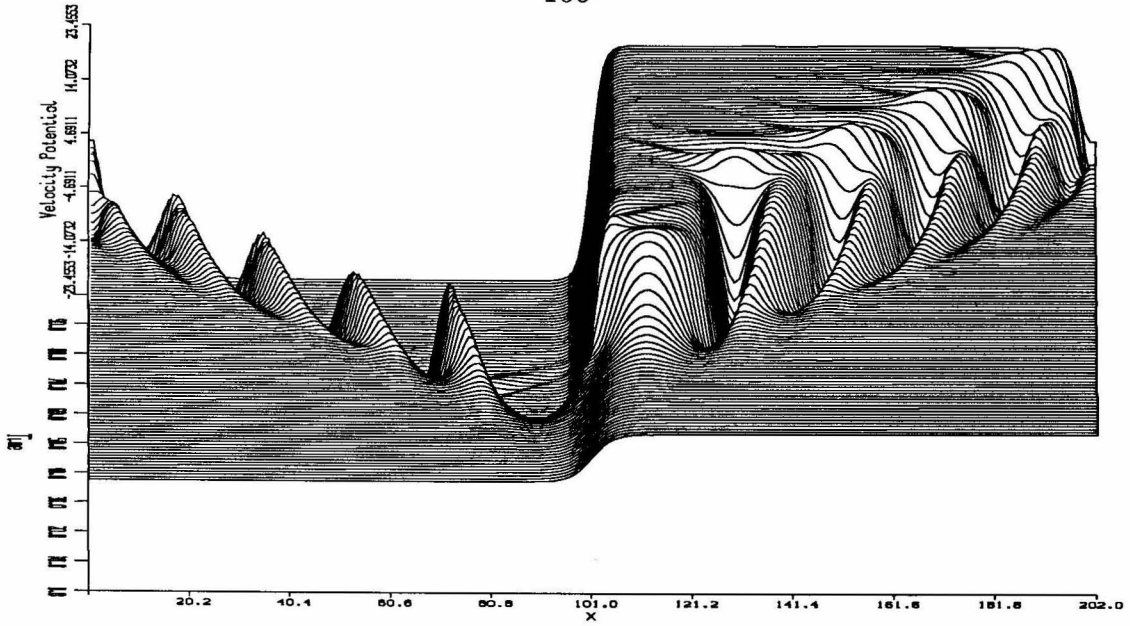


Figure 4.6: Evolution of the NLS equation for the kink solution having  $\tilde{\gamma} < 0$  for  $\beta = 1$ ,  $\gamma = 0.75$  and  $\alpha = 0.5$ .

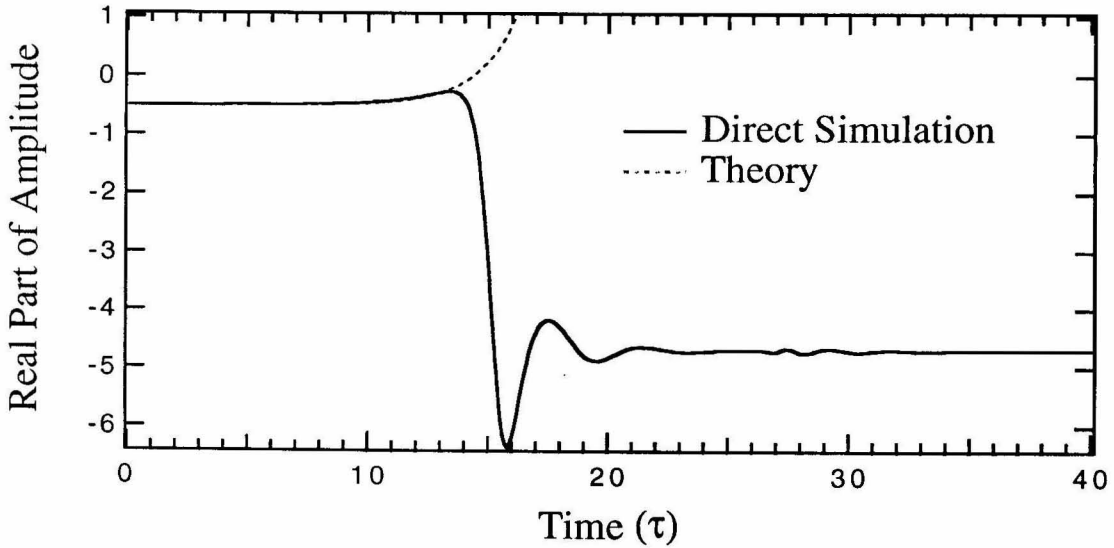


Figure 4.7: Evolution of the NLS equation for the kink solution with  $\tilde{\gamma} < 0$ . Comparison of the NLS growth rate of the solution on the center line with that predicted by the linear theory for  $\beta = 1$ ,  $\gamma = 0.75$  and  $\alpha = 0.5$ .

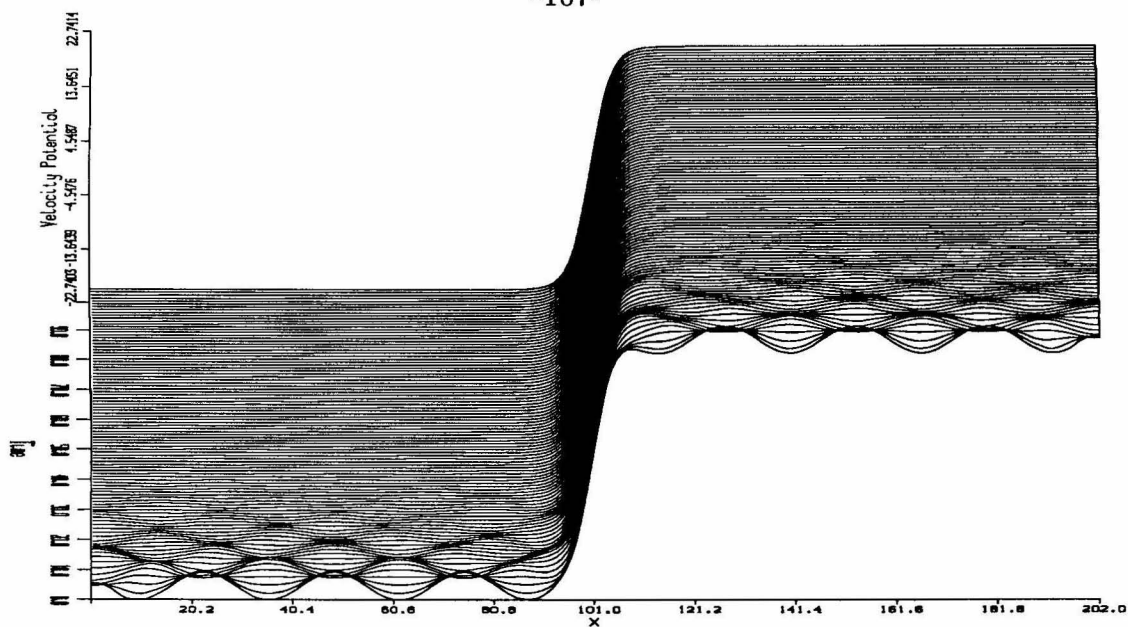


Figure 4.8: Evolution of the NLS equation for the kink solution given by  $\tilde{\gamma} > 0$ ,  $\beta > 0$ . For this figure,  $\beta = 1$ ,  $\gamma = 0.75$  and  $\alpha = 0.5$ .

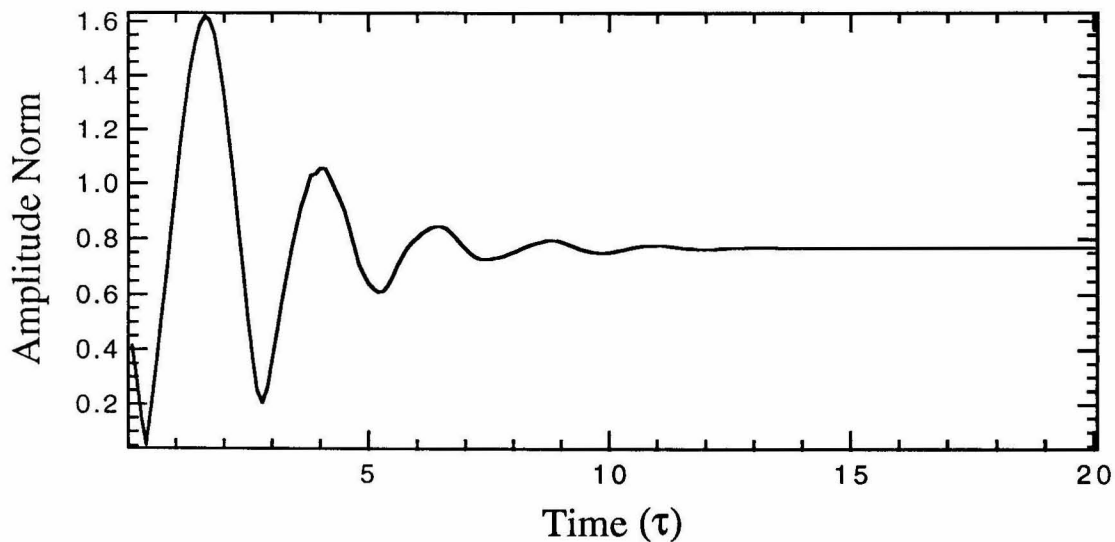


Figure 4.9: Evolution of the NLS equation for the kink solution given by  $\tilde{\gamma} > 0$ ,  $\beta > 0$ . Time evolution along the centerline when  $\beta = 1$ ,  $\gamma = 0.75$  and  $\alpha = 0.5$ .

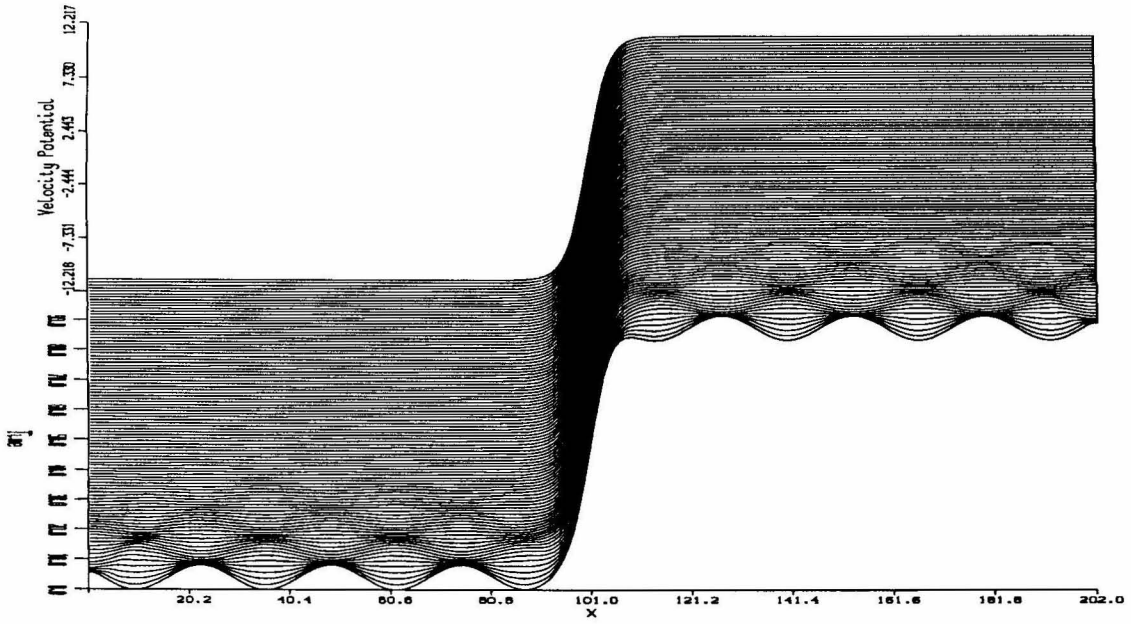


Figure 4.10: Evolution of the NLS equation for the kink solution given by  $\tilde{\gamma} > 0$ ,  $\beta < 0$ . In this figure,  $\beta = -1$ ,  $\gamma = 1.5$  and  $\alpha = 0.5$ .

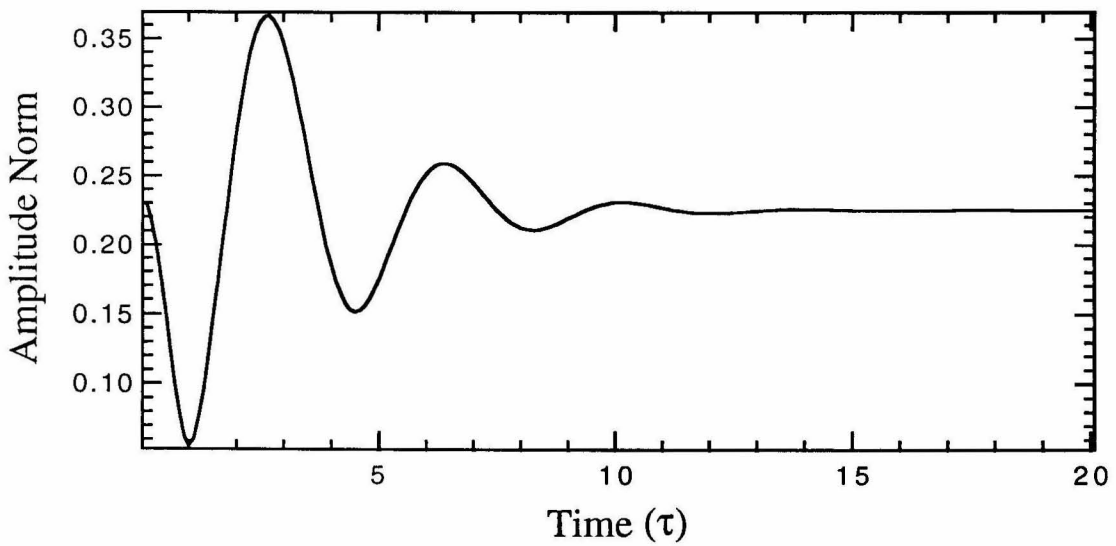


Figure 4.11: Evolution of the NLS equation for the kink solution given by  $\tilde{\gamma} > 0$ ,  $\beta < 0$ . Time evolution along the centerline for  $\beta = -1$ ,  $\gamma = 1.5$  and  $\alpha = 0.5$ .

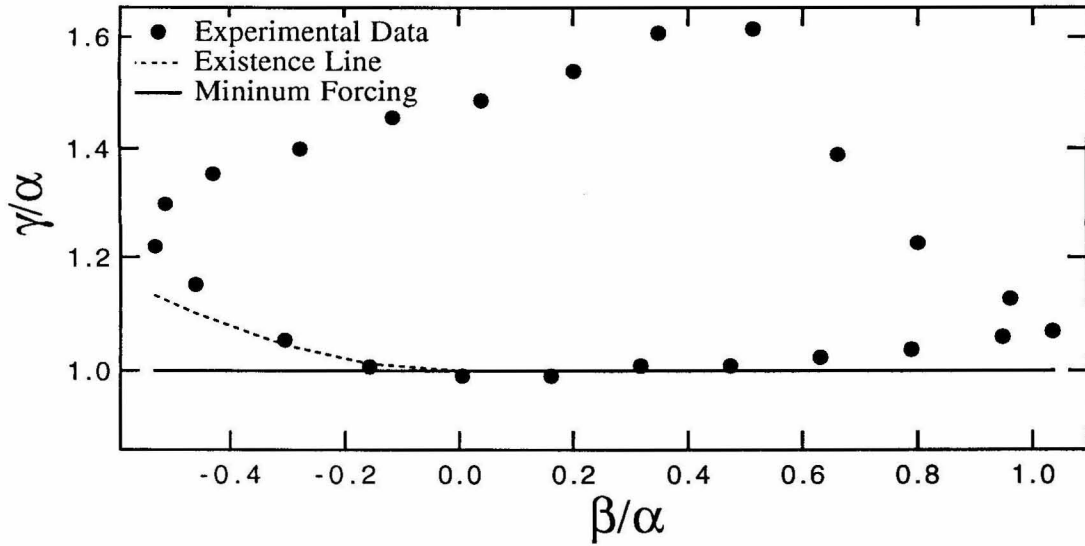


Figure 4.12: Experimental-stability diagram for the standing, kink wave from Denardo et al. (1990).

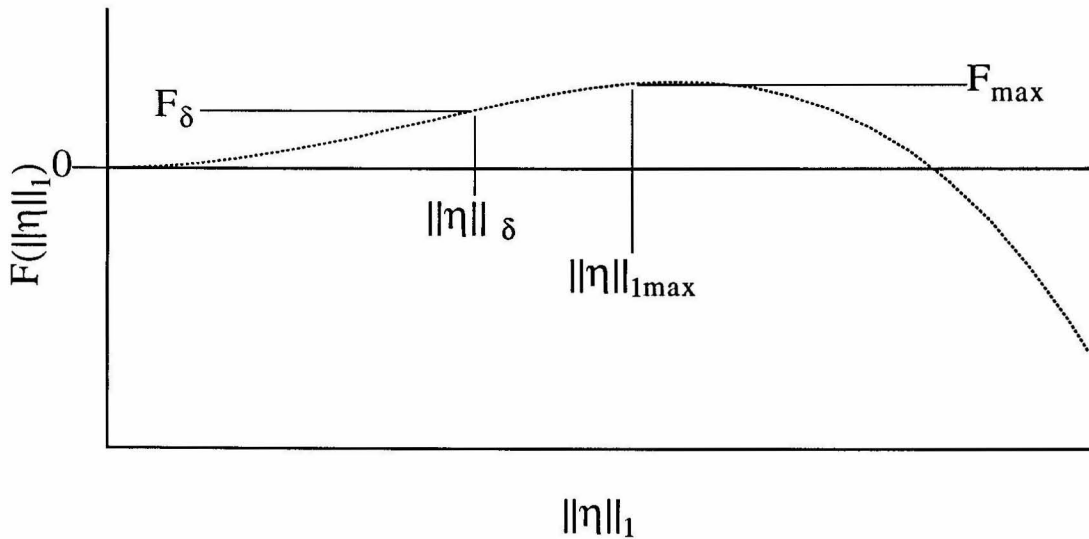


Figure 4.13: A plot of the lower-bound function,  $F$ , versus  $\|\eta\|_1$ . The maximum value,  $F_{max}$  occurs at  $\|\eta\|_{max}$ . The value  $\nu(\delta)$  is determined by the upper-bound condition, and bounds  $F$  at the value  $\|\eta\|_{\delta}$ .

# Chapter 5

## Conclusions

By using a small-amplitude approximation and an assumption of a single, primary sloshing mode, we derive the parametrically forced, nonlinear Schrödinger equation as the governing equation for the modulating envelope of a sloshing wave in Faraday resonance. Given fixed tank dimensions, the character of the stationary solutions of the envelope equation is seen to depend on the depth. Solitary waves exist as solutions to the NLS equation at all depths. The kink solitary wave exists for shallow depths, while the standing soliton exists for larger depths. Once the undisturbed water depth is fixed, the solitary-wave behavior depends upon three operating parameters,  $\gamma$ , the amplitude of parametric forcing,  $\beta$ , the frequency detuning between the forcing frequency and the first natural sloshing frequency, and  $\alpha$ , the dissipation. The properties of the solitary waves can be completely determined by the operating parameters. We also show that the NLS derivation may be generalized to the case of an internal free surface in a two-layer, stratified liquid and we find the modified equation for this case.

We examined the linear stability of the standing-soliton (hyperbolic-secant) solutions of the NLS equation. The result is that of the two possible stationary solutions, only the soliton present in the undamped, unforced case has a stable

region, the second stationary solution possessing unstable modes throughout the parameter space. For the soliton possessing a stable region, we find that the stable region exists only when the detuning is negative, so that one half of the forcing frequency must be below the first natural sloshing frequency. As the parameters  $\gamma$  and  $\beta$  are varied for fixed  $\alpha$ , different classes of instabilities arise. For relatively small detuning, an increase of the forcing amplitude causes the soliton to become unstable by creating neighboring disturbances, eventually developing into a cnoidal-wave solution. For relatively large detuning, the soliton becomes unstable to modes that focus the energy towards the soliton peak with a slowly oscillating component, eventually breaking the soliton and driving the system to a flat-surface solution. Lastly, for parameter values near the stable region but with slightly larger detuning, the soliton is unstable and gives way to a solution that is localized in space and periodic in the slow time. Numerical simulations of the NLS equation give an excellent, qualitative picture of the stability properties. The slow-time periodic solution, not found analytically, is easily observed by direct simulation. Also, the eigenvalues predicted by the analysis compared well with those computed in the direct simulations. All the qualitative features of the standing-soliton stability are observed experimentally, with good quantitative agreement for values of  $\epsilon \leq \frac{1}{2}$ .

The stability of the standing, kink-wave solution of the NLS equation was also investigated. The linear-stability analysis shows that only one of the two possible solutions is stable. Again, the stable solution is the one that exists for the unforced, undamped motion. The linear analysis predicts stability wherever the stable mode exists. For the stable kink wave, we have shown that the solution

is stable under the nonlinear dynamics of the NLS equation when dissipation is neglected. The nonlinear-stability argument also provides a bound on the possible initial conditions that will lead to the standing kink wave. Direct simulation of the NLS equation provided an excellent check for the stability properties of the kink wave and a basis for comparison of the eigenvalues found analytically. We observed that the unstable kink solution evolves into the stable solution. Experimental investigations of the kink wave show that for small  $\epsilon$ , the boundaries of the solution in parameter space are indeed the existence boundaries of the stable solution. When  $\epsilon$  increases, the kink becomes unstable to sources that are not modeled in this work.

In general, the parametrically forced, damped NLS equation adequately predicts the behavior of the envelope of the sloshing wave. When  $\epsilon$  is small, the NLS equation is in excellent quantitative and qualitative agreement with physical observations of the solitary waves. Even when  $\epsilon$  is large, the qualitative behavior of the waves is predicted by the NLS model. We find that strongly nonlinear effects such as wave breaking and droplet formation occur when  $\epsilon$  is near one and the NLS equation is inadequate, as expected. This study highlights some problems that warrant further research. First, the dynamics at the air, liquid and wall interface are not well understood and clearly play a role in the wave motion. A second, related problem concerns a better understanding of energy losses in the tank. This kind of Faraday wave system may be a good model system for future investigations of both of these effects.

## Appendix A

# Derivation of the Nonlinear Schrödinger Equation for a Stratified Fluid

In Chapter 2 we derive the equation of motion for the envelope of a single-mode sloshing wave on the free surface of a liquid contained in a high-aspect ratio rectangular tank that is forced in vertical, sinusoidal motion. In this appendix, we derive the evolution equation of a modulating envelope for sloshing motion on an internal surface between two immiscible liquids contained in a closed, rectangular tank of high-aspect ratio that is forced in vertical, sinusoidal motion. The motivation for such a derivation comes from the KdV equation, where Zhu (1986) shows that the fKdV equation, derived for waves on a homogeneous liquid, has an analogy for the internal layer of a two-layer liquid system. Here, we succeed in deriving a parametrically forced NLS equation for the modulating envelope in the two-layer case. The equation is similar to the one found in Chapter 2, Equation 2.8, with the coefficients modified for the internal-wave case.

The derivation proceeds in the same fashion as the derivation in the case of a homogeneous liquid. A rectangular tank of high-aspect ratio contains two immis-

cible liquids. The lighter liquid rests atop the heavier liquid, and the tank is closed on the top with a rigid lid. The two liquids completely fill the tank's volume. We assume that only one primary mode and its next higher harmonic are resonantly excited on the interface between the liquids, and that none of the natural frequencies of the secondary modes are nearly equal to the forcing frequency. Assume that no internal resonance occurs. Take a reference frame fixed to the rectangular tank with the  $x$ -axis directed along the long side of the tank of length,  $\ell$ , the  $y$ -axis across the tank of width  $b$ ,  $b \ll \ell$ . The wave number  $k$  of the standing cross wave generated by the vertical oscillation is  $\pi/b$ , and  $k\ell = O(1/\epsilon)$  is a measure of the aspect ratio of the tank. The  $z$ -axis points vertically upward such that  $z = 0$  at the quiescent, internal surface,  $z = -h_2$  at the tank bottom, and  $z = h_1$  at the tank lid. Figure A.1 shows a schematic of the above problem. Quantities in the upper, lighter liquid will be denoted with a subscript "1," while those in the lower liquid will have the subscript "2." The upper liquid has density  $\rho_1$ , and the lower liquid has density  $\rho_2$  such that  $\rho_2 > \rho_1$ . Both liquids are assumed inviscid and incompressible, and the motion is assumed to be irrotational and free of capillary effects. The velocity potentials are  $\phi_{1,2}(x, y, z, t)$ , and the internal surface displacement is  $\zeta(x, y, t)$ . The velocity potentials satisfy the Laplace equations

$$\begin{aligned}\nabla^2\phi_1 &= 0 \quad \text{for} \quad \zeta(x, y, t) < z < h_1 \quad \text{and} \\ \nabla^2\phi_2 &= 0 \quad \text{for} \quad -h_2 < z < \zeta(x, y, t).\end{aligned}$$

The wall conditions for the normal velocity are  $\mathbf{n} \cdot \nabla\phi_i = 0$  on the tank walls, top and bottom with  $i = 1, 2$ . The conditions on the internal interface are

$$\frac{p_1}{\rho_1} + \phi_{1t} + \frac{1}{2}(\nabla\phi_1)^2 + \tilde{g}(t)\zeta = 0, \tag{A.1}$$

$$\frac{p_2}{\rho_2} + \phi_{2t} + \frac{1}{2}(\nabla\phi_2)^2 + \tilde{g}(t)\zeta = 0, \quad (\text{A.2})$$

$$\zeta_t + \phi_{1x}\zeta_x + \phi_{1y}\zeta_y = \phi_{1z}, \quad (\text{A.3})$$

$$\zeta_t + \phi_{2x}\zeta_x + \phi_{2y}\zeta_y = \phi_{2z} \quad \text{and} \quad (\text{A.4})$$

$$p_1 = p_2 \quad (\text{A.5})$$

on  $z = \zeta(x, y, t)$ . The forced acceleration of the tank is absorbed in the gravity term so that  $\tilde{g}(t) = g(1 + 4\bar{\gamma} \cos(2\omega t))$ ,  $4\bar{\gamma}$  being the amplitude of the vertical oscillatory acceleration imposed on the tank and scaled with respect to the constant, gravitational acceleration,  $g$ . We assume that  $\phi_i = O(\epsilon)$  for  $i = 1, 2$  and  $\zeta = O(\epsilon)$  in the motion weakly forced with  $\bar{\gamma} = \epsilon^2\gamma$ ,  $\gamma$  being of  $O(1)$ , where  $\epsilon = a/h_2$  is the nonlinearity parameter for a typical wave amplitude  $a$ , with  $\epsilon \ll 1$ . Combining the two dynamic, boundary conditions, Equations A.1 and A.2, with the pressure condition on the interface, Equation A.5, leads to the equation

$$\phi_{2t} - \nu\phi_{1t} + \frac{1}{2} \left( (\nabla\phi_2)^2 - \nu(\nabla\phi_1)^2 \right) + (1 - \nu)\tilde{g}(t)\zeta = 0 \quad \text{on } z = \zeta, \quad (\text{A.6})$$

where  $\nu = \rho_1/\rho_2 < 1$ . As before, we expand the internal surface conditions on  $z = \zeta$  about  $z = 0$  in terms of  $\epsilon$  and eliminate  $\zeta$  in favor of  $\phi_1$  and  $\phi_2$ . In the stratified liquid case we obtain two equations, one from the combination of Equations A.3 and A.6, and the other from the combination of Equations A.4 and A.6. The first equation is given by

$$\begin{aligned} & \bar{\phi}_{tt} + \bar{g}\phi_{1z} - \frac{\bar{\phi}_t}{\bar{g}}(\bar{\phi}_{tt} + \bar{g}\phi_{1z})_z + \frac{1}{2}[(\nabla\phi_2)^2 - \nu(\nabla\phi_1)^2]_t + \\ & + \nabla\phi_1 \cdot \nabla\bar{\phi}_t + \frac{(\bar{\phi}_{tt} + \bar{g}\phi_{1z})_z}{2\bar{g}} \left[ \frac{1}{\bar{g}}(\bar{\phi}_t)_z^2 - (\nabla\phi_2)^2 + \nu(\nabla\phi_1)^2 \right] + \\ & + \left( \frac{\bar{\phi}_t}{2\bar{g}} \right) (\bar{\phi}_{tt} + \bar{g}\phi_{1z})_{zz} + \frac{1}{2}\nabla\phi_1 \cdot \nabla[(\nabla\phi_2)^2 - \nu(\nabla\phi_1)^2] - \\ & - \frac{\bar{\phi}_t}{\bar{g}} \left( [(\nabla\phi_2)^2 - \nu(\nabla\phi_1)^2]_{tz} + [\nabla\phi_1 \cdot \nabla\bar{\phi}_t]_z \right) + \end{aligned}$$

$$+\epsilon^2 4\gamma\bar{g} \cos(2\omega t)\phi_{1z} + \epsilon^2 8\omega\gamma \sin(2\omega t)\bar{\phi}_t = O(\epsilon^4) \quad \text{with}$$

$$\bar{\phi} = \phi_2 - \nu\phi_1 \quad \text{and}$$

$$\bar{g} = (1 - \nu)g \tag{A.7}$$

on  $z = 0$ . The second equation on  $z = 0$  is similar and is given by

$$\begin{aligned} & \bar{\phi}_{tt} + \bar{g}\phi_{2z} - \frac{\bar{\phi}_t}{\bar{g}}(\bar{\phi}_{tt} + \bar{g}\phi_{2z})_z + \frac{1}{2}[(\nabla\phi_2)^2 - \nu(\nabla\phi_1)^2]_t + \\ & + \nabla\phi_2 \cdot \nabla\bar{\phi}_t + \frac{(\bar{\phi}_{tt} + \bar{g}\phi_{2z})_z}{2\bar{g}} \left[ \frac{1}{\bar{g}}(\bar{\phi}_t)_z^2 - (\nabla\phi_2)^2 + \nu(\nabla\phi_1)^2 \right] + \\ & + \left( \frac{\bar{\phi}_t}{2\bar{g}} \right) (\bar{\phi}_{tt} + \bar{g}\phi_{2z})_{zz} + \frac{1}{2}\nabla\phi_2 \cdot \nabla[(\nabla\phi_2)^2 - \nu(\nabla\phi_1)^2] - \\ & - \frac{\bar{\phi}_t}{\bar{g}} \left( [(\nabla\phi_2)^2 - \nu(\nabla\phi_1)^2]_{tz} + [\nabla\phi_2 \cdot \nabla\bar{\phi}_t]_z \right) + \\ & + \epsilon^2 4\gamma\bar{g} \cos(2\omega t)\phi_{2z} + \epsilon^2 8\omega\gamma \sin(2\omega t)\bar{\phi}_t = O(\epsilon^4). \end{aligned} \tag{A.8}$$

In these equations, use has been made of the expansion of  $\zeta$  up to  $O(\epsilon^3)$ ,

$$\begin{aligned} g(1 - \nu)\zeta = & -(\phi_{2t} - \nu\phi_{1t}) + \frac{1}{g(1-\nu)}(\phi_{2tz} - \nu\phi_{1tz})(\phi_{2t} - \nu\phi_{1t}) - \\ & \frac{1}{2}[(\nabla\phi_2)^2 - \nu(\nabla\phi_1)^2] + O(\epsilon^3) \end{aligned} \tag{A.9}$$

on  $z = 0$ . The effects of weak-forcing excitation appear in the third-order terms of A.7, A.8 and A.9; however, they are needed only in Equations A.7 and A.8.

As in the homogeneous liquid case, we look for solutions of the above equations representing motions that slosh across the tank like  $\cos(ky)$  with frequency  $\omega$  very nearly equal to the primary, natural frequency  $\omega_0$  and that are modulated along the  $x$ -direction by an envelope depending on a slow time,  $\tau$ , and a long space,  $\xi$ . The appropriate scales of these variables are  $\tilde{t} = \omega t$  for the fast time,  $\tau = \epsilon^2 \omega t$  for the slow time, and  $\xi = \epsilon x$  for the long space. We construct the expansions

$$\omega = \omega_0 + \epsilon\omega_1 + \epsilon^2\omega_2 + \dots,$$

$$\phi_1 = \Sigma_{n=1} \epsilon^n \phi_{1n}(y, z, \tilde{t}; \xi, \tau),$$

$$\phi_2 = \Sigma_{n=1} \epsilon^n \phi_{2n}(y, z, \tilde{t}; \xi, \tau).$$

The original field equations  $\nabla^2 \phi_i$  become

$$\nabla_2^2 \phi_{i1} = 0, \quad \nabla_2^2 \phi_{i2} = 0, \quad \nabla_2^2 \phi_{i3} = -\frac{\partial^2}{\partial \xi^2} \phi_{i1}, \quad (\text{A.10})$$

where  $\nabla_2^2 = \partial_y^2 + \partial_z^2$  and  $\partial_y = \partial/\partial y$ ,  $\partial_z = \partial/\partial z$ . Now, solving the Laplace equations, Equations A.10 with the wall-boundary conditions and the conditions on the internal surface, Equations A.7 and A.8, taken by orders of  $\epsilon$ , we obtain the following first-order solution.

$$\begin{aligned} \phi_{11} &= -\frac{T_2}{T_1} R_1(\tilde{t}; \xi, \tau) \cos(ky) \frac{\cosh(k(z - h_1))}{\cosh(kh_1)}, \\ \phi_{21} &= R_1(\tilde{t}; \xi, \tau) \cos(ky) \frac{\cosh(k(z + h_2))}{\cosh(kh_2)}, \\ R_1(\tilde{t}; \xi, \tau) &= \psi(\xi, \tau) \exp(-i\tilde{t}) + c.c., \end{aligned} \quad (\text{A.11})$$

where c.c. denotes the complex conjugate of its preceding term and

$$\begin{aligned} \omega_0^2 &= \frac{gkT_1T_2(1 - \nu)}{T_1 + \nu T_2} \quad \text{with} \\ T_1 &= \tanh(kh_1) \quad \text{and} \\ T_2 &= \tanh(kh_2). \end{aligned} \quad (\text{A.12})$$

The first-order solution gives the dispersion relation for linear waves on the internal interface. Examination of the second-order system requires that  $\omega_1 = 0$  in order to suppress secularity. Solving for the particular solutions yields

$$\begin{aligned} \phi_{12} &= R_2(\tilde{t}; \xi, \tau) C_1 \cos(2ky) [\cosh(2kz) - \frac{2T_1}{1 + T_1^2} \sinh(2kz)], \quad \text{and} \\ \phi_{22} &= R_2(\tilde{t}; \xi, \tau) \left( C_2 + C_3 \cos(2ky) [\cosh(2kz) + \frac{2T_2}{1 + T_2^2} \sinh(2kz)] \right), \end{aligned}$$

with

$$R_2(\tilde{t}; \xi, \tau) = i\psi(\xi, \tau)^2 \exp(-2i\tilde{t}) + c.c.,$$

and  $C_1, C_2$  and  $C_3$  are known functions of  $k, h_1, h_2$  and  $\nu$ . Finally, in the third-order analysis, suppression of the secular terms yields, for  $\psi(\xi, \tau)$ , the familiar equation

$$2i\omega_0^2\psi_\tau + c_s^2\psi_{\xi\xi} + 2\omega_0\omega_2\psi + 2\gamma\omega_0^2\psi^* + A_s|\psi|^2\psi = 0, \quad (\text{A.13})$$

where

$$\begin{aligned} c_s^2 &= \frac{g(1-\nu)}{2k(T_1 + \nu T_2)^2} (h_2 k T_1^2 (1 - T_2^2) + T_1^2 T_2 + \nu h_1 k T_2^2 (1 - T_1^2) + \nu T_1 T_2^2) \\ A_s &= \frac{k^4 (a_0 + a_1 \nu + a_2 \nu^2 + a_3 \nu^3)}{8T_1^3 T_2 (\nu T_1 + T_2) (T_1 + \nu T_2)^2}, \end{aligned} \quad (\text{A.14})$$

with

$$\begin{aligned} a_0 &= T_1^5 (-9 + 16T_2^2 - 5T_2^4 + 6T_2^6), \\ a_1 &= T_1^2 T_2 (-9T_1^2 + 10T_1^4 + 18T_1 T_2 - 6T_1^3 T_2 + 10T_1^2 T_2^2 - \\ &\quad - 4T_1^4 T_2^2 - 18T_1 T_2^3 + 6T_1^3 T_2^3 + 4T_2^4 - T_1^2 T_2^4 + \\ &\quad + 6T_1^4 T_2^4 + 4T_1 T_2^5 - 12T_1^3 T_2^5), \\ a_2 &= T_1 T_2^2 (4T_1^4 + 18T_1 T_2 - 18T_1^3 T_2 + 4T_1^5 T_2 - 9T_2^2 + \\ &\quad + 10T_1^2 T_2^2 - T_1^4 T_2^2 - 6T_1 T_2^3 + 6T_1^3 T_2^3 - 12T_1^5 T_2^3 + \\ &\quad + 10T_2^4 - 4T_1^2 T_2^4 + 6T_1^4 T_2^4), \\ a_3 &= (-9 + 16T_1^2 - 5T_1^4 + 6T_1^6) T_2^5. \end{aligned}$$

Note that when  $\nu \rightarrow 0$ , so that the density of the upper liquid goes to zero, the coefficients reduce to those for the case of the homogeneous liquid. The coefficient  $c_s^2$  is always positive. The nonlinearity coefficient,  $A_s$ , depends upon  $h_1, h_2, \nu$  and  $k$ . Figure A.2 shows the nonlinearity coefficient as a function of  $k$  and  $\nu$  for fixed

$h_1 = h_2 = 1$ . When  $\nu = 0$ , the dependence on  $k$  is that shown in Chapter 2. The depth at which the nonlinearity coefficient changes sign may be solved as a function of  $h_1, h_2, \nu$  and  $k$ . The critical wave number decreases as  $\nu$  increases, as shown in the figure. We can also plot the nonlinearity coefficient as a function of  $h_2$  and  $\nu$  for fixed  $k$  and  $h_1$ . Figure A.3 shows a plot of  $A_s$  in this case. Here, the point at which  $A_s = 0$  decreases in  $h_2$ , with increasing  $\nu$ .

Once Equation A.13 is obtained, we can use all of the analysis from the single-layer case to analyze the stratified-liquid system. Therefore, we expect to observe the standing, solitary-wave (“sech”) solution when  $A_s > 0$  and the kink wave, when  $A_s < 0$ . The stability properties should also apply when the parameters are properly scaled.

Some preliminary experimental observations were made for sloshing solitons on the internal interface of two liquids. We used kerosene for the top liquid and water for the lower liquid. The experimental apparatus is the same as that used for the homogeneous liquid case. The tank is one inch by nineteen inches and is constructed of lucite. liquid depths,  $h_1$  and  $h_2$ , ranged from one to two inches. The value of the density ratio,  $\nu$ , is 0.85 for the kerosene and water combination. The main features of the standing soliton were observed. A stable soliton was produced, with its amplitude and characteristic length matching reasonably well with the predicted values. The absolute-forcing amplitudes tended to be much greater for the internal-interface case than for the homogeneous-layer case. That this is so may be seen by examining  $\gamma = a_0\omega_0^2/g$ . The natural frequency,  $\omega_0$ , is much lower for the stratified liquid, so that  $a_0$  must increase to give the same value of  $\gamma$ . A more detailed experimental study of sloshing waves for the stratified liquid

requires more work than has been done to date.

## **Figures for Appendix A**

### Rigid Top Surface

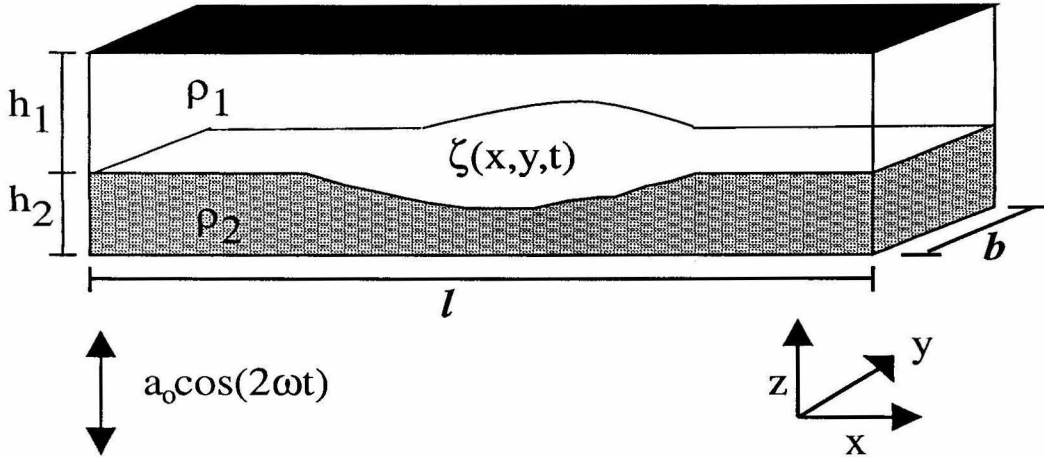


Figure A.1: Schematic of experimental apparatus for the two-layer, stratified liquid.

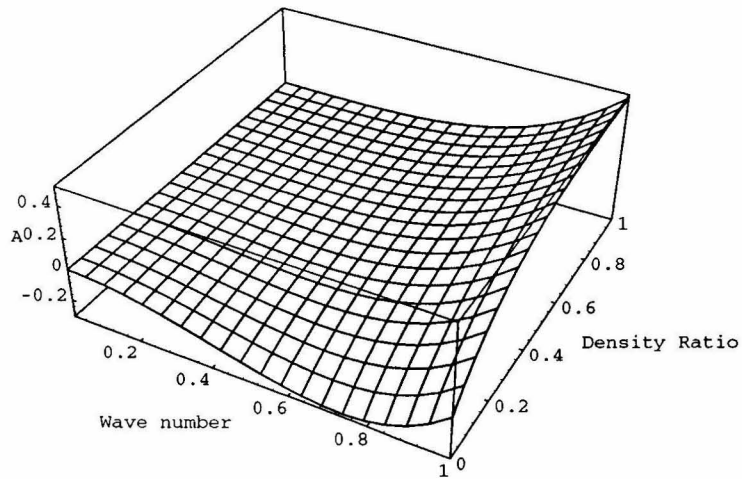


Figure A.2: The nonlinear, self-interaction coefficient,  $A$ , versus  $k$  and  $\nu$  for fixed  $h_1$  and  $h_2$ .

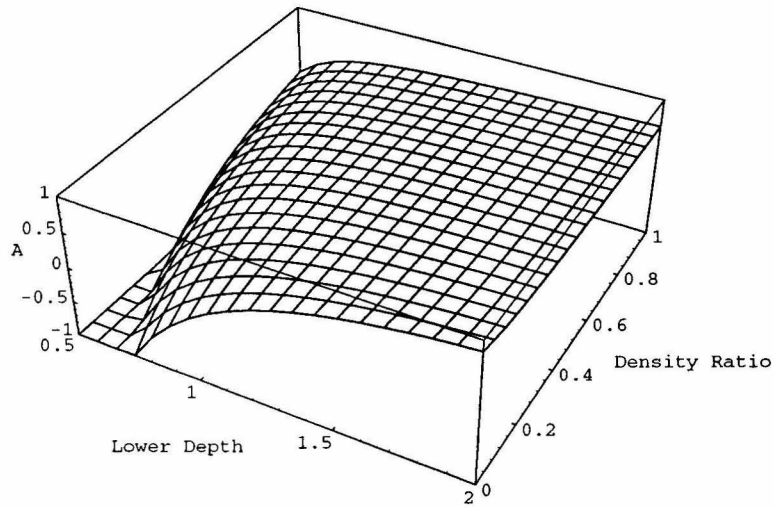


Figure A.3: The nonlinear, self-interaction coefficient,  $A$ , versus  $h_2$  and  $\nu$  for fixed  $k$  and  $h_1$ .

## Appendix B

# Center Manifold for the Flat Surface

When analyzing the stability of the flat-surface solution ( $r_0 \equiv 0$ ) of Equation 2.9, we find that the stability analysis breaks down when  $\gamma = \sqrt{\alpha^2 + (\beta - \kappa^2 c^2)} \equiv \gamma_c$ , as shown in Chapter 3.3.1. If  $\xi$  dependence in the NLS equation is neglected, we use the center-manifold theory to determine the stability of the solution along the critical surface  $\gamma = \gamma_c$ . Here,  $\sigma_{1,2} = (0, -2\alpha)$ , and the system looks like

$$\frac{d}{d\tau} \begin{pmatrix} p \\ q \end{pmatrix} = \begin{pmatrix} -\alpha & -\beta + \gamma_c \\ \beta + \gamma_c & -\alpha \end{pmatrix} \begin{pmatrix} p \\ q \end{pmatrix} + A \begin{pmatrix} -q(p^2 + q^2) \\ p(p^2 + q^2) \end{pmatrix}. \quad (\text{B.1})$$

Transform the system so that the two-by-two matrix is diagonal, and let  $Q$  be the two-by-two matrix whose columns are the eigenvectors of our linear system such that

$$\begin{pmatrix} r \\ s \end{pmatrix} = Q^{-1} \begin{pmatrix} p \\ q \end{pmatrix}.$$

Substitution into Equation B.1 gives

$$\frac{d}{d\tau} \begin{pmatrix} r \\ s \end{pmatrix} = \begin{pmatrix} 0 & 0 \\ 0 & -2\alpha \end{pmatrix} \begin{pmatrix} r \\ s \end{pmatrix} + \begin{pmatrix} f_1(r, s) \\ f_2(r, s) \end{pmatrix},$$

where  $f_1(r, s)$  and  $f_2(r, s)$  are known functions of their arguments. Following Wiggins (1990), the question of stability of the system at  $\gamma = \gamma_c$  is reduced to the

equation on the center manifold,

$$\frac{d}{d\tau}r = \frac{2A\beta}{\alpha} \frac{\sqrt{\alpha^2 + \beta^2}}{\beta + \sqrt{\alpha^2 + \beta^2}} r^3 + O(r^5). \quad (\text{B.2})$$

For small  $r$ , a positive coefficient of  $r^3$  indicates *instability*. Therefore, the condition for instability is

$$A\beta > 0, \quad (\text{B.3})$$

which is the desired result.

## Appendix C

# Eigenfunction-Construction Algorithm

The linear-stability analysis of Chapters 3 and 4 relies upon an algorithm for constructing approximate eigenfunctions of the linearized, perturbation equations, Equations 3.10 and 4.6. This appendix describes the algorithm for the construction of the eigenfunctions and for the numerical search for eigenvalues. Both continuous-spectrum eigenfunctions and discrete-spectrum eigenfunctions may be constructed. The same system is used for both the hyperbolic-tangent and the hyperbolic-secant cases, although the actual numerical codes differ in the detailed nature of the coefficients.

An outline of our procedure follows, and the detailed constructions for Equations 3.10 and 4.6 are presented in the subsequent sections. The system of interest consists of two coupled equations, second-order in  $\xi$ , that are singular as  $\xi \rightarrow \pm\infty$ . The eigenvalue is  $\bar{\sigma}$ . First, we make the transformation  $z = \tanh(\xi)$  to bring the regular singular points from infinity to  $\pm 1$ . Using a result from ordinary differential equation theory, we construct four Frobenius series at each singular point. There are four series at each point corresponding to four indices. We distinguish

two cases, depending upon the form of the indices. When at least one pair of indices is imaginary, the eigenfunctions belong to the continuous spectrum of the linear operator, which will be treated later in the appendix. When the indices possess nonzero real part, only those indices with positive real part contribute to eigenfunctions that satisfy the boundary conditions. In this case, each singular point has two acceptable indices leading to two undetermined constants at each singular point. Using a result from the theory of ordinary differential equations, the Frobenius series are known to converge in a circular region, extending to the nearest neighboring singular point. Therefore, the series solutions starting at  $z = -1$  converge for  $z \in [-1, 1)$ , while the series solutions starting at  $z = 1$  converge for  $z \in (-1, 1]$ . An eigenfunction of the linear system must approach each singular point along a combination of the two series solutions found near each singular point. To construct a complete eigenfunction across the entire interval  $[-1, 1]$ , we match the two series smoothly, starting at  $z = -1$  to those from  $z = 1$  at any intermediate point  $z_o \in [-1, 1]$ , by requiring that the solutions  $(p_{-1}, q_{-1})$  starting at  $z = -1$  and those at  $z = 1$   $(p_{+1}, q_{+1})$  satisfy

$$\begin{aligned} p_{-1}(z_o) &= p_{+1}(z_o), \\ q_{-1}(z_o) &= q_{+1}(z_o), \\ p'_{-1}(z_o) &= p'_{+1}(z_o), \quad \text{and} \\ q'_{-1}(z_o) &= q'_{+1}(z_o). \end{aligned} \tag{C.1}$$

The first two conditions require continuity of the functions and the second two conditions require continuity of the first derivatives. Application of the differential equations will ensure the continuity of all higher derivatives so that Conditions C.1 ensure a completely smooth eigenfunction. Conditions C.1 impose four conditions

on four undetermined, complex constants (the coefficients of the two series at the two singular points), leading to a four-by-four matrix whose determinant must be zero to satisfy the Equations C.1 with a nontrivial solution. Therefore, eigenvalues are the values of  $\bar{\sigma}$  that make the aforementioned determinant zero. The hyperbolic-secant and the hyperbolic-tangent cases follow, illustrating the application of the algorithm.

## C.1 Matching Code for the Standing Soliton

The detailed scheme for finding eigenvalues and constructing eigenfunctions of the linear-stability equation for the hyperbolic-secant, stationary solution of the NLS equation follows. We start with Equation 3.10 and Definitions 3.11 from Chapter 3. Letting  $z = \tanh(\xi)$  gives us the system

$$\begin{aligned} -(\bar{\sigma} + 2\bar{\alpha}) q + (1 - z^2)^2 p'' - 2z(1 - z^2) p' - p + 6(1 - z^2) p &= 0, \\ \bar{\sigma} p + (1 - z^2)^2 q'' - 2z(1 - z^2) q' - m q + 2(1 - z^2) q &= 0, \end{aligned} \quad (\text{C.2})$$

where ' denotes differentiation with respect to  $z$ ,  $\frac{d}{dz}$ . Now, we look for the Frobenius series about the point  $z = 1$  in the usual way. Let

$$\begin{aligned} p(z) &= (1 - z)^r \sum_{n=0}^{\infty} a_n (1 - z)^n \quad \text{and} \\ q(z) &= (1 - z)^r \sum_{n=0}^{\infty} b_n (1 - z)^n, \end{aligned} \quad (\text{C.3})$$

and substitute the expansions into the differential system, Equations C.2. By equating powers of  $(1 - z)$ , we obtain the form of the indices,  $r$ , as well as a recursive relationship for the coefficients,  $a_n$  and  $b_n$ . Equating powers of  $(1 - z)^r$  in the differential system leads to

$$r = \pm \frac{1}{2^{3/2}} \sqrt{1 + m \pm \sqrt{(1 - m)^2 - 4\bar{\sigma}(\bar{\sigma} + 2\bar{\alpha})}} \quad \text{and}$$

$$b_0 = \frac{\bar{\sigma}}{m - 4r^2} a_0, \quad (\text{C.4})$$

giving the four indices and the relationship between the first-order terms of  $p$  and  $q$ . The recursive definition of the coefficients is

$$\begin{aligned} a_n &= A_1 a_{n-1} + A_2 a_{n-2} + A_3 b_{n-1} + A_4 b_{n-2} \quad \text{and} \\ b_n &= B_1 a_{n-1} + B_2 a_{n-2} + B_3 b_{n-1} + B_4 b_{n-2}, \end{aligned} \quad (\text{C.5})$$

where

$$\begin{aligned} A_1 &= \frac{2}{p_0}(m - 4n^2 - 8nr - 4r^2)(5 + 3n - 2n^2 + 3r - 4nr - 2r^2), \\ A_2 &= \frac{1}{p_0}(m - 4n^2 - 8nr - 4r^2)(-4 - 3n + n^2 - 3r + 2nr + r^2), \\ A_3 &= \frac{2}{p_0}(1 + 3n - 2n^2 + 3r - 4nr - 2r^2)(2\bar{\alpha} + \bar{\sigma}), \\ A_4 &= \frac{1}{p_0}(-3n + n^2 - 3r + 2nr + r^2)(2\bar{\alpha} + \bar{\sigma}), \\ B_1 &= \frac{2}{p_0}(5 + 3n - 2n^2 + 3r - 4nr - 2r^2)\bar{\sigma}, \\ B_2 &= \frac{1}{p_0}(-4 - 3n + n^2 - 3r + 2nr + r^2)\bar{\sigma}, \\ B_3 &= \frac{2}{p_0}(1 + 3n - 6n^2 - 12n^3 + 8n^4 + 3r - 12nr - 36n^2r + 32n^3r - \\ &\quad - 6r^2 - 36nr^2 + 48n^2r^2 - 12r^3 + 32nr^3 + 8r^4), \\ B_4 &= \frac{1}{p_0}(-3n + n^2 + 12n^3 - 4n^4 - 3r + 2nr + 36n^2r - 16n^3r + r^2 + \\ &\quad + 36nr^2 - 24n^2r^2 + 12r^3 - 16nr^3 - 4r^4) \quad \text{and} \\ p_0 &= m - 4n^2 - 4mn + 16n^4 - 8nr - 8mnr + 64n^3r - 4r^2 - 4mr^2 + \\ &\quad + 96n^2r^2 + 64nr^3 + 16r^4 + \bar{\sigma}(2\bar{\alpha} + \bar{\sigma}). \end{aligned} \quad (\text{C.6})$$

Now, for a given index,  $r$ , each series for  $p$  and  $q$  is determined up to the constant  $a_0$ , when  $\bar{\alpha}, \bar{\sigma}$  and  $m$  are fixed. Without loss of generality, take  $a_0 = 1$ , so that each one of the four possible series is completely determined up to a multiplicative

constant. Each of the four indices leads to a different series in  $a_n$  and  $b_n$ . The cases for a repeated index and for indices separated by integer cause the above series to break down. However, new series may be constructed in this case (see Ince (1926)). Notice that the indices and the recursion relations at  $z = -1$  are the same as those derived above, since the equation is symmetric about  $z = 0$ .

### C.1.1 Discrete-Spectrum Eigenvalues

We construct an eigenfunction as follows. Let the four series given by  $r_j$  be denoted

$$\begin{aligned} p_j^+(z) &= (1-z)^{r_j} \sum a_n^j (1-z)^n, \\ q_j^+(z) &= (1-z)^{r_j} \sum b_n^j (1-z)^n, \\ p_j^-(z) &= (1+z)^{r_j} \sum a_n^j (1+z)^n, \quad \text{and} \\ q_j^-(z) &= (1+z)^{r_j} \sum b_n^j (1+z)^n, \end{aligned}$$

with  $j = 1, \dots, 4$ . Any solution of the differential system, System C.2, with  $z \in (-1, +1]$ , may be expressed in the form

$$\begin{aligned} p_{+1}(z) &= C_1 p_1^+(z) + C_2 p_2^+(z) + C_3 p_3^+(z) + C_4 p_4^+(z), \\ q_{+1}(z) &= C_1 q_1^+(z) + C_2 q_2^+(z) + C_3 q_3^+(z) + C_4 q_4^+(z). \end{aligned} \quad (\text{C.7})$$

Likewise, the *same* solution with  $z \in [-1, +1)$  may be expressed in the form

$$\begin{aligned} p_{-1}(z) &= D_1 p_1^-(z) + D_2 p_2^-(z) + D_3 p_3^-(z) + D_4 p_4^-(z), \\ q_{-1}(z) &= D_1 q_1^-(z) + D_2 q_2^-(z) + D_3 q_3^-(z) + D_4 q_4^-(z). \end{aligned} \quad (\text{C.8})$$

Consider the case when all four indices have nonzero real part. From the form of the index equation, Equation C.4, two indices will have positive real part and two will have negative real part. The indices with negative real part lead to series

solutions that are singular at  $z = \pm 1$ , thereby failing to satisfy the boundary conditions on  $p$  and  $q$ . Therefore, only two of the four series may be present in this case. Let  $r_1$  and  $r_2$  denote the two indices with positive real part. The series representation of the solutions is reduced to

$$\begin{aligned} p_{+1}(z) &= C_1 p_1^+(z) + C_2 p_2^+(z), \\ q_{+1}(z) &= C_1 q_1^+(z) + C_2 q_2^+(z), \quad \text{and} \\ p_{-1}(z) &= D_1 p_1^-(z) + D_2 p_2^-(z), \quad \text{with} \\ q_{-1}(z) &= D_1 q_1^-(z) + D_2 q_2^-(z). \end{aligned}$$

Application of the conditions required for a smooth solution spanning the range  $[-1, 1]$ , Conditions C.1, and satisfying the boundary conditions lead to

$$\begin{pmatrix} p_1^+(z_o) & p_2^+(z_o) & -p_1^-(z_o) & -p_2^-(z_o) \\ q_1^+(z_o) & q_2^+(z_o) & -q_1^-(z_o) & -q_2^-(z_o) \\ p_1'^+(z_o) & p_2'^+(z_o) & -p_1'^-(z_o) & -p_2'^-(z_o) \\ q_1'^+(z_o) & q_2'^+(z_o) & -q_1'^-(z_o) & -q_2'^-(z_o) \end{pmatrix} \begin{pmatrix} C_1 \\ C_2 \\ D_1 \\ D_2 \end{pmatrix} \equiv M \begin{pmatrix} C_1 \\ C_2 \\ D_1 \\ D_2 \end{pmatrix} = 0, \quad (\text{C.9})$$

where the prime denotes differentiation with respect to  $z$ . In order for a nontrivial solution to exist, defined on  $[-1, 1]$ , the above four-by-four matrix must have a zero determinant,  $\det(M) = 0$ . However, the matrix  $M$  is a function of  $\bar{\alpha}$ ,  $\bar{\sigma}$  and  $m$ . Therefore, for fixed  $m$  and  $\bar{\alpha}$ , the values of  $\bar{\sigma}$  that lead to a zero determinant are eigenvalues. The corresponding eigenfunctions are found by determining the relationship between  $C_1, C_2, D_1$  and  $D_2$ , given by the independent rows of  $M$ . To find the eigenvalues numerically, we truncate the series at  $n = N$  (usually  $N = 40$ ), and search for the zeros of  $\det(M)$  by using a two-dimensional, Newton-Raphson root-finding algorithm to find  $\bar{\sigma} = \bar{\sigma}_r + i\bar{\sigma}_i$ . As usual with a Newton-Raphson scheme, a good initial guess for  $\bar{\sigma}$  is required in order for the numerical scheme to converge. By using the asymptotic solutions found in Chapter 3 for the discrete-

spectrum solutions, we provide good initial guesses for small  $\tilde{\gamma}$ . Then, we march in small steps of  $\tilde{\gamma}$ , finding  $\bar{\sigma}$  at each step and using the previous step's  $\bar{\sigma}$  as the initial guess for each subsequent step. Using this procedure, the eigenvalue approximations converge to machine accuracy in five to ten iterations per  $\tilde{\gamma}$  step. In this way, numerical approximations to the discrete-spectrum, eigenvalue branches are constructed.

### C.1.2 Continuous-Spectrum Eigenvalues

When the eigenvalue and parameters are such that the indices of the differential system possess at least one purely imaginary pair, the eigenfunctions have a different character, that of the continuous spectrum of the operator. Assume that one pair of the indices given by Equation C.4 is purely imaginary and that the other pair has nonzero real part. Let  $r_{1,2} = \pm i\rho$  and  $r_3$  possess positive real part. The boundary condition on  $p$  and  $q$  requires that they go to zero when  $z = \pm 1$ . However, in analogy with the continuous spectrum of the linear Schrödinger equation, we relax the boundary conditions at the singular points, requiring eigenfunctions to be bounded at  $z = \pm 1$ . We show later that a synthesis of these continuous-spectrum eigenfunctions satisfies the boundary conditions. As before, any solution of System C.2 may be represented as the two series solutions given by Equations C.7 and C.8. In order for the solution to be bounded at the singular points, we require the coefficient of the  $r_4$  series to be zero, and the two representations become

$$\begin{aligned} p_{+1}(z) &= C_1 p_1^+(z) + C_2 p_2^+(z) + C_3 p_3^+(z), \\ q_{+1}(z) &= C_1 q_1^+(z) + C_2 q_2^+(z) + C_3 q_3^+(z), \quad \text{and} \\ p_{-1}(z) &= D_1 p_1^-(z) + D_2 p_2^-(z) + D_3 p_3^-(z), \quad \text{with} \end{aligned}$$

$$q_{-1}(z) = D_1 q_1^-(z) + D_2 q_2^-(z) + D_3 q_3^-(z).$$

Now, application of the matching conditions, Conditions C.1, give the linear system

$$\begin{pmatrix} p_1^+(z_o) & p_2^+(z_o) & -p_1^-(z_o) & -p_2^-(z_o) \\ q_1^+(z_o) & q_2^+(z_o) & -q_1^-(z_o) & -q_2^-(z_o) \\ p_1'^+(z_o) & p_2'^+(z_o) & -p_1'^-(z_o) & -p_2'^-(z_o) \\ q_1'^+(z_o) & q_2'^+(z_o) & -q_1'^-(z_o) & -q_2'^-(z_o) \end{pmatrix} \begin{pmatrix} C_1 \\ C_2 \\ D_1 \\ D_2 \end{pmatrix} \equiv M \begin{pmatrix} C_1 \\ C_2 \\ D_1 \\ D_2 \end{pmatrix} = \begin{pmatrix} -p_3^+(z_o) & p_3^-(z_o) \\ -q_3^+(z_o) & q_3^-(z_o) \\ -p_3'^+(z_o) & p_3'^-(z_o) \\ -q_3'^+(z_o) & q_3'^-(z_o) \end{pmatrix} \begin{pmatrix} C_3 \\ D_3 \end{pmatrix}. \quad (\text{C.10})$$

For the present system, the linear system above always possesses nontrivial solutions. If the determinant of  $M$  is zero, we are free to set  $C_3$  and  $D_3$  to zero, and we can construct an eigenfunction. If the determinant of  $M$  is nonzero, specifying  $C_3/D_3$  and solving the above system for  $C_1, C_2, D_1$  and  $D_2$  fixes the eigenfunction to within a multiplicative constant. The case of two pairs of purely imaginary indices proceeds in the same way. In the case of two pairs of imaginary indices, all four series must be included in each solution. The matching process leads to four conditions on eight constants. Again, the requirement for smooth solutions can always be satisfied so that values of  $\sigma$  leading to two pairs of purely imaginary indices are also continuous-spectrum eigenvalues.

Lastly, we show that the solutions of System C.2 can be constructed containing the continuous spectrum such that they satisfy the boundary conditions  $p(\pm 1) = q(\pm 1) = 0$ . Any parts of the solution that approach the singular points with an index having positive real part clearly satisfy the boundary condition. For the parts of a solution with a purely imaginary index, we note that the eigenvalues leading to purely imaginary indices occur in a continuous range (for example,  $\sigma_r \in [\sigma_{rmin}, \sigma_{rmax}]$ ). Therefore, while a single eigenfunction does not satisfy the

boundary conditions, a general solution of the linear system is a synthesis of the continuous-spectrum eigenfunctions and the discrete-spectrum eigenfunctions. The oscillatory part of a solution approaches the singular point at  $z = -1$  as

$$p(z) \sim \int_{\sigma_{rmin}}^{\sigma_{rmax}} F_1(\sigma)(1+z)^{i\rho(\sigma)} d\sigma + \int_{\sigma_{rmin}}^{\sigma_{rmax}} F_2(\sigma)(1+z)^{-i\rho(\sigma)} d\sigma,$$

where  $F_1$  and  $F_2$  are well-behaved, weighting functions determined by the initial conditions. The integrals may be written

$$\int_{\sigma_{rmin}}^{\sigma_{rmax}} F_i(\sigma)e^{\pm i\rho(\sigma)\ln(1+z)} d\sigma.$$

By using the method of stationary phase, the above expression can be shown to go to zero as  $z \rightarrow -1$ . The behavior of  $q$  is similar. Therefore, the synthesis of the continuous-spectrum eigenfunctions satisfies the boundary conditions. The range of eigenvalues leading to purely imaginary indices is outlined in Chapter 3.

## C.2 Matching Code for the Kink Wave

The matching algorithm for the linear-stability operator for the hyperbolic-tangent solution is the same as that presented above, with changes in the coefficients and indices reflecting the changes in the governing equation, Equation 4.6. The transformation  $z = \tanh(\xi)$  applied to Equation 4.6 leads to

$$\begin{aligned} -(\bar{\sigma} + 2\bar{\alpha}) q + (1 - z^2)^2 p'' - 2z(1 - z^2) p' - 4p + 6(1 - z^2) p &= 0, \\ \bar{\sigma} p + (1 - z^2)^2 q'' - 2z(1 - z^2) q' - m q + 2(1 - z^2) q &= 0, \end{aligned} \quad (\text{C.11})$$

where

$$\bar{\sigma} = \frac{2\sigma}{\beta + \tilde{\gamma}}, \quad (\text{C.12})$$

$$\bar{\alpha} = \frac{2\alpha}{\beta + \tilde{\gamma}} \quad \text{and} \quad (\text{C.13})$$

$$m = \frac{4\tilde{\gamma}}{\beta + \tilde{\gamma}}. \quad (\text{C.14})$$

Construct the Frobenius series about  $z = 1$  by taking

$$\begin{aligned} p(z) &= (1-z)^r \sum_{n=0}^{\infty} a_n (1-z)^n \quad \text{and} \\ q(z) &= (1-z)^r \sum_{n=0}^{\infty} b_n (1-z)^n \end{aligned} \quad (\text{C.15})$$

and substituting into System C.11. Solving the equations by order of  $(1-z)$  gives for the index and the relationship between the first-order terms

$$\begin{aligned} r &= \pm \frac{1}{2^{3/2}} \sqrt{4 + m \pm \sqrt{(m-4)^2 - 4\bar{\sigma}(\bar{\sigma} + 2\bar{\alpha})}} \quad \text{and} \\ b_0 &= \frac{4(r^2 - 1)}{\bar{\sigma} + 2\bar{\alpha}} a_0. \end{aligned} \quad (\text{C.16})$$

The recursive definitions for the series coefficients are

$$\begin{aligned} a_n &= A_1 a_{n-1} + A_2 a_{n-2} + A_3 b_{n-1} + A_4 b_{n-2} \quad \text{and} \\ b_n &= B_1 a_{n-1} + B_2 a_{n-2} + B_3 b_{n-1} + B_4 b_{n-2}, \end{aligned} \quad (\text{C.17})$$

where

$$\begin{aligned} A_1 &= \frac{2}{p_0} (m - 4n^2 - 8nr - 4r^2)(5 + 3n - 2n^2 + 3r - 4nr - 2r^2), \\ A_2 &= \frac{1}{p_0} (m - 4n^2 - 8nr - 4r^2)(-4 - 3n + n^2 - 3r + 2nr + r^2), \\ A_3 &= \frac{-2}{p_0} (1 + 3n - 2n^2 + 3r - 4nr - 2r^2)(2\bar{\alpha} + \bar{\sigma}), \\ A_4 &= \frac{-1}{p_0} (-3n + n^2 - 3r + 2nr + r^2)(2\bar{\alpha} + \bar{\sigma}), \\ B_1 &= \frac{2}{p_0} (5 + 3n - 2n^2 + 3r - 4nr - 2r^2)\bar{\sigma}, \\ B_2 &= \frac{1}{p_0} (-4 - 3n + n^2 - 3r + 2nr + r^2)\bar{\sigma}, \end{aligned}$$

$$\begin{aligned}
 B_3 &= \frac{8}{p_0}(1 + 3n - 3n^2 - 3n^3 + 2n^4 + 3r - 6nr - 9n^2r + 8n^3r - \\
 &\quad - 3r^2 - 9nr^2 + 12n^2r^2 - 3r^3 + 8nr^3 + 2r^4), \\
 B_4 &= \frac{4}{p_0}(-3n + n^2 + 3n^3 - n^4 - 3r + 2nr + 9n^2r - 4n^3r + r^2 + \\
 &\quad + 9nr^2 - 6n^2r^2 + 3r^3 - 4nr^3 - r^4) \quad \text{and} \\
 p_0 &= 4m - 16n^2 - 4mn^2 + 16n^4 - 32nr - 8mnr + 64n^3r - 16r^2 - 4mr^2 + \\
 &\quad + 96n^2r^2 + 64nr^3 + 16r^4 + \bar{\sigma}(2\bar{\alpha} + \bar{\sigma}). \tag{C.18}
 \end{aligned}$$

The construction of the discrete spectrum and the continuous spectrum proceeds as for the hyperbolic-secant case. The discrete spectrum exists where the indices all possess nonzero real part. Where the indices possess one or two purely imaginary pairs, the eigenvalue belongs to the continuous spectrum. Results for the spectra are given in Chapter 4.

## Appendix D

# Perturbation Expansion for Bound-Mode Eigenvalues

The discrete spectrum of the linear operator for the stability of the standing soliton of Chapter 3 is found numerically. However, we need a starting point for the numerical code as well as a way to verify the numerical results. Both are provided by constructing an asymptotic expansion of the eigenvalue branch near a known, neutrally stable solution. Consider the linear system given by Equation 3.10 and repeated as follows,

$$\begin{aligned} -\bar{\sigma}q - 2\bar{\alpha}q + p_{\xi\xi} - p + 6\text{sech}^2(\xi)p &= 0, \\ \bar{\sigma}p + q_{\xi\xi} - mq + 2\text{sech}^2(\xi)q &= 0, \end{aligned} \tag{D.1}$$

with

$$\begin{aligned} m &= \frac{\beta + \tilde{\gamma}}{\beta - \tilde{\gamma}}, \\ \bar{\sigma} &= \frac{\sigma}{-\beta + \tilde{\gamma}} \quad \text{and} \\ \bar{\alpha} &= \frac{\alpha}{-\beta + \tilde{\gamma}}. \end{aligned} \tag{D.2}$$

The boundary conditions require  $(p, q) \rightarrow (0, 0)$  as  $\xi \rightarrow \pm\infty$ . We can find exact solutions of the above system when  $\tilde{\gamma} = 0$  and  $\bar{\alpha} = 0$ . In this case,  $m = 1$ ,  $\bar{\sigma} = 0$ ,

and the solutions are the Legendre functions

$$\begin{aligned} p_0 &= C_p \operatorname{sech}(\xi)\tanh(\xi), \\ q_0 &= C_q \operatorname{sech}(\xi). \end{aligned} \tag{D.3}$$

The coefficients  $C_p$  and  $C_q$  are real and independent constants. We construct an expansion for small  $\tilde{\gamma}$  and small  $\bar{\alpha}$  as follows. Let  $\delta \ll 1$  be an arbitrary, positive, small parameter and define the following series in  $\delta$ ,

$$\begin{aligned} p(\xi) &= p_0(\xi) + \delta p_1(\xi) + \delta^2 p_2(\xi) + O(\delta^3), \\ q(\xi) &= q_0(\xi) + \delta q_1(\xi) + \delta^2 q_2(\xi) + O(\delta^3), \\ \bar{\sigma} &= \delta \bar{\sigma}_1 + \delta^2 \bar{\sigma}_2 + O(\delta^3), \\ \bar{\alpha} &= \delta \bar{\alpha}_1, \\ \tilde{\gamma} &= \delta^2 \tilde{\gamma}_2, \quad \text{and} \\ m &= 1 + \delta^2 \frac{2\tilde{\gamma}_2}{\beta} + O(\delta^4). \end{aligned} \tag{D.4}$$

At  $O(1)$ , the first-order terms in the expansion satisfy

$$\begin{aligned} L_p(p_0) &\equiv p_{0\xi\xi} - p_0 + 6\operatorname{sech}^2(\xi)p_0 = 0, \\ L_q(q_0) &\equiv q_{0\xi\xi} - q_0 + 2\operatorname{sech}^2(\xi)q_0 = 0. \end{aligned} \tag{D.5}$$

The solution of the above system is given by Equation D.3, where  $C_p$  and  $C_q$  are independent, real constants. The next order,  $O(\delta)$ , is given by

$$\begin{aligned} L_p(p_1) &= (\bar{\sigma}_1 + 2\bar{\alpha}_1)q_0, \\ L_q(q_1) &= -\bar{\sigma}_1 p_0. \end{aligned} \tag{D.6}$$

In both of the above equations, the forcing function is orthogonal to the solution of the homogeneous equation, so that a particular solution exists. The particular

solutions are

$$\begin{aligned} p_1(\xi) &= \frac{1}{2}C_q(\bar{\sigma}_1 + 2\bar{\alpha}_1) (\operatorname{sech}(\xi) - \xi \operatorname{sech}(\xi)\tanh(\xi)), \\ q_1(\xi) &= \frac{1}{2}C_p\bar{\sigma}_1 \xi \operatorname{sech}(\xi). \end{aligned} \quad (\text{D.7})$$

The third-order system,  $O(\delta^2)$  is

$$\begin{aligned} L_p(p_2) &= (\bar{\sigma}_1 + 2\bar{\alpha}_1)q_1 + \bar{\sigma}_2q_0, \\ L_q(q_2) &= -\bar{\sigma}_1p_1 + 2\frac{\tilde{\gamma}_2}{\beta}q_0 - \bar{\sigma}_2p_0. \end{aligned} \quad (\text{D.8})$$

For the system above, application of the Fredholm Alternative Theorem on each of the equations requires that

$$\begin{aligned} (\bar{\sigma}_1 + 2\bar{\alpha}_1) \int_{-\infty}^{+\infty} q_1p_0 \, d\xi &= 0, \quad \text{and} \\ 2\frac{\tilde{\gamma}_2}{\beta} \int_{-\infty}^{+\infty} q_0^2 \, d\xi - \bar{\sigma}_1 \int_{-\infty}^{+\infty} p_1q_0 \, d\xi &= 0, \end{aligned}$$

if our asymptotic expansion in  $\delta$  is to have solutions that go to zero at infinity.

After integration, the two conditions are reduced to

$$\bar{\sigma}_1(\bar{\sigma}_1 + 2\bar{\alpha}_1) C_p = 0, \quad \text{and} \quad (\text{D.9})$$

$$\left(8\frac{\tilde{\gamma}_2}{\beta} - \bar{\sigma}_1(\bar{\sigma}_1 + 2\bar{\alpha}_1)\right) C_q = 0. \quad (\text{D.10})$$

There are four different solution branches that will satisfy both of the above conditions. For the first series, take  $C_q \equiv 0$  and  $\bar{\sigma}_1 = -2\bar{\alpha}_1$ . For the second series, take  $C_q \equiv 0$  and  $\bar{\sigma}_1 = 0$ . For the third and fourth series, take  $C_p \equiv 0$  and

$$8\frac{\tilde{\gamma}_2}{\beta} - \bar{\sigma}_1(\bar{\sigma}_1 + 2\bar{\alpha}_1) = 0.$$

Solving for  $\bar{\sigma}_1$  in this case yields

$$\bar{\sigma}_1 = -\bar{\alpha}_1 \pm \sqrt{\bar{\alpha}_1^2 + 8\tilde{\gamma}_2/\beta}.$$

Without loss of generality, take  $\bar{\alpha}_1 = 1$  so that  $\delta = \bar{\alpha}$ . The above equation gives the approximate solution branches

$$\bar{\sigma} = -\bar{\alpha} \pm \sqrt{\bar{\alpha}^2 + 8\frac{\tilde{\gamma}}{\beta}} + O(\bar{\alpha}^2), \quad (\text{D.11})$$

where  $\bar{\alpha}$  is small.

The four solution branches are the two given by Equation D.11,  $\bar{\sigma} = 0$  and  $\bar{\sigma} = -2\bar{\alpha}$ . These branches are used to verify the numerical scheme used to find the bound-mode branches near  $\tilde{\gamma} = 0$ . The comparison shows good agreement for small  $\tilde{\gamma}$ , as expected. The computed eigenfunctions compare favorably to the eigenfunctions found in the above perturbation.

To illustrate the behavior of the branches more simply, it is convenient to return to  $\sigma = \bar{\sigma}(-\beta + \tilde{\gamma})$  and let  $\bar{\alpha} = 0$ . Then the four branches reduce to two branches along  $\sigma = 0$  and two branches given by

$$\begin{aligned} \sigma &= \pm 2\sqrt{2\beta\gamma} + O(\gamma) \quad \text{for } \tilde{\gamma} > 0 \quad \text{and} \\ \sigma &= \pm 2\sqrt{-2\beta\gamma} + O(\gamma) \quad \text{for } \tilde{\gamma} < 0. \end{aligned}$$

These are the two branches compared to the numerically generated branches shown in Figures 3.12 and 3.13.

# Appendix E

## Direct Simulation Algorithm

This appendix describes the finite-difference schemes used to compute direct simulations of the parametrically forced, damped, nonlinear Schrödinger equation, Equation 2.9. The simplest scheme uses a leapfrog time step and second-order central differences in space. Letting  $\Delta t$  represent the time step in  $\tau$  and  $\Delta x$  the spatial grid in  $\xi$ , the time and space are discretized as

$$\tau = n\Delta t \quad \text{and} \quad \xi = j\Delta x,$$

where  $n$  and  $j$  are integers. Let the envelope of the velocity potential be denoted

$$\Psi(\xi, \tau) = \Psi_j^n.$$

The leapfrog scheme takes initial data in  $\xi$  and uses a fourth-order, Runge-Kutta first time step. All subsequent steps are computed using the scheme

$$\begin{aligned} \Psi_j^{n+1} = & \Psi_j^{n-1} + 2\Delta t[(i\beta - \alpha)\Psi_j^n + \frac{ic^2}{\Delta x^2}(\Psi_{j+1}^n - 2\Psi_j^n + \Psi_{j-1}^n) + \\ & + i\gamma\Psi_j^{n*} + iA\Psi_j^n|\Psi_j^n|^2]. \end{aligned} \quad (\text{E.1})$$

A numerical-stability analysis on the above equation determines the relative orders of  $\Delta t$  and  $\Delta x$  leading to a stable numerical scheme. For simplicity, we discard  $\alpha$

and  $\gamma$  and approximate the nonlinear term by  $A\Psi|\Psi|^2 \simeq A\Psi|\Psi_o|^2$ , where  $\Psi_o$  is a characteristic wave amplitude. Using the von Neumann method for stability analysis, we take  $\Psi_j^n = \rho^n e^{ikj\Delta x}$ . Substituting into Equation E.1 with  $\alpha = \gamma = 0$  and the approximate cubic term gives

$$\rho^2 - 2i\Delta t[\beta + A|\Psi_o|^2 + \frac{2c^2}{\Delta x^2}(\cos(k\Delta x) - 1)]\rho - 1 = 0. \quad (\text{E.2})$$

The two roots of the above equation,  $\rho_{1,2}$ , satisfy

$$\rho_1\rho_2 = -1 \quad (\text{E.3})$$

$$\rho_1 + \rho_2 = -2i\Delta t \left[ \beta + A|\Psi_o|^2 + \frac{2c^2}{\Delta x^2}(\cos(k\Delta x) - 1) \right]. \quad (\text{E.4})$$

We require  $|\rho_{1,2}| < 1$  for stability. Equation E.3 implies that  $|\rho_1||\rho_2| = 1$ , so that stability implies  $|\rho_1| = |\rho_2| = 1$ . Then, using  $|\rho_1 + \rho_2| \leq |\rho_1| + |\rho_2| = 2$ , Equation E.4 implies that

$$\Delta t|\beta + A|\Psi_o|^2 + \frac{2c^2}{\Delta x^2}(\cos(k\Delta x) - 1)| \leq 1, \quad (\text{E.5})$$

which is the condition on  $\Delta x$  and  $\Delta t$  that implies a stable, numerical scheme. The addition of  $\alpha$ ,  $\gamma$  and the nonlinear term will change the scheme so that the above stability result is useful only as an approximate guideline. We find that when the leapfrog time step is replaced with a fourth-order, Runge-Kutta time step we get a more efficient scheme. The increased stability of the Runge-Kutta scheme allows for time steps that are large enough to offset the increase in computation at each step.

## References

- Barashenkov, I.V., Bogdan M. M. and Korobov V.I. 1991 Stability diagram of the phase-locked solitons in the parametrically driven, damped nonlinear Schrödinger equation. *Europhysics Letters* **15**, 113-118.
- Benjamin, T.B. and Ursell, F. 1954 The stability of the plane free surface of a liquid in vertical periodic motion. *Proc. Roy. Soc. Lond. A* **225**, pp. 505-515.
- Benjamin, T.B. 1972 The stability of solitary waves. *Proc. R. Soc. Lond. A* **328**, pp. 153-183.
- Bona, J. 1975 On the stability theory of solitary waves. *Proc. R. Soc. Lond. A* **344**, pp. 363-374.
- Camassa, R. and Wu, T.Y. 1991 Stability of some stationary solutions for the forced KdV equation. *Physica-D* **51**, 295-307.
- Chester, W. 1968 Resonant oscillations of water waves. *Proc. Roy. Soc. Lond. A* **306**, pp. 5-22.
- Denardo, B., Wright, W., Putterman, S. and Larraza, A. 1990 Observation of a kink soliton on the surface of a liquid. *Phys. Rev. Lett.* **64** #13, pp. 1518-1521.
- Faraday, M. 1831 On a peculiar class of acoustical figures; and on certain forms assumed by groups of particles upon vibrating elastic surfaces. *Phil. Trans. Roy. Soc. Lond.* **121**, 299-340.
- Guthart G.S. and Wu T.Y. 1991 Observation of a standing kink cross wave parametrically excited. *Proc. R. Soc. Lond. A* **434**, 435-440.
- Henderson, D. and Miles, J. 1990 Single-mode Faraday waves in small cylinders. *J. Fluid Mech.* **213**, 95-109.

Holm, D.D., Marsden, J.E., Ratiu, T. and Weinstein, A. 1985 Nonlinear stability of fluid and plasma equilibria. *Phys Rep.* **123**, 1-116.

Ince, E.L., 1926 *Ordinary differential equations*, New York: Dover Publications, 1956 Reprint, pp. 396-416.

Laedke, E.W. and Spatschek, K.H. 1991 On localized solutions in nonlinear Faraday resonance. *J. Fluid Mech.* **223**, 589-601.

Larraza, A. and Putterman, S. 1984 Theory of nonpropagating surface-wave solitons. *J. Fluid Mech.* **148**, 443-449.

Miles, J. 1967 Surface-wave damping in closed basins. *Proc. Roy. Soc. Lond. A* **297**, pp. 459-475.

Miles, J. 1984a Nonlinear Faraday resonance. *J. Fluid Mech.* **146**, 285-302.

Miles, J. 1984b Parametrically excited solitary waves *J. Fluid Mech.* **148**, 451-460.

Miles, J. and Henderson, D. 1990 Parametrically forced surface waves. *Annu. Rev. Fluid Mech.* **22**, 143-165.

Ockendon, J.R. and Ockendon, H. 1973 Resonant surface waves. *J. Fluid. Mech.* **59**, 397-413.

Rayleigh, Lord 1883a On maintained vibrations. *Philos. Mag.* **15**, 229-235. Reprinted, 1900, in *Scientific Papers*, **2**, 188-193. Cambridge: Univ. Press.

Rayleigh, Lord 1883b On the crispations of fluid resting upon a vibrating support. *Philos. Mag.* **16**, 50-58. Reprinted, 1900, in *Scientific Papers*, **2**, 212-219. Cambridge: Univ. Press.

Stuart, J.T. 1960 On the nonlinear mechanics of wave disturbances in stable and unstable parallel flows. *J. Fluid Mech* **23**, 353-370.

Stuart, J.T. and DiPrima, R.C. 1978 The Eckhaus and Benjamin-Feir resonance mechanisms *Proc. R. Soc. Lond. A* **362**, pp. 27-41.

Whitham, G.B. 1974 *Linear and nonlinear waves*, New York: Wiley-Interscience, pp. 602-603.

Whitham, G.B. 1976 Nonlinear effects in edge waves. *J. Fluid Mech.* **74**, 353-368.

Wiggins, S. 1990 *Introduction to applied nonlinear dynamical systems and chaos*, New York: Springer-Verlag, pp. 193-210.

Wu, J., Keolian, R. and Rudnick I. 1984 Observation of a nonpropagating hydrodynamic soliton. *Phys. Rev. Lett.* **52**, 1421-1424.

Yan, J., Zhou, C. and You J. 1992 Nonpropagating soliton and kink soliton in a mildly sloping channel. *Phys. Fluids A* **4**, 690-694.

Yates G.T. 1990 Some antisymmetric solutions with permanent form of the forced KdV equation. In *Engineering Science, Fluid Dynamics, A symposium to honor T.Y. Wu.* (G.T. Yates, editor), Singapore: World Scientific, pp. 119-131.

Zhidkov, P.E. 1986 Stability of a soliton solution of a nonlinear Schrödinger equation. *Differential Equations*, **22**, 703-711.

Zhu, J. 1986 Internal solitons generated by moving disturbances. *California Institute of Technology* Ph.D. thesis.